2011

Supercritical Fluid Aided Microencapsulation of Dry Powders

Raquel Carvallo
University of South Florida, rcarvall@mail.usf.edu

Scholar Commons Citation
Carvallo, Raquel, "Supercritical Fluid Aided Microencapsulation of Dry Powders" (2011). *Graduate Theses and Dissertations.*
http://scholarcommons.usf.edu/etd/3035

Supercritical Fluid Aided

Microencapsulation of Dry Powders

by

Raquel Carvallo

A dissertation submitted in partial fulfillment
of the requirements for the degree of
Doctor of Philosophy
Department of Chemical and Biomedical Engineering
College of Engineering
University of South Florida

Major Professor: Aydin K. Sunol, Ph.D.
Scott W. Campbell, Ph.D.
Shyam Mohapatra, Ph.D.
Douglas Shytle, Ph.D.
John T. Wolan, Ph.D.

Date of Approval:
June 4, 2011

Keywords: microparticle, coating, DMSO, Chitosan, biopolymer

DEDICATION

To my beloved husband who is the Angel in my life and to the best gift he could have ever given me, our son Marcelo.

ACKNOWLEDGMENTS

I would like to express my gratitude to all those who gave me the possibility to complete this dissertation. I want to thank the Chemical and Biomedical Engineering Department for giving me the opportunity to be part of USF as a student, an employee and a friend; and Donovan Industries, TempTroll, the National Science Foundation (NSF) and the Florida High Tech Corridor for their financial support.

I am deeply indebted to my advisor Dr. Aydin K. Sunol whose help, stimulating suggestions and encouragement helped me throughout my research.

I thank my colleagues from the Environmentally Friendly Engineering Systems (EFES) group for all their help, support and valuable input.

I want to thank Dr. Yusuf Emirov and the Nanomaterials and Nanomanufacturing Research Center (NNRC) at USF for their assistance using SEM, EDS and AFM, as well as Betty Loraamm for her help with using the TEM.

Most importantly, I would like to express my deeply appreciation to my family whose patient love enabled me to complete this work, and for being there to share the good times and cheer me up during the difficult ones.

TABLE OF CONTENTS

LIST OF TABLES

LIST OF FIGURES

NOMENCLATURE

AFM: Atomic Force Microscopy

ASES: Aerosol Solvent Extraction System

C_d: drag coefficient

CP: Critical Point

DMSO: Dimethyl Sulfoxide

d_p: particle diameter

DSC: Differential Scanning Calorimeter

EOS: Equation of State

f: fugacity

F: degrees of freedom

FDA: Food and Drug Administration

FTIR: Fourier Transform Infrared Spectroscopy

GAS: Gas Antisolvent

H: enthalpy

k: thermal conductivity

L: Liquid

RESS: Rapid Expansion of Supercritical Solutions

LCEP: Lower Critical End Point

LCST: Lower Critical Solution Temperature

LL: Liquid-Liquid

LLV: Liquid-Liquid-Vapor

Mn: number average molecular weight

MW: Molecular Weight

NMR: Nuclear Magnetic Resonance

P: Pressure

P_c: Critical pressure

PMMA: Polymethyl Methacrylate

PVA: Poly Vinyl Alcohol

PCA: Precipitation with Compressed Fluid Antisolvent

PDLA: Poly-(D-Lactide)

PGLA: Poly-(DL-Lactide-co-Glycolide)

PLLA: Poly-(L-Lactide)

Re: Reynolds number

T_L: low temperature

S: Solid

SAS: Supercritical Antisolvent

$SCCO_2$: Super Critical carbon dioxide

SCF: Super Critical Fluid

SEM: Scanning Electron Microscopy

SLV: Solid-Liquid-Vapor

SSV: Solid-Solid-Vapor

T: Temperature

T_c: critical temperature

TEM: Transmission Electron Microscopy

TGA: Thermal Gravimetric Analysis

T_H: high temperature

TP: Triple Point

UCEP: Upper Critical End Point

UCST: Upper Critical Solution Temperature

u_{mf}: minimum fluidization velocity

u_t: terminal velocity

UV: Ultraviolet

V: Vapor

VOC: volatile organic compound

x^*: overall equilibrium composition

x: Mole Fraction

y: Solubility

Greek Symbols

Å: Angstrom

ϕ: Fugacity coefficient

γ: Activity coefficient

μ: Dynamic viscosity

μm: Micron

ν: Kinematic viscosity

ρ: Density

σ: Surface tension

ω: Acentric factor

ABSTRACT

Coating of fine particles to produce tailored surface properties is currently a key development for supercritical fluids applications, in different areas such as: pharmaceutical, nutraceutical, cosmetic, agrochemical, electronic and specialty chemistry industries. During the encapsulation process the particle surface can be designed with specific properties by spreading a thin film coating material over the surface of the particles.

Chitosan, a natural polymer, was used in this work as the encapsulant material. Chitosan is biocompatible, biodegradable to normal body constituents, safe, non-toxic, bacteriostatic, anticancerogen, and versatile polymer. These attributes are among the properties that make Chitosan an attractive component of pharmaceutical products.

The main objective of this research was to encapsulate solid particles under 5µm with a biopolymer, Chitosan, using supercritical CO_2 as one of the solvents. In order to reach this goal, some the following initial tasks were completed: the cloud point for the system DMSO-CO_2 was determined and compared with published data to validate the experimental system. Subsequently the cloud point experiments were extended to include the ternary system Chitosan-DMSO-CO_2, and a dynamic solubility experimental set-up was constructed and used to obtain solubility data for the same ternary system.

A novel SCF fluidized bed was used to micro encapsulate porous (TiO_2) and non-porous particles (CaO) through a temperature swing with a Chitosan thin layer. DMSO was used as an entrainer to enable solubilization of Chitosan and removed within the supercritical carbon dioxide.

Several analytical methods were used to characterize these particles; SEM-EDS analysis was used to evaluate a group of particles, determining composition and particle diameter on samples up to 900 particles. TEM and AFM confirmed particles of one micron or less were encapsulated with a thickness of less than 5 nm. AFM shows particle roughness on the nanometer range, 46 nm or more for uncoated particles and 2-4 nm for the encapsulated ones.

FTIR, NMR and DSC-TGA analysis confirmed that the chemical structure of Chitosan remained constant before and after processing, and the changes observed were attributed to some DMSO and moisture adsorbed during the encapsulation process.

CHAPTER 1

INTRODUCTION

Encapsulation of fine particles to produce modified surface properties have extensive applications in different industries, such as pharmaceutical, nutraceutical, cosmetic, agrochemical, electronic and specialty chemistry industries. During the encapsulation process, the particle surface can be designed with a specific physical and/or chemical property by coating the surface of the particle with a thin film of encapsulant material. As a result, the flow-ability, dissolution rate, controlled release, masking, dispersability, chemical reactivity and hydrophilicity of particles can be modified to tailor specific applications. Encapsulated particles have a significant application in targeting and controlled release of therapeutic products, genes and other bioactive agents. This could be attributed to the fact that controlled release systems provide the benefits of protection from rapid degradation, targeting delivery, controlled release rate, and prolonged duration of bioactive agents (Benita S. 2006, Onwulata C. 2005).

There are several encapsulation technologies available, which can be classified into two categories:

- Physical methods: vibrating nozzle, spinning disk, pan coating, fluidized bed, freeze-drying, and spray drying being among the most frequently used methods.
- Chemical methods: coacervation, phase separation, interfacial polymerization, in situ polymerization and sol–gel methods. All of these have a common characteristic:

large amounts of organic solvents, surfactants, and other additives, which lead to volatile organic compound (VOC) emissions and other waste streams. Additional drawbacks include low encapsulation efficiency, toxic residual solvents in the end products, what usually leads to further processing, putting in risk the fragile structure of some chemicals or biochemical ingredients.

Spinning disk is an atomization method that involves the formation of a suspension of core particles in the coating liquid and the passage of this suspension over a rotating disk under conditions that generate a coating film much thinner than the core particle size. This technology was considered very promising for particles on the micron size range because the results were comparable to regular spray drying or freeze drying. On the other hand, scaling up would involve the construction of multi-head small nozzles which can certainly be a source of frequent clogging problems.

Freeze drying works under the fundamental principle of sublimation. The material to be preserved is frozen, and then lowering the atmospheric pressure below 0.06 atm, the ice turns directly into water vapor. The water vapor flows out of the freeze-drying chamber. This continues for a long period of time until the material gradually dries out.

Spray drying assembly requires a feed pump, an atomizer, an air heater, an air disperser, a drying chamber, and systems for exhaust air cleaning and powder recovery. An aqueous solution is sprayed as fine droplets into hot air, evaporating the water, and the dried solid is separated. This method and the regular fluidized beds have problems when fluidizing particles smaller than 100 μm, due to electrostatic forces that make fluidization difficult. Another problem involved with these methods is the atomization of the coating material, since droplets must be significantly smaller than the particle to be coated in order to achieve uniform and complete coating while avoiding agglomeration. Atomizing droplets at 10-100 nm is a demanding engineering problem (Gouin S. 2004).

Coacervation is a colloid phenomenon that consists of the phase separation into colloid-rich and colloid-poor layers, which requires large amounts of solvents. It is initiated by creating a perturbation: changing the temperature, the pH or adding a concentrated aqueous ionic salt solution or a non-solvent. The final step for microencapsulation is the hardening of the coacervate wall and the separation of the microcapsules, which generally is the toughest step in the total process, requiring a long processing period.

For many years there has been continuous interest in replacing conventional organic solvents with environmentally friendly fluids in different chemical processes. Supercritical carbon dioxide ($SCCO_2$) became known as an excellent candidate due to its characteristics and properties: it has mild critical conditions (T_c = 304.1 °K, P_c= 7.38 MPa) and is low cost, non-toxic, non-flammable, highly available and easily recycled. Finally, its most remarkable advantage is the fact that it shows gas-like diffusivities and liquid-like densities (McHugh and Krukonis, 1994). Supercritical carbon dioxide ($SCCO_2$) was used initially as a solvent or in other processing areas like supercritical extraction and separation; however, more recent applications are in particle formation and encapsulation.

During the past decade, supercritical fluid processes such as RESS (rapid expansion of supercritical solutions) (Tsutsumi 1995, Wang T. J. 2001, Wang Y. 2002; Mishima K. 2000, Kim J. H. 1996, Tsutsumi A. 2003, Matsuyama K., 2003a, Sun Y. P. 1998, Matsuyama K. 2003b), gas antisolvent (GAS), and precipitation with a compressed fluid antisolvent (PCA) (Falk, 1997; Young, 1999), also known as aerosol solvent extraction system (ASES) (Bleich, 1996) or supercritical antisolvent technique (SAS) (Wang Y., 2004; Wang Y., 2005; Elvassore, 2001; Duarte, 2006) have attracted increasing attention for particle encapsulation.

Some of the reasons that make supercritical encapsulation techniques an attractive option are:

- It is an environmentally benign technology, since the supercritical solvent used can be recovered at the end of the encapsulation process and recycled.
- It is a one step process where the core material is enclosed by the encapsulant and with a simple adjustment of the operation conditions; the supercritical solvent is released obtaining a clean final product.
- The selective solvatin power makes it possible to modulate the separation of a particular component from a multi-component mixture.
- The high solubility of cosolvents in the supercritical solvent make the drying of the microparticles rapid and efficient with a low level of residual solvent, as requested by the FDA.
- The carbon dioxide inactivates a wide variety of bacterial organisms in the absence of oxygen and in a slight acidic environment, generating a sanitized and sterile final product.
- The fact that supercritical fluids have zero surface tension and low viscosity promotes coverage of porous materials.

It is important to emphasize that encapsulated particles have many significant advantages, but there are some potential disadvantages that cannot be ignored: the possible toxicity of the solvents used, biocompatibility of the coating material, undesirable by-products of degradation, the chance of patient discomfort (in pharmaceutical and cosmetic applications), and the higher cost of controlled release systems compared with traditional formulations. These are some of the reasons that have been driving a significant amount of interest to switch to biodegradable polymers, which degrade as a result of natural biological processes. Most biodegradable polymers degrade through hydrolysis of the polymer chains to biologically acceptable and progressively smaller compounds. In some cases (i.e. poly-lactides, poly-glycolides and their co-polymers), the polymers will eventually break down to lactic acid and glycolic acid, entering the Kreb's cycle and break down into carbon dioxide and water.

Today the polymer industry offers a broad selection of biodegradable polymers with unique characteristics for different applications, depending on the time delivery range, the targeting objective (organ or cell) and the delivery pH (Brannon-Peppas 1997, Middleton and Tipton 1998).

One of the most difficult tasks in this research was finding a natural and versatile biopolymer, soluble on physiological pH, and non-toxic. Chitosan oligosaccharide lactate, which is a modified carbohydrate polymer derived from chitin deacetylation, meet all these requirements. Chitin is the second most abundant natural polysaccharide commercially derived from crustaceous shells (Muzzarelli 1973).

Some biopolymers frequently used in particle encapsulation, such as poly-(D-lactide) (PDLA), poly-(L-lactide) (PLLA), poly-(DL-lactide-co-glycolide) (PGLA), Dextran, Inulin and poly vinyl alcohol (PVA), are insoluble in pure $SCCO_2$. For this reason different authors (Bleich 1996, Mishima 2000, Reverchon 2000, Elvalssore 2001, Matsuyama 2003, Perez de Diego 2004) have been studying and processing these polymers with the assistance of a cosolvent, creating a ternary system, polymer-cosolvent-$SCCO_2$.

Selecting the proper cosolvent for any solubility process is a important step, as it can significantly influence and determine the homogeneity of the mixture, and the degree of dissolution of the solute into the given cosolvent. DMSO was chosen as a cosolvent for this work because it is able to solubilize the solid biopolymer Chitosan, as well as it is soluble in supercritical carbon dioxide, a basic requirement for any supercritical micronization or coating process (Rajasingam 2004, Kordikowski 1995, Yeo S. 1993, Reverchon 1998).

The objective of this research was to encapsulate dry powder particles with diameters on the micron and sub-micron range using a green, controllable and scalable technique (Supercritical Fluid Technology) in order to obtain a uniform and controllable coverage of particles with the chosen biopolymer.

To be able to pursue this objective, specific steps were followed in a logical and organized sequence.

Chapter 2 provides the fundamental thermodynamic background necessary to develop and analyze a supercritical encapsulation process. Phase equilibrium principles, recognized experimental methods for solubility measurement in supercritical fluids, phase diagrams for binary, ternary and polymer systems under supercritical conditions, and a brief introduction to biopolymers are discussed here.

In Chapter 3, a broad review of different supercritical particle encapsulation techniques published is presented. These techniques were classified based on the fact that the encapsulation systems can be homogeneous or heterogeneous and that the supercritical carbon dioxide can be used as a solvent or an antisolvent.

Chapter 4 is a compendium of the properties and specific characteristics of all the chemicals used for this work, including the supercritical solvent, the cosolvent, encapsulant and core material. As there is not much information available for the encapsulant material, and having an original encapsulation technique, the selection of well characterized and economic core material like calcium oxide (non-porous) and titanium dioxide (porous) was a requirement. The information presented in this chapter comes from literature data and direct experimental analysis.

In Chapter 5, all the experimental systems employed during this research are described in full detail. In total, three different set-ups were required. The first one is a static solubility set-up, used to establish the experimental cloud point for the binary system DMSO-CO_2 and for the ternary system Chitosan-DMSO-CO_2. As there was no data published for this particular ternary system, another set of experimental data is used to confirm these previous results, and an extraction cell is built to obtain dynamic solubility data. The final set-up presented is the encapsulation one, a 60 ml supercritical fluidized bed designed and built to encapsulate micron and sub-micron particles using a temperature perturbation technique. Diagrams and detailed experimental procedures are presented.

Chapter 6 includes the experimental results for the solubility and cloud point for the DMSO-$SCCO_2$ and Chitosan-DMSO-$SCCO_2$ system, as well as the encapsulation results and coating characterization. In the beginning of this chapter, the cloud point data for the binary system DMSO-$SCCO_2$ obtained during this research is presented and compared with some published information, after which some novel Chitosan-DMSO-$SCCO_2$ experimental data is shown, including cloud point and dynamic solubility results. Based on these results, the encapsulation conditions are established, showing the T-P effect over the encapsulant and final product. Multiple characterization techniques are followed in order to confirm the presence of Chitosan as encapsulant material and establish the quality of the final product. All these results are discussed in this chapter. Techniques like FTIR and EDS are employed to confirm the presence of Chitosan on the encapsulated sample; SEM, TEM and AFM are used to evaluate the particles before and after the encapsulation process in order to determine the quality of the proposed method and NMR, DSC-TGA are utilized to characterize the polymer coating before and after being processed.

Finally, the conclusions for all the steps followed in this dissertation are presented in Chapter 7, as well as recommendations for future work, as in all research, one door leads to many other doors.

CHAPTER 2

THERMODYNAMIC BACKGROUND FOR SUPERCRITICAL ENCAPSULATION

In this chapter, a brief introduction to supercritical fluids, measurement techniques, and phase diagram models will be presented, as a fundamental knowledge basis to develop a micro-encapsulation process under a supercritical environment. The solubility measurement techniques are presented as they are usually referred to in the literature, as well as the phase diagrams for binary and ternary systems shown. Polymers and biopolymers in supercritical fluids will be introduced at the end of this chapter, since they are the most commonly used coating material in particle encapsulation.

2.1. Supercritical Fluids

When talking about pure components, supercritical refers to the condition where the temperature and pressure pass the critical point at which the phase boundaries disappear. A supercritical fluid (SCF) is defined as a substance above its critical temperature (T_C) and critical pressure (P_C). The critical point (CP) represents the highest temperature and pressure at which the substance can exist as a vapor and liquid in equilibrium. The phenomenon can be easily explained by looking at the phase diagram for pure carbon dioxide (Figure 2.1).

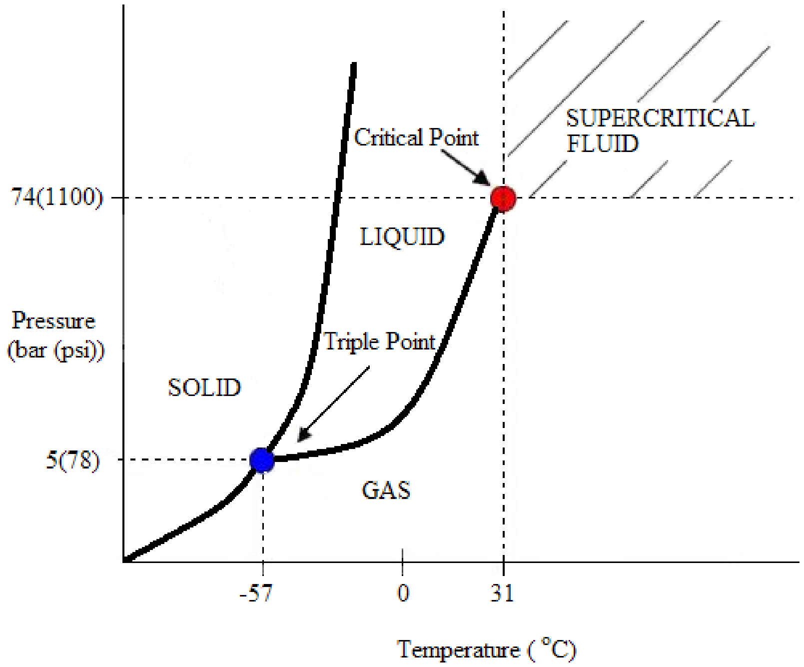

Figure 2.1. Phase Diagram for Carbon Dioxide

SCF technology has been in commercial use for more than 40 years as an environmentally benign, and energy-cost effective tool in a variety of industries, such as the decaffeination of coffee and tea (Vitzthum 1975) and for the extraction of flavors and essential oils from natural sources (Rizvi 1994, Grandison 1996). SCF technology is building its path in several pharmaceutical industrial operations, including product sterilization, crystallization, particle size reduction, coating, encapsulation and the preparation of drug delivery systems. It has also been shown to be a feasible option in the production of granular drug delivery systems, such as microparticles and nanoparticles, liposomes and encapsulated complexes, which control drug delivery and/or enhance drug stability.

There are advantages when working with supercritical fluids, for example:

- The fact that the critical temperature of carbon dioxide is close to ambient temperature makes it possible and safe to process heat-labile compounds.
- SCF functions as solvent for aliphatic hydrocarbons with chains of 20 carbons or less and for nearly all aromatic hydrocarbons.
- It can be used with cosolvents, such as methanol and acetone to enhance the solubility of polar solutes.
- Organic solvents, such halocarbons, aldehydes, esters, ketones, and alcohols are freely soluble in supercritical CO_2, facilitating the extraction of organic solvents.

Carbon dioxide can be used in two different ways: as a solvent or an antisolvent, depending on if the purpose is to coat particles or just to make particles by precipitation. For coating purposes, coverage of porous particles benefits from this particular solvent, since the diffusion coefficients of organic solvents in supercritical CO_2 are typically one or two orders of magnitude higher than in conventional organic solvents, making porous impregnation with controlled morphology and narrow particle size distribution (Table 2.1).

Carbon dioxide is non-toxic, non-flammable, inexpensive and recyclable. After finishing the chemical process, it can be separated completely from the final product by expanding it, and then liquefied for recycling purposes.

Supercritical fluids (SCF) can be applied on the production of pure active ingredient particles or a mixture of active ingredients and excipients (polymer or lipid carrier). The density and the solvent power of SCF could be adjusted significantly through a small perturbation of temperature and/or pressure around the critical region to tailor the product characteristics. SCF can even be used to coat therapeutic particles with single or multiple layers of polymers or lipids, by preparing a coating solution in SCF and choosing the adequate temperature and pressure conditions that do not solubilize the core material being coated.

Table 2.1. Fluid Properties for Different Pure Components Phases

Medium Properties	**Gases**(1)	**Liquids**(1)	**Supercritical Fluids**	
			T_c, P_c	**T_c, $4P_c$**(2)
Density, ρ (g/ml)	(0.6-2.0) x 10^{-3}	0.6 – 1.6	0.2 – 0.5	0.4 – 0.9
Diffusivity, D (cm^2/s)	(1.0-4.0) x 10^{-1}	(0.2-2.0) x 10^{-5}	0.7 x 10^{-3}	0.2 x 10^{-3}
Dynamic viscosity, μ $(g/cm-s)$	(1.0-3.0) x 10^{-4}	(0.2-3.0) x 10^{-2}	(1.0-3.0) x 10^{-4}	(3.0-9.0) x 10^{-4}
Surface tension, σ (dynes/cm)	-	10-400	-	-
Thermal conductivity, k (W/m K)	10^{-2}	10^{-1}	10^{-1}	10^{-1}

(1) Ambient conditions, (2) Conditions where pressure is four times higher than the critical pressure. (Bruce E. Poling, John M. Prausnitz, John O' Connell, 2000)

2.2. Solubility in Supercritical Fluids

The solvent power of supercritical fluids is a function of pressure and temperature. For this reason, the solubility power can be adjusted to solubilize or separate solutes and solvents by manipulating the operation conditions. Usually, the solvent power of a supercritical fluid increases with density and vice versa. Density can be reduced by decreasing the pressure or increasing the temperature.

For extraction or desorption purposes, different authors (Tan and Liou 1988 and 1989, Modell 1978) found that higher pressures at fixed temperatures promote these phenomena. The solvency power of supercritical fluids is enhanced as the fluid density increases with pressure increments at a given temperature, which is favorable for desorption, extraction or regeneration processes.

Pressure reduction at constant temperature leads to lower concentrations of the dissolved substances, causing precipitation of dissolved substances due to the lower density. In the same order of ideas but now considering the temperature effect, the density is reduced by temperature augmentation at constant pressure.

When working with mixtures of multiple solutes at supercritical conditions, the isotherms will intersect at the crossover points due to pressure adjustments, as illustrated in Figure 2.2 (Chimowitz 1986). For that reason, separation processes for solid mixtures can be designed in which the separation conditions will be located between the crossover points of the two species. For example, in Figure 2.2, consider a gas phase at a pressure Po, intermediate to crossover points P_1* and P_2*, which is cooled from temperature T_H (High Temperature) to T_L (Low Temperature). Note that the solubility of component 2 increases, while solubility of component 1 decreases. As an example, consider a process in which a mixture of components 1 and 2 are extracted at Po and T_H, and separated by a simple temperature decrease to T_L. This approach can be extended to multicomponent mixtures.

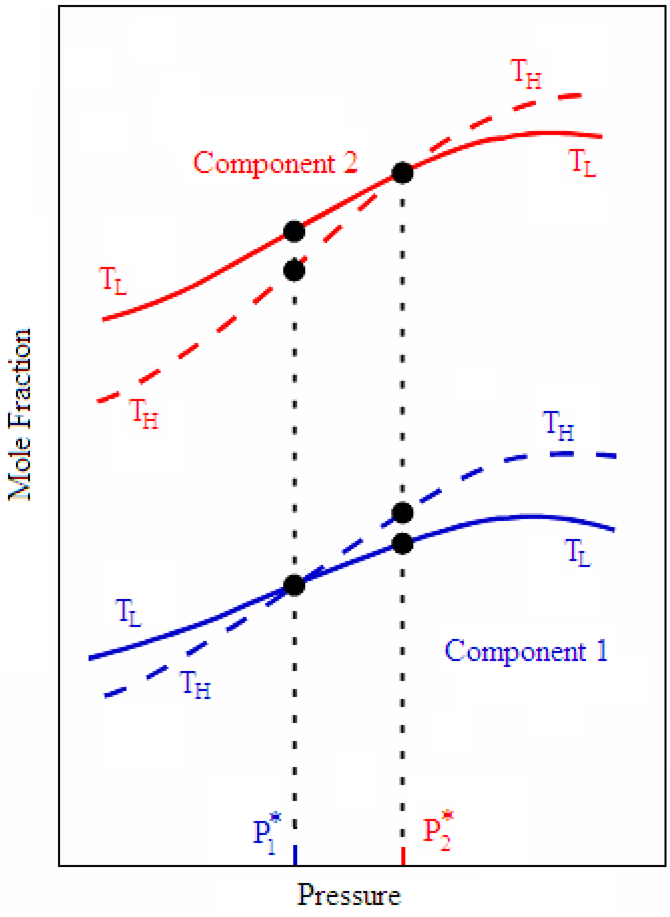

Figure 2.2. Crossover Phenomena for Multiple Solutes Mixtures. (Chimowitz, 1986)

The observed retrograde behavior for solubility of multicomponent solute mixtures is similar to the retrograde effects of pressure and temperature observed in sorption processes (Figure 2.3). As was presented by Tan and Liou 1990a and 1990b, the system Toluene-CO_2-Activated Carbon and Benzene-CO_2-Activated Carbon show crossover of the equilibrium loadings at different temperatures and relatively high pressure. The pressure at which the crossover occurred increased with the supercritical phase concentration for both components. This behavior was modeled by Akman and

Sunol 1991, by coupling supercritical sorption isotherms with a conventional fixed bed desorber model, where a high-density favored desorption was predicted.

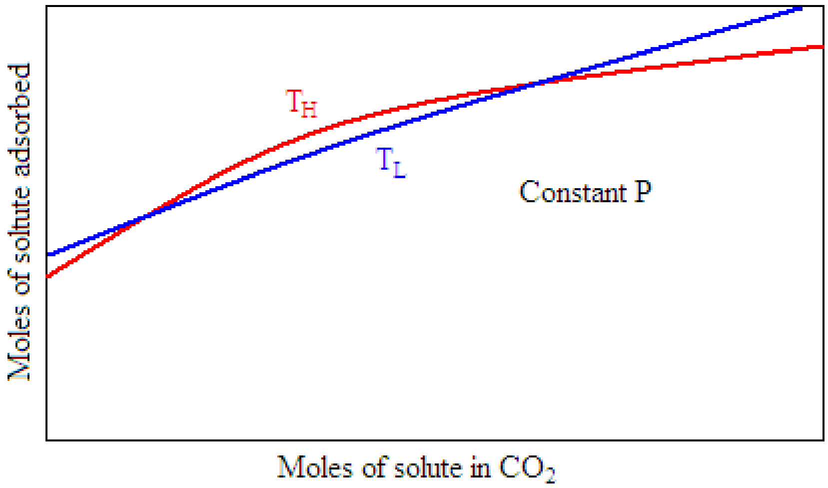

Figure 2.3. Crossover Phenomena in a Desorption Process. (Akman and Sunol, 1991)

2.3. Experimental Techniques for Solubility Measurements in Supercritical Fluids

The solubility of a solute in a supercritical fluid (SCF) is probably one of the most important thermo-physical mixture properties. The solubility information is desirable for the determination of Equation of State (EOS) interaction coefficients to allow prediction of the phase distribution of the solute. This information is used to understand the temperature-pressure dependence of the solubility in order to determine the appropriate operation conditions for process components such as extractors and separators.

To determine the feasibility of an encapsulation process, it is necessary to have the solubility of the encapsulant and the core material in the SCF. This data is not always available and some experimental determination of the data could be required. There have been a number of different approaches developed for the measurement of solute solubility for pure or multicomponent SCFs. These techniques are either dynamic, where the solute is continually removed within SCF at equilibrium conditions, or static, where known amounts of solute and solvents are preloaded into a cell where the pressure, temperature and/or volume can be adjusted to obtain the cloud point or equilibrium condition.

2.3.1. Dynamic Solubility Measurements for Supercritical Fluids

The diagram of a flow apparatus similar to the one used to determine the solubility of Chitosan in SCF is shown in Figure 2.4. In this system, the SCF is loaded to the system with a high pressure pump and compressed to the desired operating pressure.

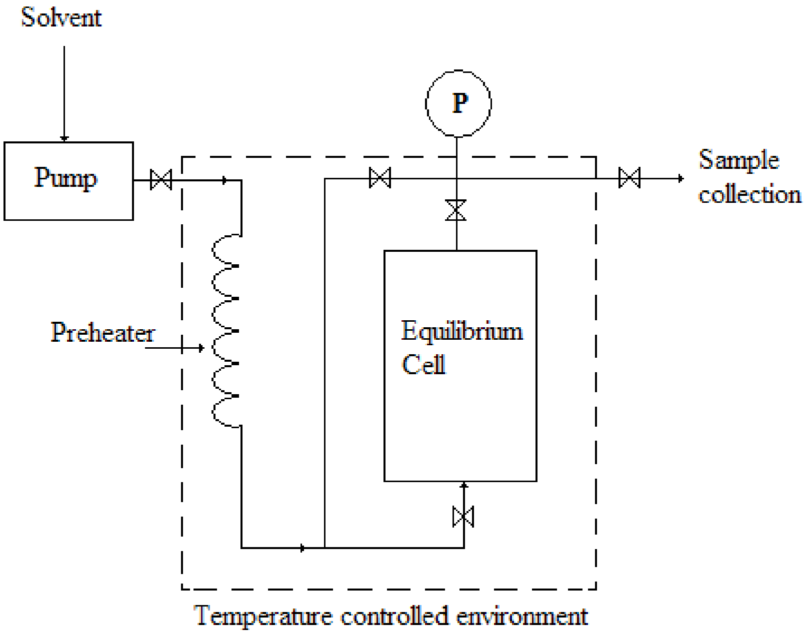

Figure 2.4. General Diagram of a Dynamic Flow Set-Up.

After leaving the pump, the SCF flows through a preheater within the constant temperature bath; this ensures that it reaches the required temperature before it contacts the heavy solute carefully preloaded into the equilibrium cell.

After the saturated SCF-rich phase exits the column, it is expanded at atmospheric pressure. The heavy component falls out of the solution and is collected in a cold trap. The advantages and disadvantages of using a dynamic flow system are listed in Table 2.2.

Table 2.2. Evaluation of Dynamic Solubility System.

Advantages
Off-the-shelf equipment is used
Large amounts of solubility data can be obtained
Equilibrium, stripping, or fractionation data can be obtained
A simple sampling procedure can be used
Disadvantages
At high pressure the density of the SCF-rich phase can become greater than the density of the solute-rich liquid phase, pushing out the liquid phase and causing inaccurate solubility data
Undetected phase changes can occur in the column, such as: solid$\rightarrow$liquid, liquid$_1\rightarrow$ liquid$_1$+ liquid$_2$
Cannot be used to determine solubility of liquid solutes
When running multi-component mixtures, extra care should be taken to avoid completely depleting one or more of the components.
A heavy solute can clog the system and cause erroneous solubility data.

2.3.2. Static Solubility Measurements for Supercritical Fluids

Figure 2.5 shows a diagram of a typical static view cell apparatus used to obtain solubility information (McHugh 1984 and 1985, Seckner 1988). The main component of this system is a high-pressure, variable-volume, view cell. This cell allows visual determination of the phases present at equilibrium.

The cell is initially loaded with a measured amount of solute (liquid or solid), after which a known amount of SCF is pumped into the cell. Then, keeping the temperature constant, the mixture in the cell is compressed to a single phase by adjusting the volume. The reported solubility data point is the pressure interval between the two-phase state and the single fluid-phase state.

The mixture critical point is defined by the pressure and temperature at which critical opalescence is observed for a slight change in either pressure or temperature.

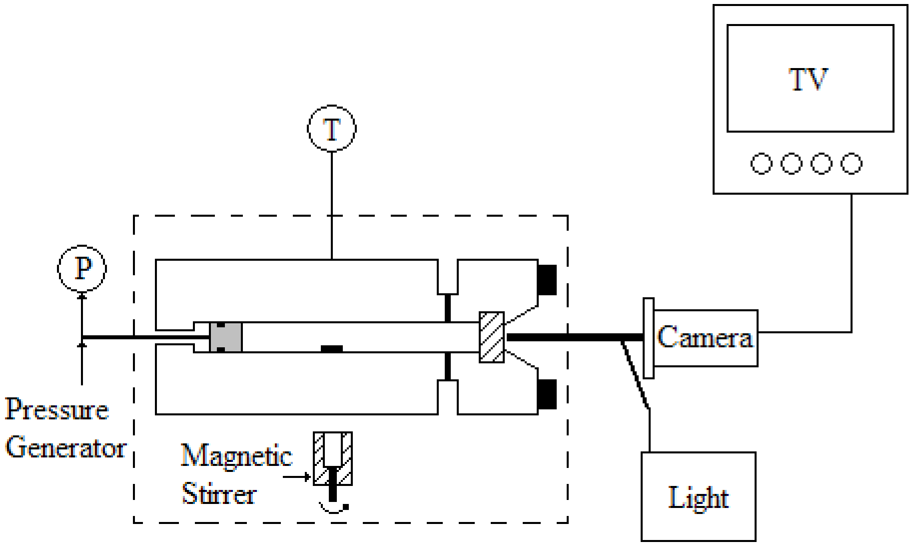

Figure 2.5. General Diagram of a Static View Cell Set-Up.

The advantages and disadvantages of a variable volume view cell apparatus are presented in Table 2.3.

Table 2.3. Evaluation of Static Solubility System.

Advantages
The phase transitions are also determined visually, and phase inversions are easily detected.
The solubility of solids and liquids in binary mixtures are obtained without sampling.
Heavy solids, liquids and polymers can be studied.
Minimum amounts of chemical components or SCF are used in an experiment.
The pressure of the mixture can be continuously adjusted at a fixed composition and temperature.
Disadvantages
SCF fractionation data are not easily obtained.
Just one sample mix can be studied per loading

2.4. Phase Equilibria

An understanding of the phase equilibrium of mixtures is fundamental for the design of supercritical fluid processes. Accurate high pressure equilibrium data for multi-component systems are difficult to obtain and time consuming; therefore it would be ideal to be able to predict it from pure component properties. However, it is possible to make such predictions in all cases, so it is useful to correlate and extrapolate limited experimental data.

Before describing the characteristics of the phase diagrams, it is helpful to remember the Phase Rule. The Phase Rule describes the possible number of degrees of freedom in a (closed) system at equilibrium, in terms of the number of separate phases and the number of chemical constituents in the system. The phase rule not only gives the number of independent variables that should be fixed to define a multiphase, multi-component mixture, it also specifies the topology of the phase diagrams used to represent that behavior. This explanation is represented in Table 2.4 (McHugh and Krukonis, 1994).

Table 2.4. Summary of the Geometrical Features
of Phase Diagrams for One and Two Components.

Number of Equilibrium Phases		**Degrees of Freedom**	**Geometrical Features**
One Component System	**Two Component System**		
3	4	0	Points
2	3	1	Lines
1	2	2	Surfaces
-	1	3	Volumes

Phase diagrams are essential instruments for the study of supercritical mixtures, due to the high level of complexity of the intermolecular interactions in dense fluids that makes solubility calculations difficult and not always reliable. This is why understanding the possible types of phase diagrams applicable for the mixture of interest, can help minimize the amount of experimental work needed to determine the solubility levels over wide ranges of temperature and pressure.

Before describing the possible phase diagrams for supercritical systems, some phase transition definitions commonly used are presented in Table 2.5.

Table 2.5. Definitions of Phase Transitions Occurring at High Pressures.

Abbreviation	**Transition**	**Description**
LCST	Lower Critical Solution Temperature	a) Temperature at which two liquids merge to form a single liquid phase as the system temperature decreases at constant pressure. b) Temperature at which the transition described in (a) takes place in the presence of a gas phase.
UCST	Upper Critical Solution Temperature	Temperature at which two liquids merge forming a single liquid phase when the system temperature is ramping up; the UCST takes place at a lower temperature than the LCST.
UCEP	Upper Critical End Point	a) For systems solid-SCF, the UCEP is the point at which the liquid and the gas phase merge to form a single fluid phase in the presence of a noncritical solid phase. b) For systems liquid-SCF, the UCEP takes place at the intersection of the UCST curve and a three-phase liquid-liquid-vapor; the UCEP is also the intersection of the LLV line with the lower temperature branch of the critical mixture curve.
LCEP	Lower Critical End Point	For systems solid-SCF, the LCEP takes place when a liquid and a gas phase merge to form a single fluid phase in the presence of a noncritical solid phase.

(McHugh and Krukonis, 1994)

When operating at supercritical conditions, it is recommended to keep away from regions of multiple phases in pressure-temperature-composition space, such as: liquid-liquid-vapor (LLV), solid-liquid-vapor (SLV) or solid-solid-vapor (SSV) equilibrium; because when these regions of multiple phases are projected onto a two dimensional P-T diagram, their geometrical representations are simplified, since the pressure and temperature (field properties) are the same in each of the equilibrium phases.

2.5. Phase Diagrams for Binary Mixtures

McHugh and Krukonis have found that many of the behaviors observed in phase diagrams for multi-component mixtures are very similar to the phase diagrams for binary mixtures, even if the components vary in molecular size, shape, structure and/or attractive potential. Following their classification, a description of the phase diagrams for a supercritical solvent and a single solute are presented in this section.

2.5.1. Type I

The phase diagram for a Type I system is shown in Figure 2.6, which illustrates the behavior of a binary system with respect to temperature, pressure and composition by using three-and two-dimensional plots. This phase equilibrium is characteristic for binary systems conformed by a supercritical component and a compound of medium volatility, or components with similar molecular diameter and/or similar interaction forces.

The light component (lower molecular weight) will be identified with number 1, while the heavy component (higher molecular weight) will be identified with the number 2. When evaluating the interval where the molar fraction of the heavy compound (2) varies from x=0 to x=1, the vapor-pressure curves for components 1 and 2, they separate into gas and liquid regions. The vapor pressure curves end at the critical point of each component, T_{C1} and T_{C2}. The critical curve, symbolized by the broken line in Figures 2.6a and 2.6b, connects the critical points and limits the two-phase region.

The molar composition of the heavy compound is denoted by *x*, T_1 is a temperature below the critical temperature of the components and T_2 is a temperature above the critical temperature of the light component (1).

Figure 2.6c shows that a single vapor phase will exist at very low pressures with an equilibrium composition x* at a temperature $T_1 < T_{C1.}$ As the pressure is isothermally increased a two-phase vapor-liquid envelope is formed and the liquid phase becomes visible. The equilibrium composition of the vapor and liquid phases will be given by the horizontal tie lines in the envelope. As the pressure is increased continuously while keeping the temperature constant at a fixed composition (x*), the amount of the liquid phase increases while the amount of the vapor phase decreases until only a small bubble of vapor remains, and finally the bubble of vapor disappears, turning into a single liquid phase.

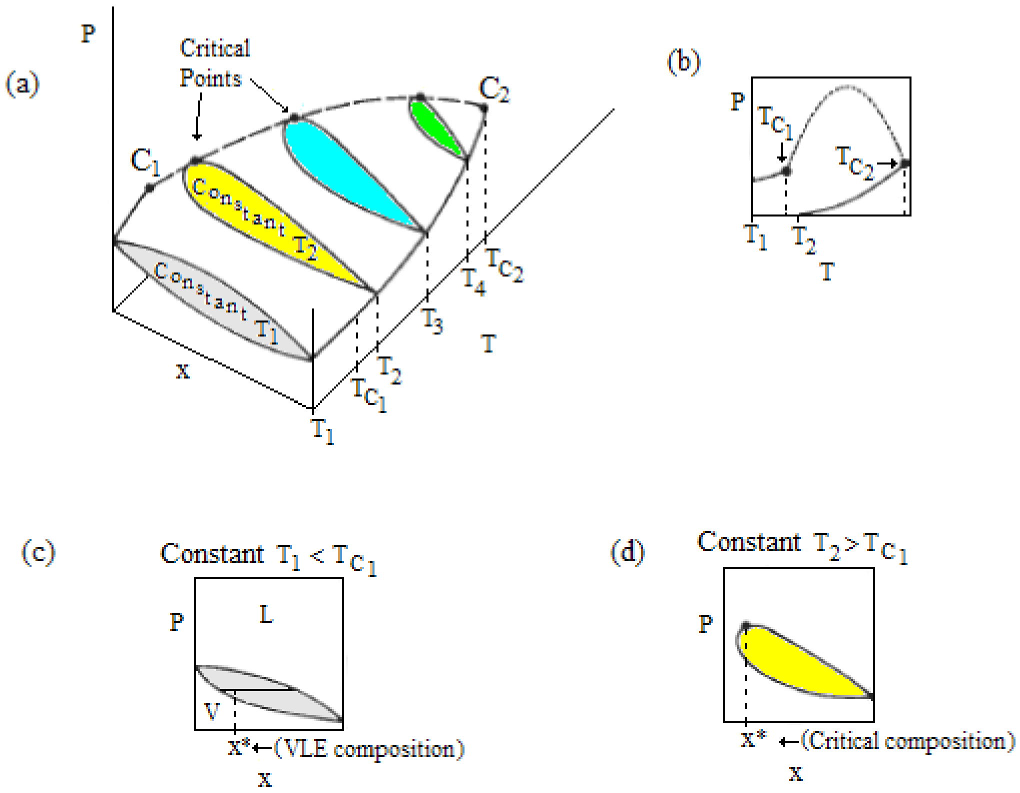

Figure 2.6. Phase Diagram Type I for a Binary Mixture. (a) P-T-x, (b) P-T, (c, d) P-x.

Next, as the temperature is raised to T_2, where $T_2 > T_{C1}$, just the right end of the molar composition x will be observed, as showing in Figure 2.6d. In this plot the left-hand side of the vapor-liquid does not touch the pressure axis; at the equilibrium composition x* in Figure 2.6d, the vapor-liquid envelope is intersected along the dew point curve at low pressures. As the pressure is raised, the vapor-liquid envelope is intersected at its highest pressure, which corresponds to the mixture critical point at T_2 and x*. This mixture critical point is identified with the intersection of the dashed curve in Figure 2.6b and the vertical isotherm at T_2. At the critical mixture point, the dew point and bubble point curves concur and all the properties at each of the phases becomes the same.

2.5.2. Type II

This type of behavior is presented in Figure 2.7. It is similar to the Type I system, in that the critical mixture curve is a continuous curve between the critical points of the two pure components (1 and 2). However, at low temperatures, liquid-liquid phase separation occurs, resulting in a liquid-liquid-vapor (LLV) line in Figure 2.7a. This LLV equilibrium line intersects the liquid-liquid critical line (Figure 2.7b) at an UCEP (upper critical end point). At this point, the two liquid phases become identical in the presence of a vapor phase. Only liquid-liquid equilibria exist at pressures higher than the colored surface, representing equilibrium of the three phases (Figure 2.7b).

The P-T group of liquid-liquid critical points is known as upper critical solution temperature (UCST) and is not affected by pressure changes; it is just a function of temperature for a given composition.

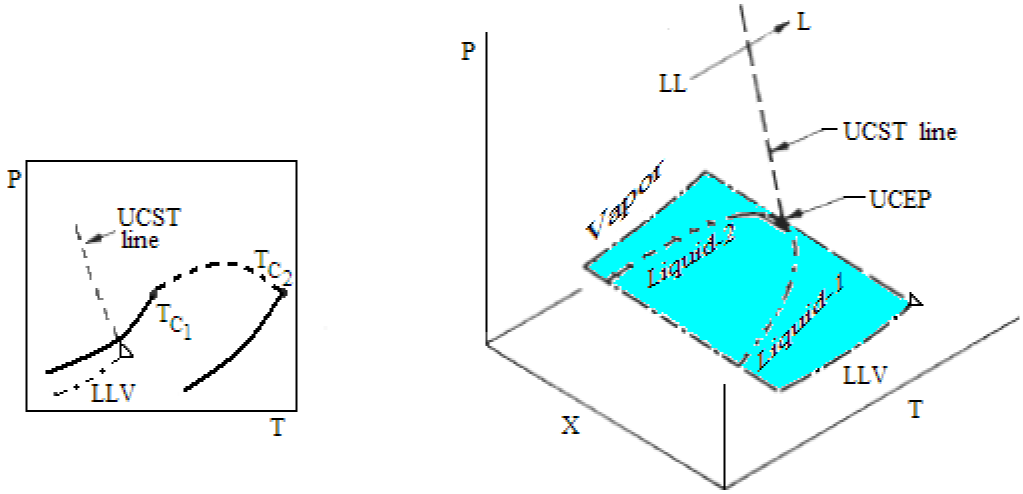

(a) (b)

Figure 2.7. Phase Diagram Type II for a Binary Mixture. (a) P-T, (b) P-T-x.

2.5.3. Type III

This type of diagrams corresponds to a system in which the critical properties of the two mixture components are significantly different, as a result of a different molecular weight, structure and/or intermolecular forces between the molecules.

The Type III diagram (Figure 2.8b) differentiates from Types I and II in that it has a LLV region very close to T_{C1}. The Te branch of the critical line that starts at T_{C2}, symbolized as usual as a dotted line, intersects the LLV line at the low-temperature end known as Lower Critical Solution Temperature (LCST).

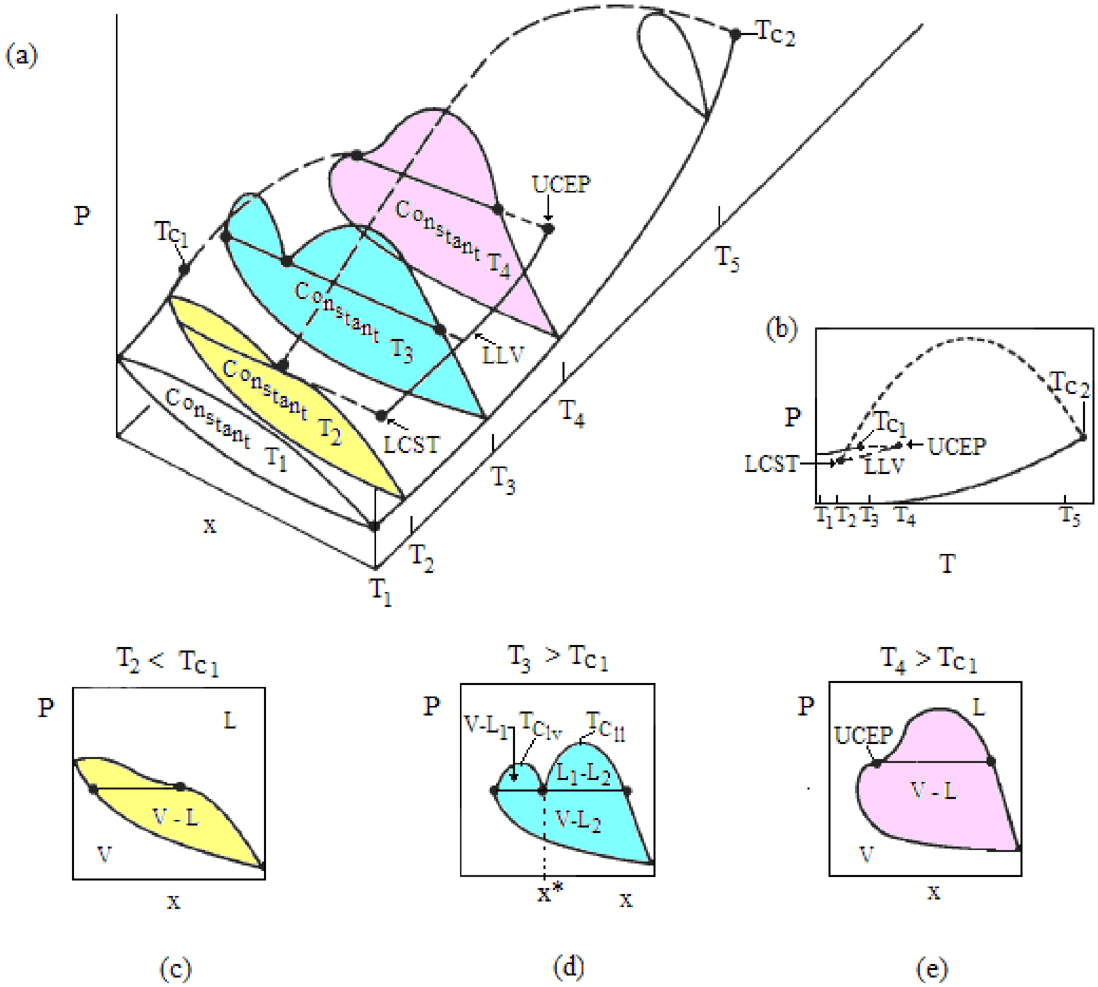

Figure 2.8. Phase Diagram Type III for a Binary Mixture.
(a) P-T-x , (b) P-T , (c) P-x , (d) P-x , (e) P-x.

The other branch of the critical mixture temperature, which starts at T_{C1}, intersects the LLV line at the high temperature end known as Upper Critical End Point (UCEP), as can be observed in the P-T diagram of Figure 2.8b.

From Figure 2.8a, it can be seen that the P-T diagram at T_1, a temperature below the LCST, is similar to the one described for the Type I system in Figure 2.6c. When the temperature is raised to T_2, where $T_2 <$ LCST, the isotherm drawn at this specific temperature just misses the LLV line. Then in Figures 2.8a and 2.8c, a particular envelope shape is observed, where the single liquid phase is almost divided into two liquids to form a three phase LLV system.

When the temperature is slightly incremented to T_3, the LLV line will be intersected, as shown in Figures 2.8b and 2.8d, indicating that two liquids have been formed in the presence of a vapor phase. At low pressures, a single vapor phase exists. As pressure is raised, the dew point line of the liquid-vapor envelope is intersected and a liquid phase is formed. If the pressure is increased and the overall mixture composition is less than x*, a vapor-liquid envelope is obtained. If the overall mixture composition is greater than x*, a liquid-liquid envelope is observed. At T_3, two critical points are observed, one at the top of the vapor-liquid envelope (T_{Clv}) and the other at the top of the liquid-liquid envelope (T_{Cll}).

When temperature is raised to T_4 = UCEP, Figure 2.8e shows the P-x diagram expected. This isotherm intersects the vapor pressure curve for the less volatile component, the high-temperature end of the LLV line (UCEP) and the critical mixture curve. At low pressure, a single vapor phase exists. As the pressure is isothermally increased the dew point curve is intersected, revealing a single liquid-vapor phase.

2.5.4. Type IV

This type of system (Figure 2.9) is obtained when the differences in size, structure or strength of the intermolecular forces between the two mixture components are remarkably larger than in the Type III system.

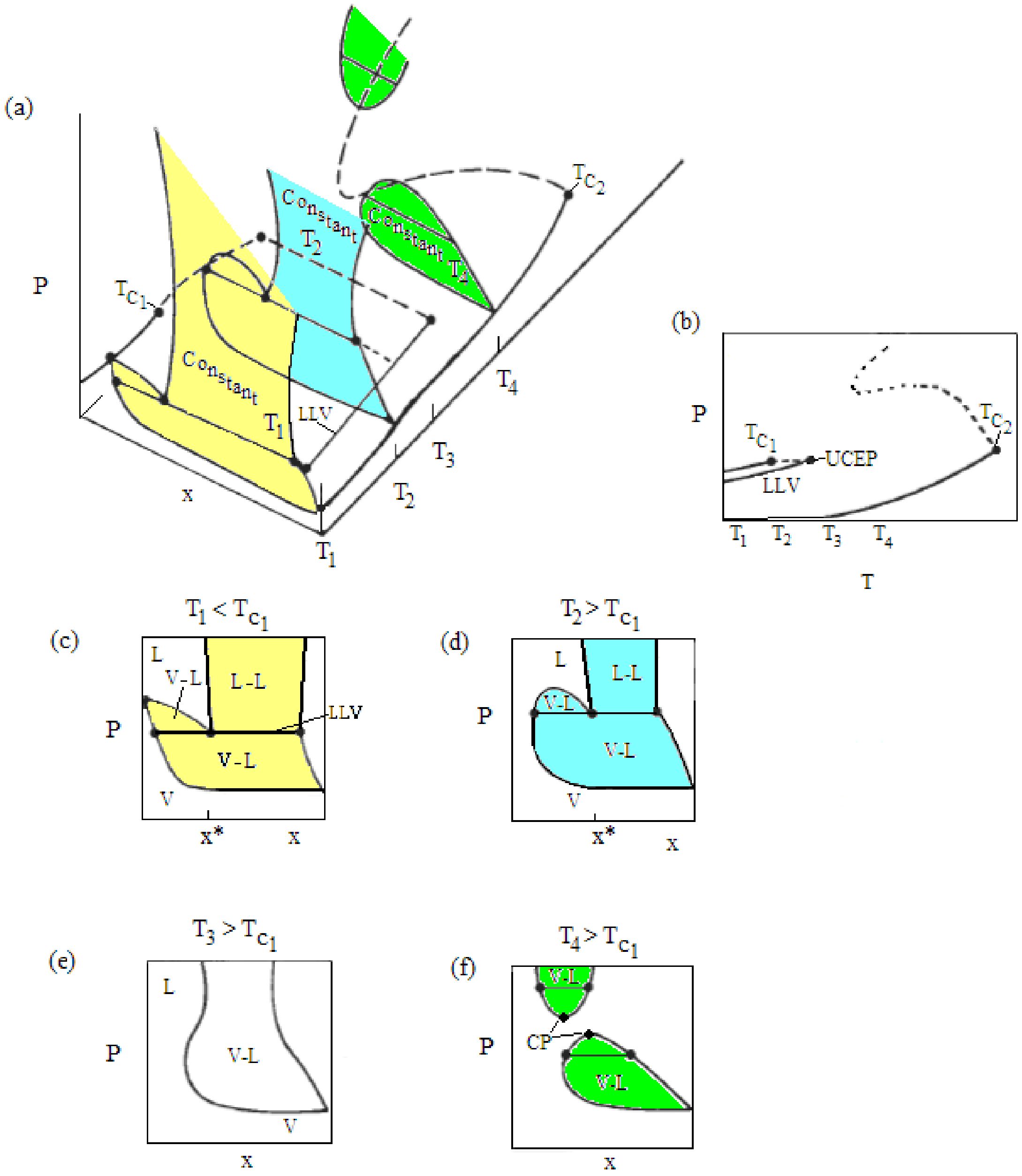

Figure 2.9. Phase Diagram Type IV for a Binary Mixture.
(a) P-T-x , (b) P-T , (c) P-x , (d) P-x , (e) P-x.

At T_1, the LLV line and the pressure curve of the component 1 are intersected, but at T_2, the LLV line is intersected and not the pressure curve of the more volatile component (Figure 2.9b). At pressures higher than the LLV pressure Figures 2.9c and 2.9d show that at concentrations greater than x* the liquid-liquid envelope does not exhibit a closed dome with a mixture critical point.

The diagram is presented in Figure 2.9e shows the phase behavior when the temperature is higher than the UCEP temperature (T_3). Two phases exist as the pressure increase. The two branches of the vapor liquid phase envelope start getting closer in composition at an intermediate pressure, as a mixture critical point may occur; but as the pressure increases, the two curves begin to diverge.

When the temperature is raised towards T_4 the vapor-liquid envelope gets closed, resulting in a mixture critical point (CP) at a moderate pressure. If the pressure values become greater than the mixture critical pressure then a single fluid phase will exist at T_4. If the pressure is increased further than the mixture critical pressure, a single fluid phase splits into two phases. Figure 2.9f shows the two-phase regions with their tie lines and two mixture critical points (CP) at T_4, depending on the overall composition of the mixture. One critical point occurs at the maximum of the vapor-liquid envelope as the pressure is increased isothermally from low to a moderate value, while the other mixture critical point (CP) occurs at the minimum of the fluid-liquid envelope at higher pressures.

2.5.5. Type V

As shown in Figure 2.10, this phase behavior is very similar to the previously described Type III system; but in Type V phase behavior, there is no region of liquid immiscibility at temperatures below LCST.

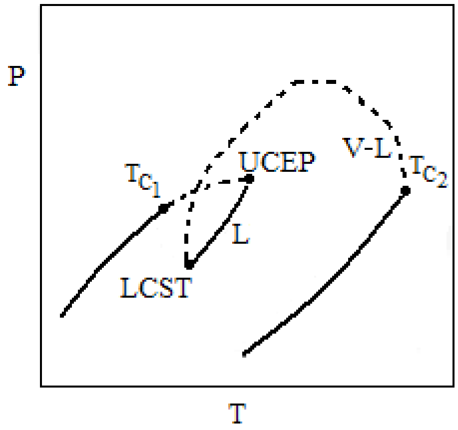

Figure 2.10. Type V P-T Phase Diagram.

2.5.6. Type VI

This type of equilibria is the only one that cannot be described by van der Waals equation of state, since the components involved in these systems develop hydrogen bonding. In these particular systems a continuous, gas-liquid critical curve and a liquid-liquid critical curve intersects the LLV line at UCEP and LCEP points (Figure 2.11).

This phase behavior is found in systems with specific chemical interactions, like water-alcohol. It consists of a liquid-vapor critical line connecting the two critical points of the pure components T_{C1} and T_{C2}, and a LL immiscibility critical line with a maximum pressure connecting both UCEP and LCEP of the same three-phase line. Another possibility is the existence of a second LL critical curve at high pressure with a pressure minimum; this phenomenon is called high pressure immiscibility. Also, the low-pressure immiscibility region and the high-pressure immiscibility region can be combined in one uninterrupted LL region (Andreas Bolz 1998).

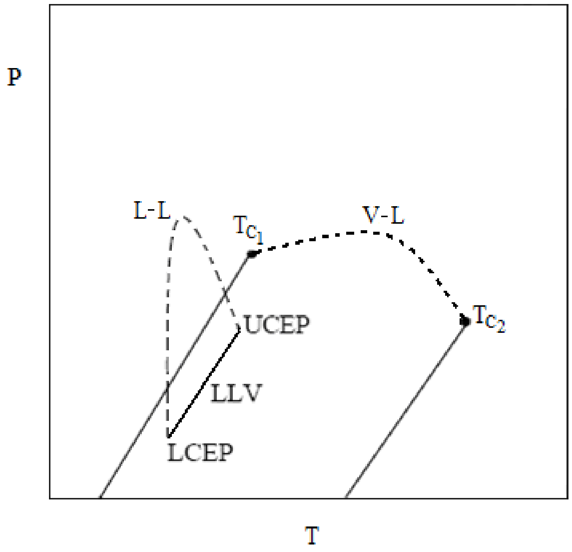

Figure 2.11. Type VI P-T Phase Diagram.

2.6. Phase Diagrams for Solid-Supercritical Fluid

Solid-SCF mixtures constitute a large and important subset of binary mixes, as was presented by Thomas J. Bruno and James F. Ely 1991. For these types of mixtures, usually the melting point of the solid is greater than the critical temperature of the SCF.

The vapor pressure curves of both components are shown in Figure 2.12a, as well as the melting and sublimation curves for the pure solid. A solid-liquid-vapor (SLV) line that starts at the triple point (TP) of the pure solid and ends on the upper branch of the gas-liquid critical curve at the UCEP, indicates that the melting point of the solid is decreased in the presence of the supercritical fluid. This behavior can be attributed to the fact that the SCF dissolves the solid in the equilibrium liquid phase, lowering the melting point of the heavy component.

In Figure 2.12b, the phase diagram for a temperature in-between the SCF critical point and LCEP (T_1) is presented. At low pressures, a solid-vapor equilibrium is observed, for a high solid concentration. As the pressure increases, the system comes across the SLV line. At high solid concentration, a solid–liquid equilibrium will be reached, merging continuously into a solid-fluid equilibrium with further pressure increments. At lower solid concentrations and pressures, a liquid–vapor equilibria envelope is obtained with a critical point (CP) at the top of it.

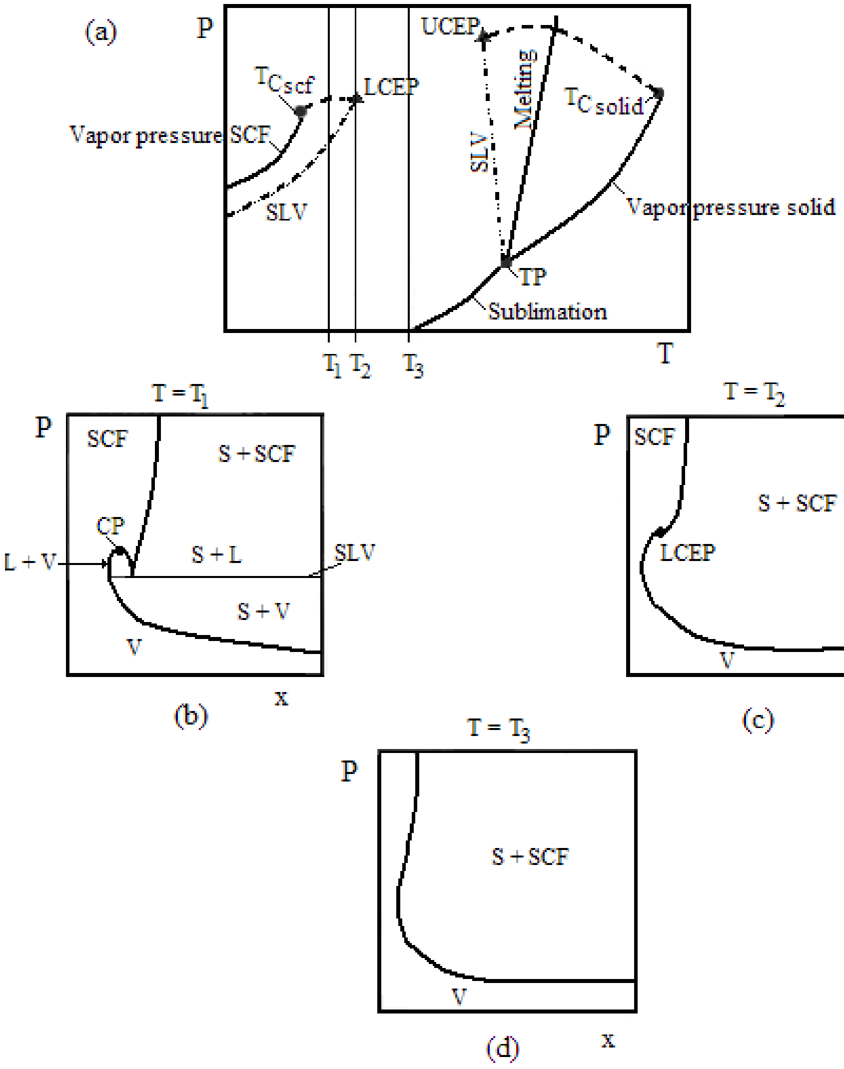

Figure 2.12. Phase Diagram for a Solid-SCF System

As the temperature increases to T_2, the liquid-vapor envelope disappears at the LCEP, becoming a single solid-SCF equilibrium region. As can be inferred from Figure 2.12c, the LCEP is a crucial point when using SCF as solvents, since small pressure changes around it can turn the binary system Solid-SCF into a one phase system, a SCF system. Continuing with temperature increases to T_3, shown in Figure 2.12d, the inflection point at LCEP vanishes.

2.7. Phase Diagrams for Ternary Mixtures

The phase behavior diagrams used for ternary systems consist of a supercritical fluid and two other components that are liquids at room temperature, following the classification suggested by Elgin J. C. 1959. The ternary phase diagrams were organized into three different classes, based on the appearance of liquid-liquid-vapor (LLV) regions. The diagrams are presented as three binary pairs, where each of the three diagram axes represents a single tie line for a binary pair at a certain temperature and pressure.

In order to be able to study a ternary system, it is required to fix three degrees of freedom, such as P, T and overall mixture composition. The ternary diagrams shown set the SCF in the lower left-hand corner, the least soluble component (A) in the lower right-hand corner and the third component (B) is placed at the top of the triangle phase diagram.

2.7.1. Type I

The three diagrams in Figure 2.13 represent mixtures at a fixed temperature, somewhat higher than the critical temperature of the SCF, and three different pressures.

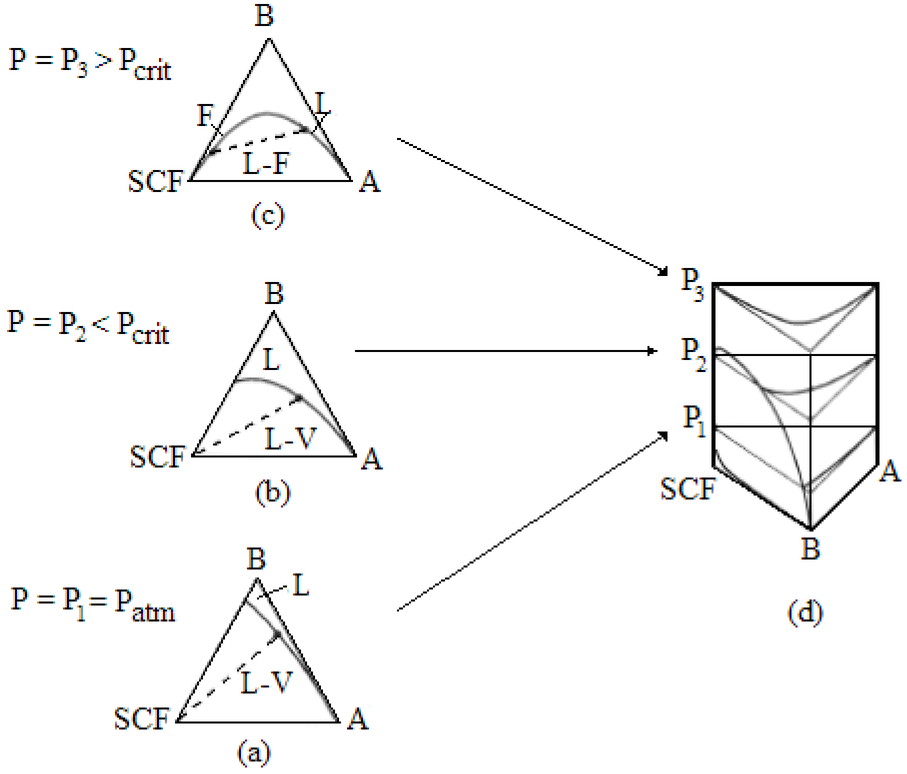

Figure 2.13. Phase Diagram for a Type I Ternary Mixture

A particular characteristic of Type I systems is the absence of liquid-liquid-vapor (LLV) immiscibility regions within the ternary diagram. Figure 2.13a shows that at atmospheric pressure (P_1), component A is miscible in all proportions with component B, while the SCF is almost immiscible in A and slightly soluble in component B. The solid curve in the diagram separates the one-phase liquid (L) region from the two-phase liquid-vapor (L-V) region.

In Figure 2.13b, the pressure of the system has been increased to a point slightly below the critical pressure of the SCF ($P=P_2<Pc$). At this pressure the SCF still remains practically insoluble in component A but its solubility in B has increased; the tie line for the SCF-B mixture became smaller too, reflecting that the solubility of component B and SCF-rich phase has increased.

In Figure 2.13c the pressure is increased to a value greater than the critical pressure for the SCF-B mix ($P=P_3>Pc$). The SCF is now miscible in all proportions with B, and the binodal curve does not intersect the SCF-B binary axis, while the SCF remains insoluble in A. The binodal curve intersects the SCF-A binary axis in two places, indicating that a liquid phase, mostly a mixture of A and B, is in equilibrium with a fluid phase, mainly the SCF with component B.

2.7.2. Type II

This phase diagram is presented in Figure 2.14. What distinguishes this ternary mix from other systems is that liquid-liquid-vapor (LLV) regions appear within the pressure-composition prism but do not extend to the SCF-B face of the prism.

Figure 2.14a shows that the phase diagram at atmospheric pressure ($P=P_1=Patm$) is identical to the one described previously for the Type I mixture.

If the pressure is increased to P_2, a pressure below the critical pressure of the SCF ($P=P_2<Pc$), a miscibility break appears for various SCF-A-B compositions where liquid-liquid (LL) and liquid-liquid-vapor (LLV) regions are generated, as shown in Figure 2.14b.

In Figure 2.14c, the pressure is increased to P_3, where ($P=P_3=P_c$), and the LL and LLV regions expand considerably. If the tie lines in the LL region become parallel to the A-B binary axis, the selectivity $(y_A/x_A)/(y_B/x_B)$ approaches values greater than 1.0, indicating that a very good separation of A from B could be obtained at this condition.

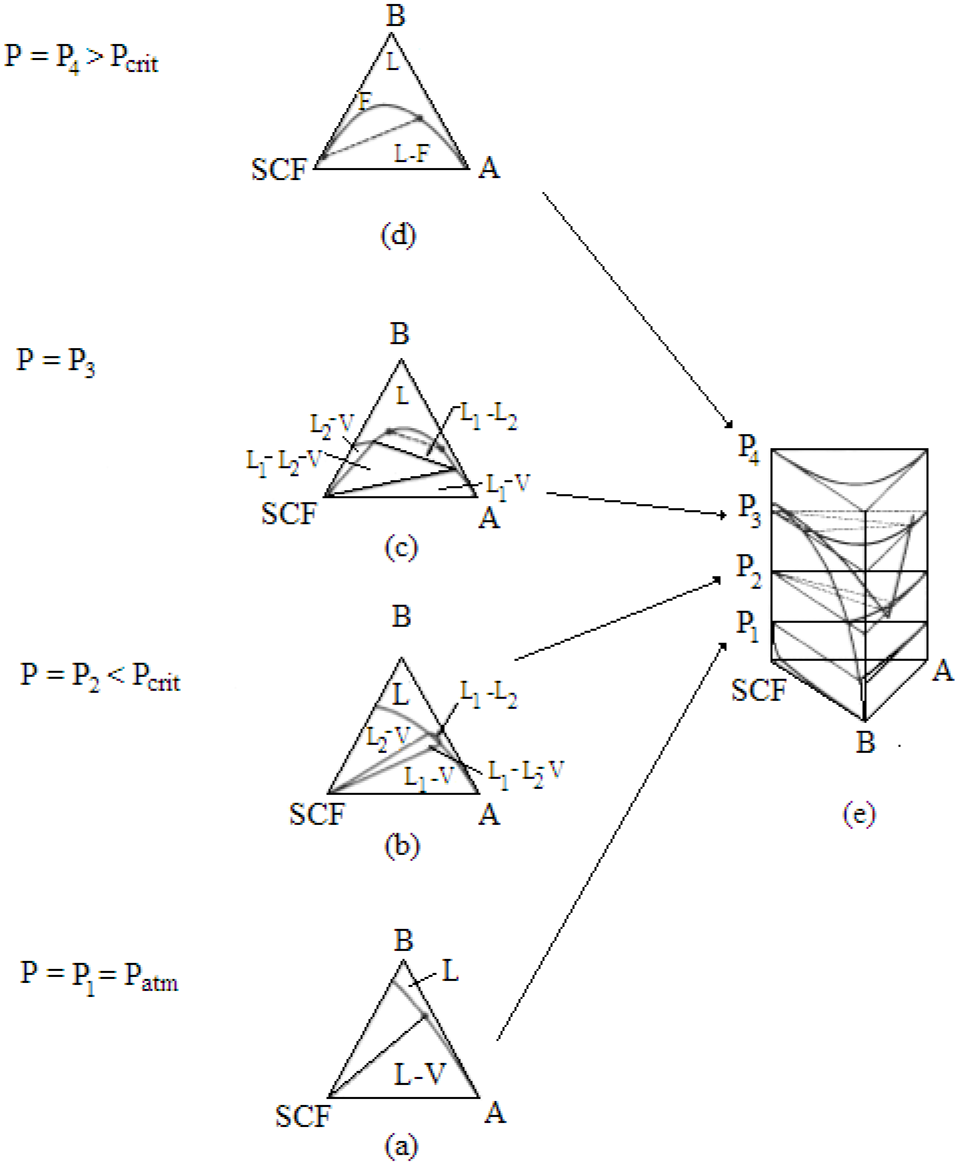

Figure 2.14. Phase Diagram for a Type II Ternary Mixture.

If the pressure is further increased above the critical pressure for the SCF-B mixture (P= P_4>Pc), the LLV miscibility gap disappears and the phase behavior becomes identical to that described for a Type I ternary system (Figure 2.13d), where at most two phases exist.

2.7.3. Type III

The distinguishing feature of Type III ternary phase behavior is that the binary A-B mixture is immiscible at very low pressures, as can be seen in Figure 2.15a. As SCF is added to the A-B mixture (Figure 2.15b), a very large LLV region appears in this diagram, then by increasing the pressure, the LL region close to the A-B axis expands. If the pressure value is greater than the critical pressure for the SCF-B mix (P=P_3>Pc), a single liquid-fluid solubility curve is formed. In Figure 2.15c, the liquid-fluid solubility curve intersects the A-B axis at the end of the binary A-B tie line, indicating that, even at an elevated pressure, a miscibility region still exists in the A-B binary system.

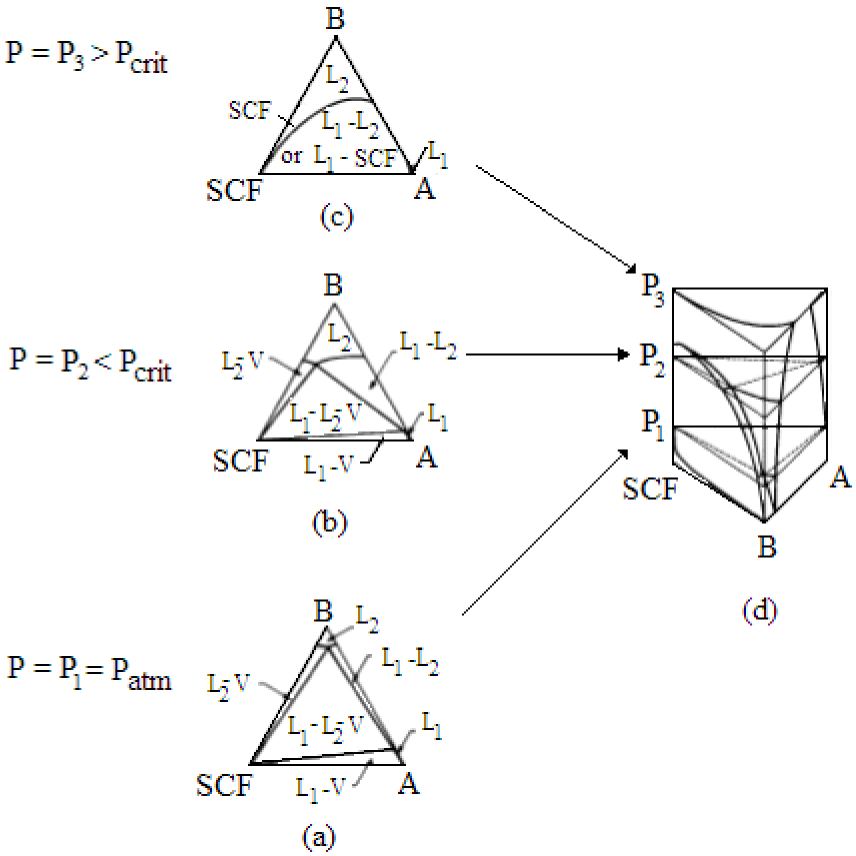

Figure 2.15. Phase Diagram for a Type III Ternary Mixture.

For Type III ternary systems, the liquid-liquid region increases with increasing SCF content (Figure 2.15b). Even if B is only slightly miscible with A at low pressures and in the absence of SCF, it is possible to use the SCF to separate even more A from B.

Although the classification for ternary systems is described here at a fixed temperature, it is important to remember that any single binary system can exhibit all three types of phase behaviors as the temperature of the system changes. This implies that a Type I ternary system may behave as a Type II or Type III ternary system if the operating temperature and pressure are adjusted to values near the critical point of the SCF solvent.

2.8. Phase Diagrams for Polymers

An important subset of high-pressure phase diagrams is the one for polymer-SCF mixtures. The scientific interest in the high-pressure phase behavior of polymer solutions was initially motivated by the technology required to make polyethylene.

In order to facilitate the study of this system, the polymer is considered as a pseudo-single component, describing the phase behavior by using the same diagrams presented before.

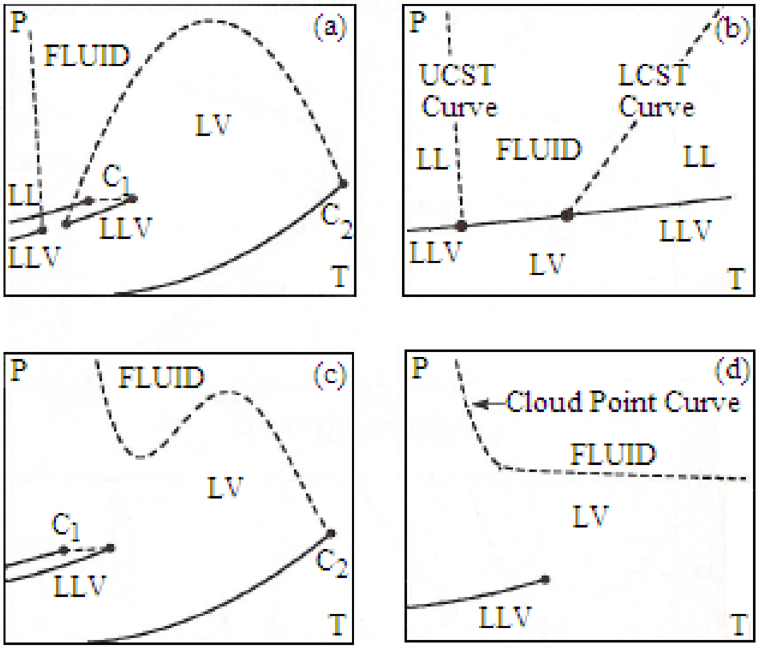

Figure 2.16. P-T Diagram for a Polymer-SCF System.

Figure 2.16a shows the schematic P-T diagram for a Type III (small polymer molecules) system where the vapor-liquid equilibrium curves for two pure components end in their respective critical points, C_1 and C_2. The steep dashed line in Figure 2.16a at the lower temperature is the P-T trace of the UCST curve. The other critical mixture curve shown in Figure 2.16a starts at the critical point of the less volatile component, shows a pressure maximum, and intersects an LLV region at conditions usually close to the critical point of the more volatile component. The portion of the curve named LCST is where the two phases (liquid-liquid) coalesce into a single phase when the temperature is lowered at a constant pressure.

Figure 2.16b shows the P-T diagram for a pseudo-binary polymer-solvent mixture that is similar to the diagram given in Figure 2.16a. It this case the large difference in the molecular size of the mixture components (polymer and carbon dioxide) suppress many of the features of the phase diagram shown in Figure 2.16a. A pure polymer does not have a critical point or vapor pressure curve, so the high temperature portion of the critical mixture curve does not exist in Figure 2.16b.

Both the UCST and the LCST branches of the chemical mixture curve are usually referred to as cloud point curves. For polymer-solvent systems, the pressure or temperature interval for a clear to totally opaque fluid to liquid-liquid transition along the UCST or LCST curves can be one hundred times greater than the interval for small molecule systems. The phase transition is not very distinct; it just progressively gets cloudier and cloudier, and so the name cloud point.

UCST curve for a polymer-solvent system is usually attributed to enthalpy interactions between the mixture components, which are not affected by small pressure changes. However the LCST curve is usually attributed to the large difference in the thermal expansion or free volume of the polymer and solvent. As the mixture is heated, the solvent expands at a much faster rate than the polymer, so that the dissolution of the polymer in the solvent is associated with a large decrease in the change of entropy of mixing. This entropy decrease occurs as solvent molecules are forced to condense around the polymer to dissolve it. At the end the amount of entropy released while forming a single phase is so great that the free energy of mixing becomes positive and the solution splits into two phases.

Figure 2.16c shows a Type IV P-T diagram that could take place with small molecule mixtures if the difference in size and/or the intermolecular potentials of the mixture components becomes very large. The occurrence of the phase behavior shown in Figure 2.16c can be tracked back to Figure 2.16a. As the disparity in the properties of the two components increases, the temperature range between the UCST and the critical mixture curves shown in Figure 2.16a becomes smaller and smaller. Eventually the difference in properties of the mixture components becomes so large that the UCST and critical mixture curves merge into a single critical mixture curve, exhibiting a pressure minimum at low temperatures.

Figure 2.16d shows how Figure 2.16c is transformed into a polymer-solvent system where the cloud point curve is the result of combining the LCST-type transitions at high temperatures and the UCST-type transitions at lower temperatures.

The molecular weight distribution of the polymer also has another effect on the phase diagram; Figure 2.16b shows that at pressures below the LLV line, the vapor and the liquid phases exist in equilibrium, but if the molecular weight distribution of the polymer is large, the LLV line becomes an area. This is because the system is now truly a multi-component system and the LLV line shown in Figure 2.16b in fact represents the highest pressure at which three phases exist for a highly poly-disperse polymer.

2.9. Modeling Supercritical Fluid Equilibria

In order to be able to design and evaluate supercritical fluid processes, it is essentially useful to have accurate models. Unfortunately, the properties that make SCF so useful such as: the high compressibility, the asymmetry of the system and the mathematical singularity of the critical point itself make modeling it difficult.

There are quite a few models for supercritical phase equilibriun most of them the SCF phase is treated as a dense gas and an equation of state (EOS) is used to calculate the fugacity coefficient.

When a supercritical solvent and a solute *i* are in equilibrium, the fugacity of the component *i* in the supercritical fluid phase can be determined with the following equation:

$$f_i^{SCF}\left(T, P, y_i\right) = y_i\, \phi_i^{SCF}\, P \tag{1}$$

In this approach the results are susceptible to the composition dependence of the interaction energies and size factors, making mixing rules extremely important. Another difficulty in this approach is that to estimate the fugacity coefficient in a supercritical phase requires the integration through the critical region where most EOSs are less accurate.

Another approach considers the SCF phase as an expanded liquid, and as a result the fugacity is given by:

$$f_i^{SCF} = y_i\, \gamma_i\left(y_i, P^o\right) f_i^{oL}\left(P^o\right) \exp\left(\frac{1}{RT}\int_{P^o}^{P} \frac{\bar{v}_i}{R\,T}\, dP\right) \tag{2}$$

where:

γ_i : Is the composition dependent activity coefficient at the reference pressure.

P^o: Reference pressure.

f^{oL}: Is the fugacity of the pure reference liquid.

$\bar{v}_i$: Is the partial molar volume of component *i*.

If the reference pressure is supercritical, it is not necessary to make the integration on the critical region; however, an EOS should be used to calculate the partial molar volume and a reference activity coefficient will be required.

When working with solids, the cubic equations cannot predict the fugacity, and for this reason it will be determined by modeling *i* as a pure component, and the fugacity equation obtained will be:

$$f_i^S(T,P) = P_i^{sat}(T)\phi_i^{sat}(T)\exp\left(\frac{1}{RT}\int_{P_i^{sat}}^{P}\nu_i^S\,dP\right) \qquad (3)$$

where:

f_i^S : Fugacity of a component *i* as a pure solid phase.

$P_i^{sat}(T)$: Sublimation pressure of the pure component at the same temperature.

ν_i^S : Molar volume of the pure solid.

$\phi_i^{sat}(T)$: Fugacity coefficient at T and P_i^{sat} (correction factor for high pressure).

$\exp\left(\frac{1}{RT}\int_{P_i^{sat}}^{P}\nu_i^S\,dP\right)$: Pointing correction factor.

The volume of the solid can be considered constant for a given temperature (T), so the pointing correction factor is simplified to: $\exp\left[\left(P - P_i^{sat}\right)\nu_i^S/RT\right]$.

Following the same analysis the fugacity coefficient for a pure solid $\phi_i^{sat}(T)$ at a given temperature can be considered one (1) since the saturation pressure for a solid is less than 1 bar. Then considering all these simplifications in equations 1 and 3, the solubility for a heavy solid in supercritical fluid can be determined with the following equation:

$$y_i = \underbrace{\frac{P_i^{sat}}{P}}_{\text{Ideal}} \; \underbrace{\frac{1}{\phi_i^{SCF}}}_{\text{Non-ideal}} \; \underbrace{\exp\left[\frac{\left(P - P_i^{sat}\right)v_i^{S}}{R\,T}\right]}_{\text{Pointing correction}} \qquad (4)$$

The fugacity coefficient of the solid in the SCF phase is the most important variable in this equation, representing the solubility increase as the gas is compressed into the critical region. The fugacity coefficient describes the non-ideal behavior observed when the gas density increases from ideal gas values at very low pressures, where the molecular interaction is much lower compared to liquid-like densities at high pressures. At a fixed temperature, the solubility increases in the supercritical fluid solvent with pressure increments, as ϕ_i^{SCF} decreases much more rapidly than the pressure increases or than the exponential term in the numerator increases, particularly near the critical point.

The most widely used method of analysis for supercritical equilibrium systems are Equations of State (EOSs). Cubic EOSs are easily extended to multi-component systems by using mixing rules. They can be derived by considering a first order perturbation with a hard sphere reference system and making some simplifications and assumptions. The most basic EOS known is the van der Waals (vdW), obtained by considering that the integral of the perturbing intermolecular potential for a pair of molecules is constant. The vdW EOS can predict almost all types of phase behaviors qualitatively, but not necessarily quantitatively. Other EOSs like Redlich-Kwong (RK) (1949), the Soave modification of Redlich-Kwong (SRK) (1972) and the Peng-Robinson (PR) equation (1976) incorporated some improvements, like the assumption that the perturbing intermolecular potential is temperature and density dependent, calculating the parameters from critical properties and optimizing the parameters by fitting pure component vapor pressure or liquid molar volume data.

Another model successfully used to describe liquid phase behavior in highly asymmetric polymer solutions is the Lattice-Gas EOS. The lattice-gas model is based on the distribution of molecules and holes, or vacant lattice sites, in a three dimensional lattice. Lattice models have been used to address the fact that the behavior in the immediate vicinity of the critical point is non-classical and cannot be described by classical EOS like vdW. Non-analytical lattice-gas models have been developed that are accurate in the critical region. Wheeler (1972) developed an equation able to describe the limiting behavior of dilute solutions near the critical point. Gilbert (1986, 1987) described a lattice-gas model able to fit molar volume and solubility data for highly asymmetric SCF-solid mixtures using two adjustable parameters.

When working with polymers and SCF at high pressures, a lattice-gas model is recommended, as the pure component properties are calculated assuming that each component can be broken into small parts (mers), and these parts will each have their own particular hole or space (lattice), generating a specific density for system. Flory's research group developed the theory of solutions (1964-1970) known as Flory's theory, where they were able to demonstrate that the thermodynamic properties of a mixture depends in the thermodynamic properties of the pure components. For example, the

LCST behavior normally observed of polymers phase diagrams, is a consequence of the differences on the thermodynamic properties of the polymers and solvent components in the mixture. Flory's model does not apply for systems where there are strong specific interactions; to dilute solutions and it neglects the free volume effect.

In 1977 Sanchez-Lacombe developed a lattice-fluid theory, in which the vacancies or empty lattice sites are accounted for the compressibility and density changes. This model does not require separation of internal and external degrees of freedom, as in Flory's theory. External degrees of freedom are attributed only to intermolecular forces, and internal degrees of freedom are related to intra-molecular chemical bond forces.

Perturbation models such us the Statistical Associated Fluid Theory (SAFT) developed by Chapman *et al*. (1990) are more sophisticated than the lattice-fluid models. This theory has a wider range of applicability, since the mixture density is considered a function of pressure, temperature and composition. This EOS considers the association between resembling molecules and solvation between contrasting molecules. This makes the theory more accurate, but at the same time more complicated, since additional equations and parameters are required.

SAFT is an EOS that incorporates terms to describe the molecular size and shape (including chain length and branches), association energy (like hydrogen bonds) and dispersion. The reference part of SAFT includes hard-sphere, chain and association terms, while the perturbation part of SAFT accounts for mean-field dispersion effects. The characteristic parameters for the pure substances involved in a mixture can be determined from vapor-liquid equilibrium data (VLE), vapor-pressure-temperature data

(VPT) or from the molecular weight. All this makes SAFT an attractive method to use, when using well known and characterized components. However when working with substances like the one required for this research, Chitosan Oligosaccharide Lactate, this model is difficult to use, since no molecular properties, VPT or VLE data are published.

A technique that complements all the methods already mentioned are computer simulations, which are not yet effective tools for modeling SCF phase equilibria due to the non-analytic nature of the results and the time consuming computing calculations. Still, the calculations may provide a good approach on the molecular level to outline the basis for improved mathematical models. Monte Carlo simulation has been used to predict SCF equilibria with an isobaric-isothermal assembly which accounts for density fluctuations to calculate solid solubility in SCF. Qualitative and quantitative agreement were obtained using Lennar-Jones potentials, plus quadrupole interactions for the system naphthalene-SCCO$_2$.

Working with polymers in a multicomponent supercritical mixture is a complex problem, where most of the theoretical approaches cannot accurately predict the thermodynamic interaction of such a different conglomeration of molecules. The use of global phase diagrams provides a logical method to investigate the phase behavior of simple and complex mixtures. Initially this technique was applied for simple binary mixtures (Deiters and Pegg 1989, Lamm and Hall 2001, Patel 2008, Patel and Sunol 2009), while lately the interest has turned to more complex systems like polar substances and polymer mixtures (Kraska 1996, Yelash and Kraska 1999, Polishuk et al. 2000).

When generating a global phase equilibrium diagram from EOS, the boundaries between the different types of phase behavior can be obtained by calculating high order thermodynamic states, which represent transition states between different types of phase behavior. In order to work with multicomponent mixtures, sub-systems of binaries can be studied separately and used as pseudo pure substances.

As presented in this section, there are different approaches to model phase equilibria for SCF, and no single model will work for all situations. The compromise between accuracy and convenience will always exist.

CHAPTER 3

SUPERCRITICAL ENCAPSULATION TECHNIQUES

In this chapter, a review of published papers and patents on particle encapsulation using different supercritical techniques and their classification according to the different concepts currently used is made. Encapsulation methods using supercritical fluids basically follow two tracks: the homogeneous supercritical solution track or the heterogeneous multi-phase track. In addition, the heterogeneous track contains a sub-classification where the carbon dioxide possibly combines with a cosolvent, or can be used as a solvent or antisolvent for the encapsulant material. A set of tables are presented in Appendices A and B contain summarized information (Papers and Patents) for the different SCF techniques used to encapsulate particles in the size range from 0.5 to 500 μm for different industrial applications. For this work, the term particle encapsulation indicates that a core solid material is covered by a shell or coating material. This term can be used for single core encapsulation (Encapsulated Single Particle) or multiple core encapsulations (Encapsulated Particles).

At this point it is helpful to recap some information introduced in Chapter I. Encapsulation of fine particles to produce tailored surface properties is currently a key development of supercritical fluids applications, in areas like: pharmaceutical, nutraceutical, cosmetic, agrochemical, electronic and specialty chemistry industries. A direct result of the industrial application is that a considerable number of publications and patents are filed every year. This chapter presents a review of published information classified according to the different concepts currently used to encapsulate particles, and is as comprehensive as possible.

During the encapsulation process, the particle surface can be engineered with specific physical, chemical, and/or biochemical properties by spreading a thin film of material on the surface of the particles. As a result, the flow-ability, dissolution rate, controlled release or masking, dispersability, chemical reactivity, bio-efficacy, and hydrophilicity of particles can be modified for a variety of applications.

Several traditional encapsulation processes are used at industrial levels. These can be classified into two broad categories with possible hybrid mechanisms: physical methods (vibrating nozzle, rotating disk, pan coating, fluidized bed, freeze-drying, spray drying, etc.) and chemical methods (coacervation, phase separation, interfacial polymerization, in situ polymerization, sol–gel methods, etc.). Usually these encapsulation methods require large amounts of organic solvents, surfactants, and other additives, leading to volatile organic compound (VOC) emissions and other waste streams. Other drawbacks include low encapsulation efficiency and further processing of the products such as downstream drying, milling, and sieving, which are usually necessary. In addition, residual toxic solvent in the end products, temperature and pH requirements, and strong shear forces are overwhelming challenges for maintaining the delicate structure of some chemical and biochemical ingredients.

Micronization and recrystallization of pharmaceutical compounds using supercritical fluids has many advantages over other traditional methods like spray drying, jet milling, grinding, and liquid antisolvent techniques. There has been growing interest in replacing conventional organic solvents with environmentally friendly supercritical fluids in chemical processes. Supercritical carbon dioxide ($SCCO_2$) became an excellent candidate due to its characteristics and properties: it has mild critical conditions (Tc = 304.1°K, Pc= 7.38 MPa), and is low cost, non-toxic, non-flammable, readily available, easily recycled, and as a solvent, it possesses a unique combination of gas-like diffusivity and liquid-like density and solvency (Krukonis 1985). At this point of time, $SCCO_2$ has been used as solvent or processing medium demonstrating successful results in numerous areas, initially with supercritical extraction and separation, and more recently with particle formation, coating and encapsulation (Yeo 1993, Reverchon 1998).

During the past decade, supercritical fluid processes have attracted increasing attention for particle engineering, including fine particle formation, coating, and encapsulation (Jung 2001). These have included Rapid Expansion of Supercritical Solutions (RESS), (Tsutsumi 1995, Wang T. J. 2001, Wang Y. 2002, Mishima K. 2000, Kim J. H. 1996, Tsutsumi A. 2003, Matsuyama K. 2003, Sun Y. P. 1998, Matsuyama 2003), Gas Antisolvent (GAS), and Precipitation with a Compressed fluid Antisolvent (PCA) (Falk 1997, Young 1999), also known as Aerosol Solvent Extraction System (ASES) (Bleich 1996) or Supercritical Antisolvent method (SAS) (Wang Y. 2005, Elvassore 2001, Wang Y. 2004, Duarte 2006).

Pressure or temperature changes can produce regions of supersaturation, which result in the formation of fine and uniform solid particles. The term supersaturation refers to a solution that contains more of the dissolved material than could be dissolved by the solvent under normal circumstances. Supersaturated solutions are prepared or result when the temperature increases at constant pressure, or the pressure increases at constant temperature of a saturated solution. Small particles (seeds) can trigger the separation of the dissolved material from the solvent.

When using supercritical fluids to produce solid materials independent of the technique used, two basic mechanisms of phase separation occur: nucleation or spinodal decomposition. If the initial condition from which the new phase is formed is metastable, the phase transition occurs by nucleation. If the starting condition is unstable, the phase transition occurs by spinodal decomposition.

Nucleation is an activated process where a free energy barrier must be eliminated in order to form a nucleus of the new phase within the metastable mother phase, while spinodal decomposition is a spontaneous process. The height of the nucleation free energy barrier is the result of the competition between the formation of an interface, which involves an energy cost, and the formation of a bulk stable phase, which is energetically favorable. The formation of a new phase by nucleation is the result of the activated growth of localized fluctuations of large amplitude. Nucleation normally occurs at nucleation sites provided by suspended particles or small bubbles; this is called heterogeneous nucleation. Nucleation without preferential nucleation sites is known as homogeneous nucleation (Debenedetti 1998).

In contrast, spinodal decomposition involves fluctuations of any amplitude that grow spontaneously, exceeding the critical wavelength. Spinodal decomposition is the preliminary procedure by which an unstable phase settles down to equilibrium. The type of perturbation considered in thermodynamic stability theory is large in extent but small in intensity, like a small density (or any intensive property) change occurring over a large-scale volume. In the thermodynamic viewpoint, loss of stability with respect to such perturbations occurs at a precisely specified condition: the spinodal (Figure 3.1).

In Figure 3.1, the binodal and spinodal curves merge at the critical concentration. Inside the binodal curve, the system is unstable and undergoes a spontaneous phase separation. Between the binodal and spinodal curves (shaded region), the system is metastable. Outside the binodal curve the system is fully miscible (one phase).

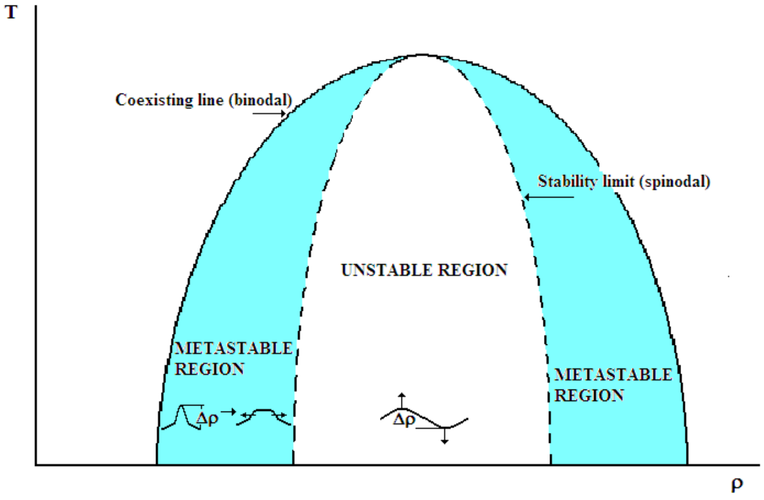

Figure 3.1. Phase Transition by Nucleation and Spinodal Decomposition.

In polymer systems the nucleation kinetics is significantly slower, leading usually to spinodal decomposition. The critical polymer concentration corresponds to the condition where $\left\lfloor \partial^3 \Delta G / \partial \varphi^3 \right\rfloor_{,P} = 0$, where the curvature of the free energy function is zero, at the spinodal point. The shape of the free energy function can be changed by adjusting temperature or pressure conditions. If the pressure is kept constant and the temperature is adjusted, two general polymer systems can be differentiated. Polymer systems that become miscible upon increasing the temperature are known as UCST

(Upper Critical Solution Temperature). Polymer systems that become miscible upon decreasing the temperature are known as LCST (Lower Critical Solution Temperature). These concepts, that are well known for polymer solutions at ambient pressures, are valid as well for solutions near and at supercritical conditions. At any pressure, depending on the nature of the combination polymer-solvent, the solution could display UCST or LCST or some combination of these (Kiran 1998).

In Figure 3.2, curve *a* represents a complete miscible system, and curves *b*, *c* and *d* represent the variation in shape of the free energy function which occurs when temperature is increased or decreased.

The route for particle synthesis and encapsulation using supercritical fluids basically follows two tracks: the homogeneous supercritical solution track or the heterogeneous track (Sunol 2001). On the heterogeneous track a sub-classification is suggested, where the CO_2 can be a solvent or an antisolvent for the coating material. The schematic explanation for each of these tracks is presented in Figure 3.3.

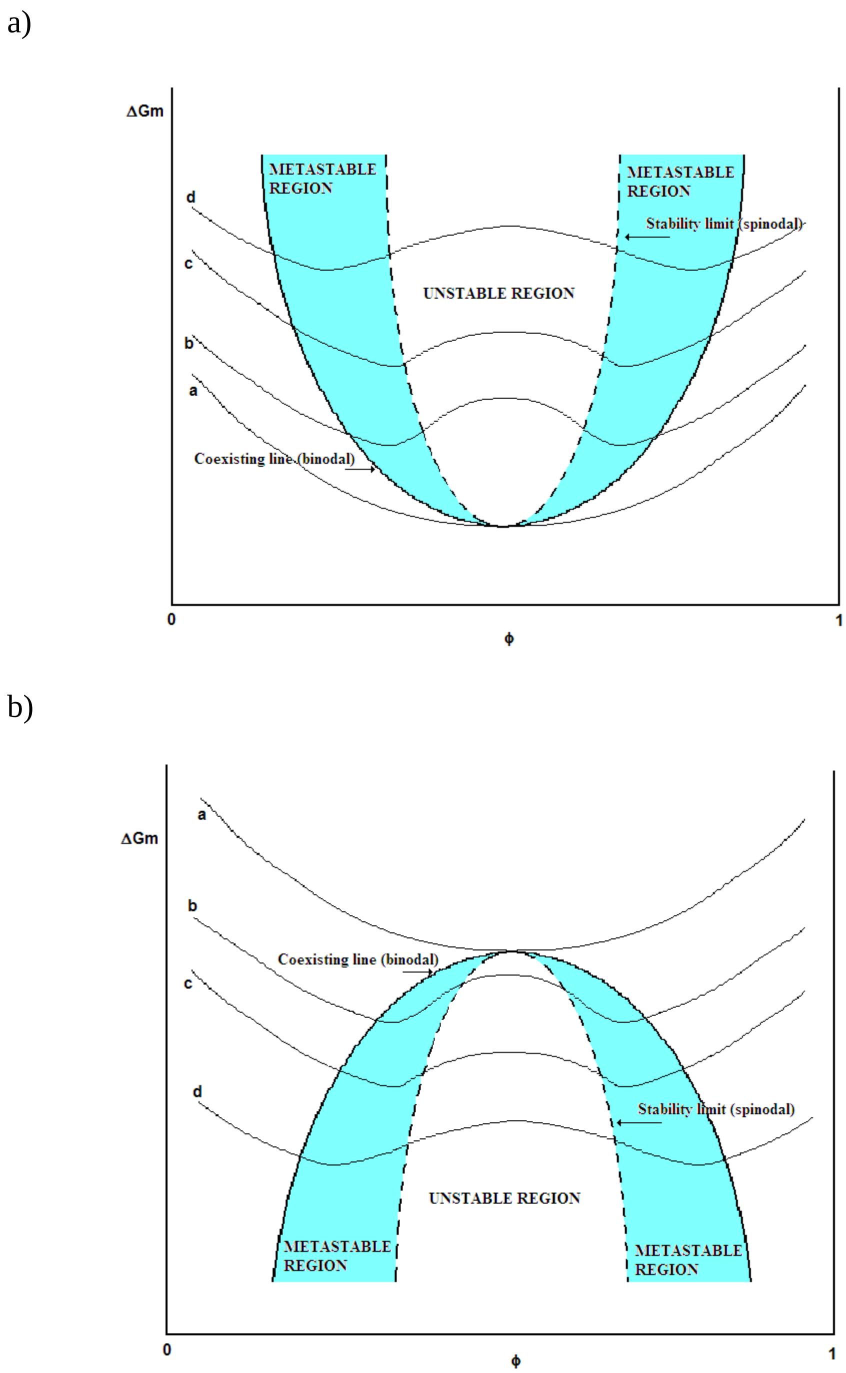

Figure 3.2. Binodal and Spinodal Curves in Polymer Systems. a) LCST and b) UCST

The morphology of the resulting solid material depends on the material structure (crystalline or amorphous, composite or pure, etc.) and of the RESS parameters (temperature, pressure drop, distance of impact of the jet against the surface, dimensions of the atomization vessel, nozzle geometry, etc.) (Tsutsumi 1995, Wang T. J. 2001, Wang Y. 2002; Mishima K. 2000; Kim J. H. 1996; Tsutsumi A. 2003; Matsuyama K. 2003; Sun Y. P. 1998; Matsuyama 2003).

Different methods have been described for the encapsulation of powders using RESS (Kim J. H. 1996) and its derived processes (Wang Y. 2002) obtained by coupling with a non-solvent (RESS-N) (Mishima K. 2000, Matsuyama K. 2003) or with a fluidized bed (Tsutsumi 1995, Wang T. J. 2001). All of them will be described in this review.

a)

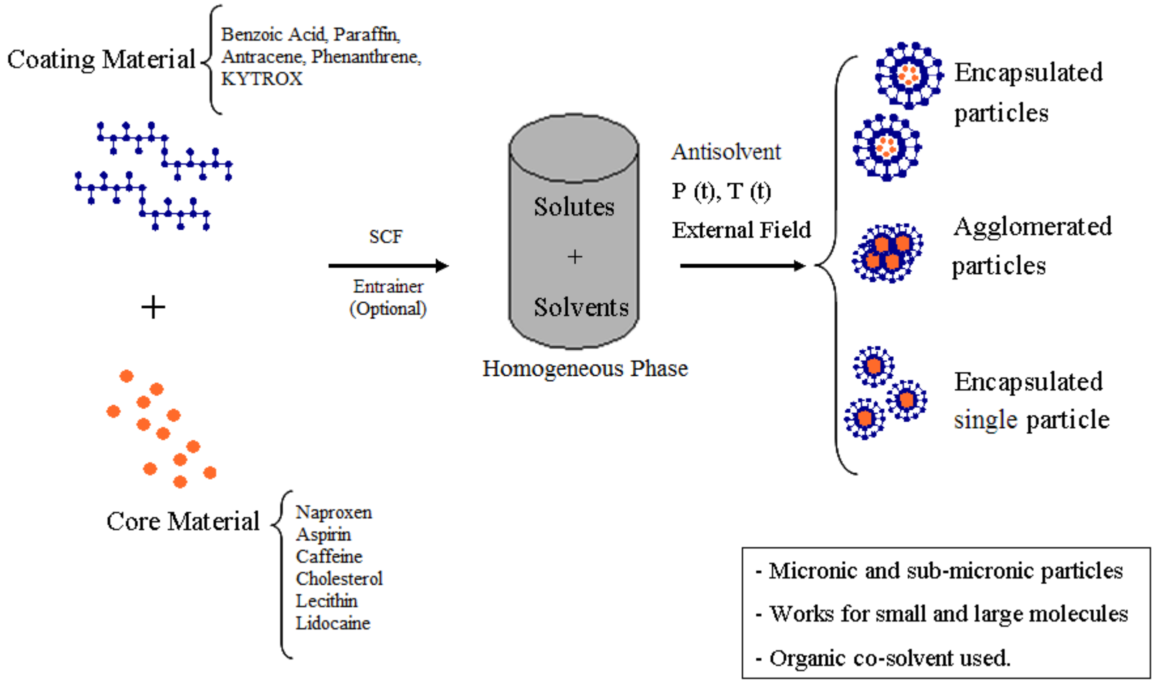

Figure 3.3. Route for Particle Encapsulation. a) Homogeneous track.
b) Heterogeneous track (CO_2 as a solvent). c) Heterogeneous track (CO_2 as antisolvent).

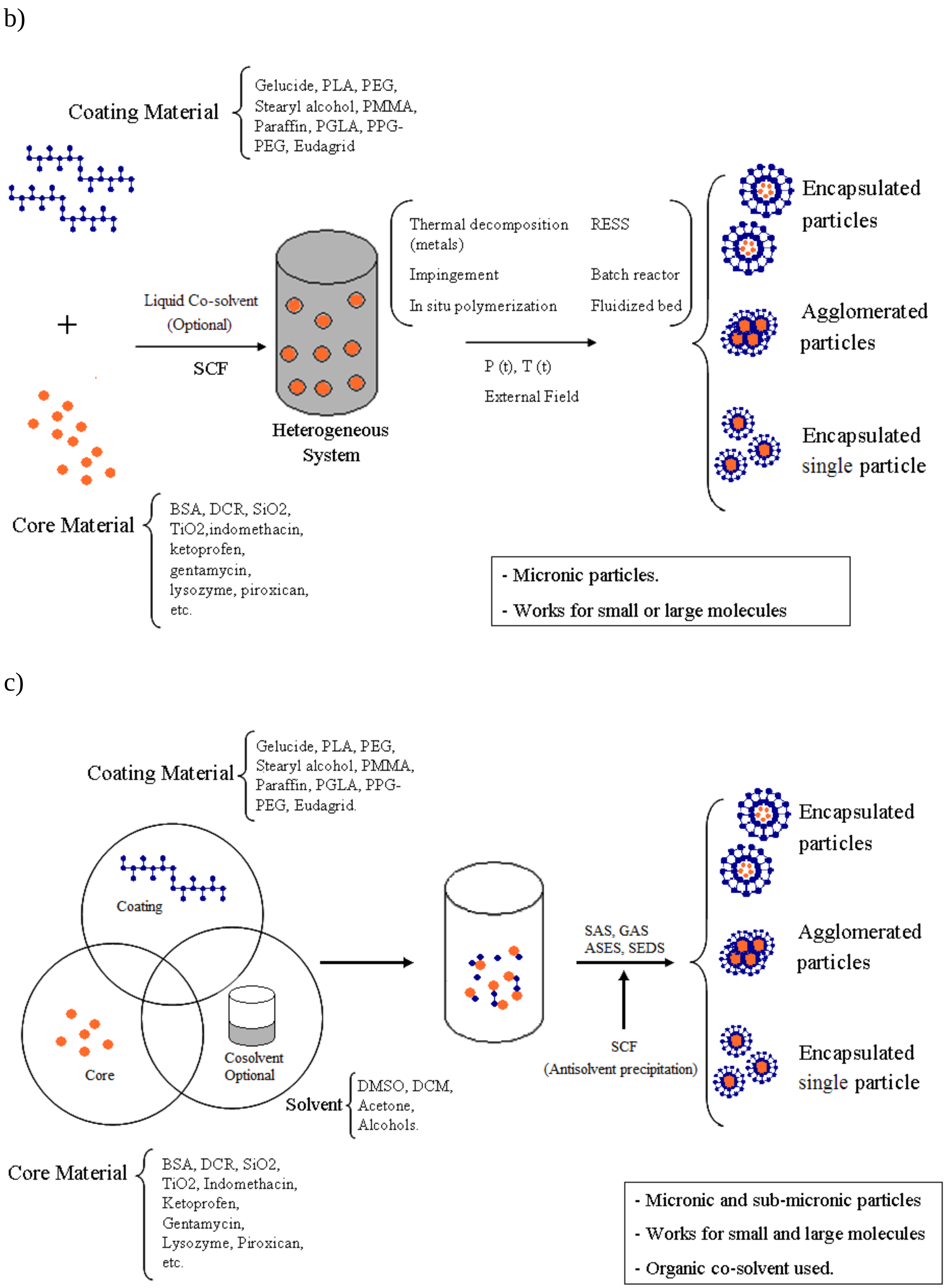

Figure 3.3. (Continued)

GAS (Gas Antisolvent) is also referred to as SAS (Supercritical Antisolvent). SEDS or Solution Enhanced Dispersion by Supercritical Fluids is a particular modification of this process, where the supercritical fluid is used as an anti-solvent that causes precipitation of the substrate(s) dissolved initially in a liquid solvent.

This method is based on the principle that a batch of solution is expanded several times by mixing with a supercritical fluid in a vessel, causing the solute precipitation. Due to the dissolution of the supercritical fluid, the expanded solvent has a lower solvent strength than the pure solvent. The mixture becomes supersaturated and the solute precipitates (Wang Y. 2005, Elvassore 2001, Wang Y. 2004, Duarte 2006).

An important feature of the SAS process is that the organic solvent can be almost completely removed by simply washing it out with pure CO_2 and as a result, dry particles are produced. Compared to RESS, the SAS process offers much more flexibility in terms of choosing suitable solvents. Furthermore, SAS has advantages over RESS because SAS is usually operated under mild conditions compared with those of RESS, which is associated with relatively high temperature and high pressure (Chang 1989, Matson 1987, Tom 1991).

ASES or PCA (Precipitation with a Compressed Antisolvent) is used when micro- or nano-particles are expected. The process consists of pulverizing a solution of the substrate(s) in an organic solvent into a vessel swept by a supercritical fluid, then spraying the solution through an atomization nozzle as fine droplets into compressed carbon dioxide. The dissolution of the supercritical fluid into the liquid droplets is accompanied by a large volume expansion, which leads to a reduction in the liquid solvent power. The weaker liquid solvent power causes a quick rise in the supersaturation within the liquid mixture and the consequent formation of small and uniform particles (Falk 1997, Young 1999, Bleich 1996).

PCA enables production of relatively monodispersed, sub-micron sized particles of biodegradable polymers. This process is quite flexible in terms of solvent choice, as well as for polymer and drug also. The only stipulations on solvent choice are that the compressed antisolvent can readily dissolve in it and expand it. Nearly all organic solvents meet these criteria.

Recent studies with PCA applied to drug processing have shown difficulties in incorporating the drug into the release matrix, as well as undesirable conformational modification of proteins. A process of dissolving ionic species in non-aqueous environments, Hydrophobic Ion-Pairing (HIP), was developed and successfully applied to these problems.

HIP is a technique whereby ionic pharmaceutical agents and proteins can be directly solubilized in organic solvents. It consists of pairing charged halves of the molecule with oppositely charged surfactants possessing some hydrophobic character, effectively increasing the molecule’s solubility in low-dielectric organic solvents by orders of magnitude. Anionic surfactants have been used exclusively for this work due to their low toxicity, while the cationic sites on the pharmaceutical compound or protein are masked with detergent molecules. The drug, surfactant, and residual water of hydration form what is referred to as a HIP complex. This technique makes it possible to obtain true homogeneous solutions of ionic compounds in neat organic solvents, with the only requirement being an accessible positive charge (Falk R. 1997).

Microencapsulation of pharmaceutical compounds in biodegradable polymer particles is of great interest for the development of new controlled drug-delivery systems. Several medical methods, depending on the required particle morphology, can be used for this purpose including, aerosol, inhalation, and systemic and subcutaneous injections. Typically, particles in to the range of 5-100 μm are subcutaneously injectable, 1-5 μm particles are suitable for aerosol delivery and inhalation therapy to the lungs, while nanoparticles can be directly injected in the systemic circulation. Even with a considerable number of studies of the preparation of pharmaceuticals coated with polymers for controlled release applications, the development of a micro-encapsulation method with environmentally benign solvents still remains a challenge. Solvent impurities are often toxic and also may degrade pharmaceuticals within a polymer matrix.

Polymers in general have very limited solubility in $SCCO_2$ at temperatures below 80°C (Lele 1992 and 1994, Tom 1994, O'Neill 1998). However, solubility can increase significantly at higher temperatures and very high pressures, often above 300 bar (Lele 1994, Tom 1991, Mawson 1995).

Another encapsulation method, well adapted for batch operation, involves polymerization on the particle surface in $SCCO_2$. This method is equivalent to the emulsion polymerization route in aqueous media, except that $SCCO_2$ is used as the polymerization solvent (Cooper 2000). $SCCO_2$ is a classical solvent used for polymerization reactions of methyl methacrylate, MMA (Wang W. 2002, Shiho 2000). More recently, encapsulation in $SCCO_2$ has been found to be of particular interest for recovering and processing metal oxide nanoparticles (Liu 2003). Metal powders are common components of pyrotechnic and solid propellants. Coating of metal powders reduces their deterioration through corrosion and aggregation caused by moisture or other aggressive surroundings. Coating of metal nanoparticles with polymers also reduces their flammability and makes them safe to handle. The technologies currently used in the industry for coating of solid substrates, such as the Wurster coating process or fluidized-bed coating, employ common organic solvents. Replacement of organic solvents with $SCCO_2$ could result in an alternative, environmentally friendly approach.

3.1. Homogeneous Pathway

Particle encapsulation using the homogeneous track is not very easy, since all the components (including coating material, core and cosolvent (if required)) should be soluble in $SCCO_2$, and after that they have to be precipitated following an appropriate sequence.

Kim Jong-Hyun (1996) used the rapid expansion of supercritical solutions (RESS) process to make polymeric microparticles or microspheres of poly-(L-lactic acid) (L-PLA) loaded with pharmaceuticals (naproxen) for drug delivery applications.

The liquid solvent carbon dioxide was compressed to the desired pressure by a high-pressure syringe pump. Before it entered the extraction vessel, the solvent was preheated up to the extraction temperature. The solvent entered the extraction vessel, loaded with L-PLA and naproxen mixture. Next, the saturated solution flowed to the pre-expansion unit wrapped with double-insulated heating tape to prevent phase changes upon expansion and choking problems in the capillary tube caused by premature precipitation of solute or solid CO_2. After that, the supercritical fluid solution was expanded through a capillary tube serving as the expansion device.

Several process variables were studied (*L*/*D* nozzle ratio, pre-expansion temperature, and extraction pressure) that could affect the morphology of the processed naproxen and L-PLA particles. Microspheres and some microspherical agglomerates dominated the morphology, L-PLA microspheres (10-90 μm) loaded with naproxen and some free naproxen microparticles (1-5 μm) were observed.

From the results presented, the presence of agglomeration is constant in almost all the experiments. This indicates that this is not a simple system, and an enhancement in the precipitation conditions (T-P) is required to make this step smoother. It is important to mention that all the precipitation methods presented in this chapter were initially used to make particles with a supercritical technique, and they have been adjusted for coating purposes, due to all the advantages that SCF offers.

From the information reviewed and following the classification used, the SCF precipitation methods are heterogeneous or homogeneous. In the heterogeneous ones there is a sub-classification where the CO_2 can be a solvent or an antisolvent for the coating material.

Homogeneous systems are less frequently used because solubility in CO_2 is limited to low-polarity substances. In addition to this, a homogeneous systems requires very fine control of the operation variables in order to be able to obtain the right deposition order. However, if all the conditions are given, this could be a powerful method where the deposition order, the particle size and the coating thickness would be tunable parameters.

In RESS processes, the nucleation phenomena is straightforward: as soon as the pressure decreases, the dissolved solute precipitates. However, it is not easy to control the thickness and uniformity of the coating, because this precipitation phenomena can happen in just 10^{-5} s. Another difficulty with a RESS process is the elimination of the cosolvent to trace levels, which sometimes can be a problem. However, this process is usually considered because the implementation costs are lower than in an antisolvent process and deposition will always occur.

Antisolvent processes are recommended for systems where the coating material is not soluble on the SCF. In this case an entrainer will be used, and the use of this technique will allow reducing the amount of cosolvent or entrainer to trace levels in the final product just by flushing it with pure CO_2. Rapid expansion techniques show better results when working with particles between 10-90µm, and antisolvent methods work reasonably well with particles under 10µm.

Using the data presented by authors cited in this paper, we see that the use of SCF in a fluidized bed improves the quality of the coating, but still when working with particles under 100µm, agglomeration is a common factor.

When temperature is used as the perturbation condition to initiate the precipitation, a better control and uniformity of the coating is obtained. This was confirmed in Sunol (1998), where an antisolvent process was described in which the precipitation was induced by a temperature change, allowing the formation of a coating film as thin as 0.2µm. Another author that used temperature adjustments in SCF to precipitate a coating over small particles (2-3µm) was Pessey (2000), who obtained a thickness of 0.2-1µm.

3.2. Heterogeneous Pathway

On the heterogeneous track, the ternary system integrated by a core substance, a coating material, an optional co-solvent and the supercritical solvent form the heterogeneous mixture. The supercritical fluid can be used as a solvent for the coating material, and a pressure or temperature perturbation is introduced to cause the precipitation. Another option can be using the supercritical fluid as antisolvent, where the mixture becomes supersaturated, thus precipitating the coating material.

3.2.1. Carbon Dioxide as a Solvent

What characterizes this particular coating track is that the coating material is completely soluble in pure $SCCO_2$, or in the system cosolvent-$SCCO_2$.

One of the first supercritical fluidized-bed coating processes with the rapid expansion of fluid solutions (RESS) was presented by Tsutsumi Atsushi (1995). Spherical catalyst particles (average particle size of 56 μm) were coated with paraffin by expanding a supercritical carbon dioxide solution of paraffin through a nozzle into a bed that was fluidized by air. Tsutsumi reported no significant agglomeration during coating and, using a gravimetric method, estimated the thickness of paraffin layer coated on the core particles to be below 0.5μm.

A new method for coating polymeric thin films on particles was achieved via simultaneous nucleation of polymeric material, by encapsulating the fluidized particles in the supercritical fluid, and further curing and binding the material coated on the particles, Sunol et al. (1998). A schematic description of the multi-purpose pilot plant used is shown in Figure 3.4.

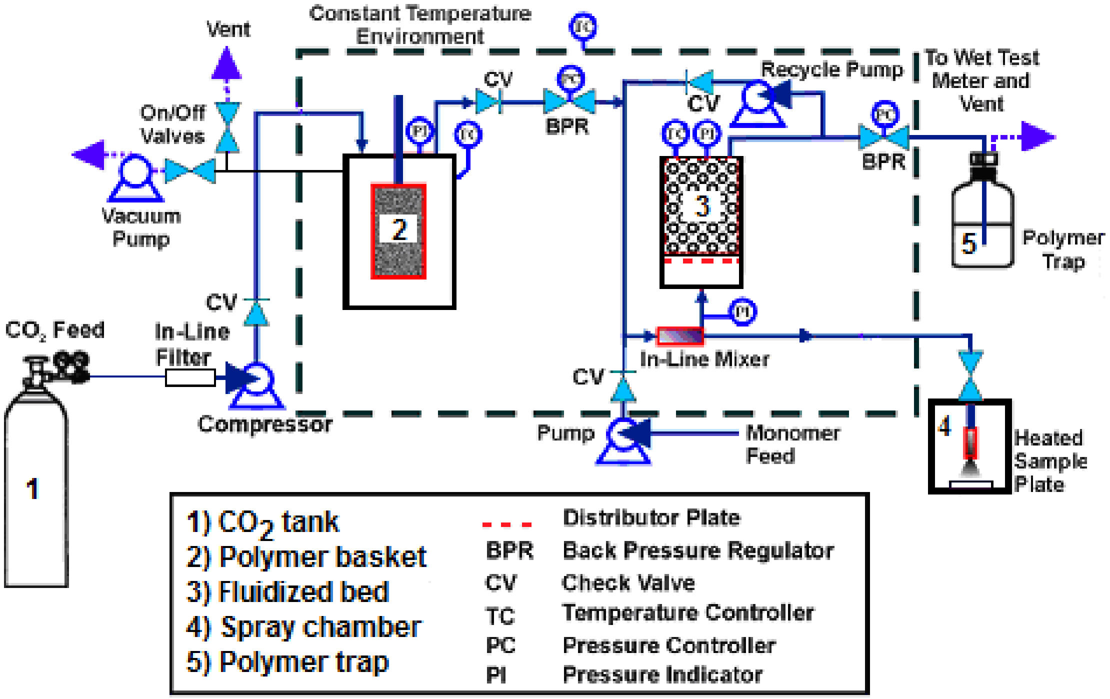

Figure 3.4. The Supercritical Fluid Aided Materials Processing Pilot Plant. (Sunol 1998)

The prototype system used carbon dioxide as the supercritical solvent and hydroxyl terminated poly butadiene (HTPB) as the polymer. The particles coated were sodium chloride crystals and ammonium nitrate, with a particle size range of 30-500 µm and film thickness as low as 0.2 µm.

The particles were fluidized with supercritical fluid recirculated through a recirculation pump in a closed loop. The loop was maintained at a low but supercritical temperature, while the fluidized bed was controlled at a higher temperature, in order to decrease the solubility, precipitating the coating material and promoting the polymerization. In order to achieve successful fluidization, the liquid feed containing monomer/polymer, catalyst, and the curative were introduced into the recirculation loop, which operated at a temperature that maximized solubility. The operation continued in the recycle mode until satisfactory level of coating and curing was achieved. Then, the system was shut down through a procedure that avoided further polymerization and precipitation of the polymer.

The surface characteristics of the polymer encapsulant were quite uniform. SEM and AFM both confirmed the deposition of a defect free, self-planarizing, encapsulating layer on the selected particulate materials.

This particular coating method can be distinguished from regular coating processes, since the precipitation is a consequence of a temperature increment instead of depressurization; this suggests a better control on the coating, given that the precipitation process is slower, providing more time for thermodynamic stabilization of the system.

In 2000, Pessey et al. presented particular “core-shell structures,” Ni/Cu and SmCo5/Cu, by thermal decomposition of bis(hexafluoroacetylacetonate)-copper(II) in the supercritical mixture CO_2/ethanol. Ni particles with an average diameter 3 μm and thickness of 0.2 to 1 μm were obtained.

The experimental system required a high-pressure reactor made of stainless steel and the internal walls covered with poly(tetrafluoroethylene) film (PTFE; thickness 0.25 mm) to avoid contamination of the cell’s wall. An external heating resistor allowed the precursor to reach the decomposition temperature. The temperature of the cell’s bottom was T_A, while the temperature of the cell’s top was maintained constant at T_B (with $T_B > T_A$), creating a convective movement produced by the temperature gradient ($T_B - T_A$). At the same time, the precursor decomposition occurred and released atomic copper, which coated the in-movement particles. The experimental set-up is shown in Figure 3.5.

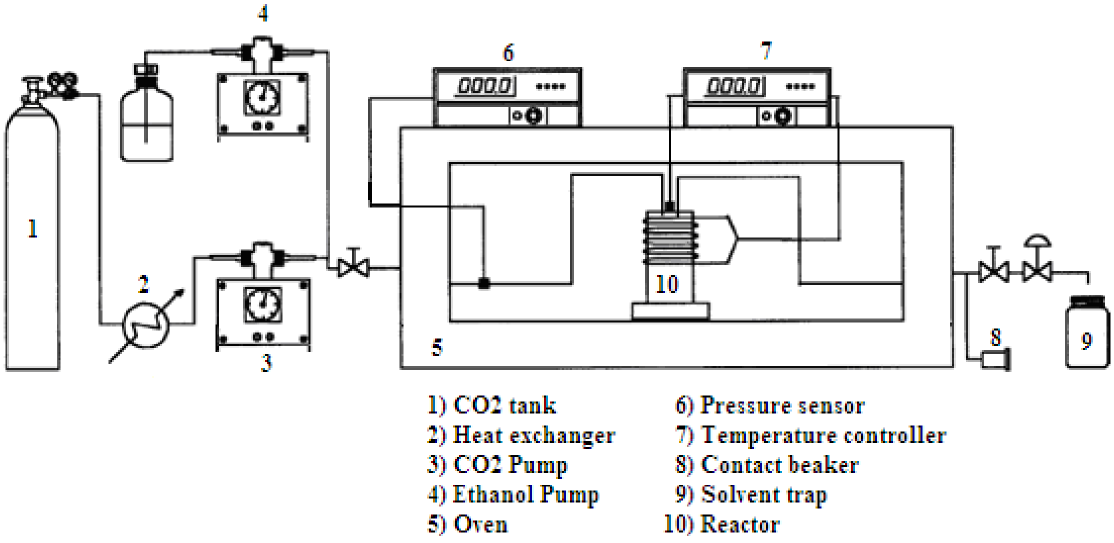

Figure 3.5. Apparatus for Particle Encapsulation by Thermal Decomposition.

A strong point of this process is that after the decomposition stage the organic part of the precursor is still soluble in the supercritical fluid and is easily removed when the vessel is vented and easily trapped at the outlet of the installation. After the return to ambient conditions, the coated particles are directly obtained free of solvent and organic contamination.

Mishima et al. (2000, 2001 and 2003) presented a rapid expansion method they named RESS-N, since they used a cosolvent (methanol, ethanol, propanol) that as pure component was a non-solvent for the coating material (poly ethylene glycol (PEG), poly(methyl methacrylate) (PMMA), poly(L-lactic acid) (PLA), poly(DL-lactide-co-glycolide) (PGLA) and PEG-poly(propylene glycol) (PPG-PEG) triblock copolymer). The solubilities of these polymers in CO_2 increased significantly with low-molecular weight alcohols as cosolvents. Particles of lysozyme (24 μm), lipase (19 μm), *p* acetamidophenol, acetylsalicylic acid, 1,3-dimethylxanthine, flavone, and 3-

hydroxyflavone (15 µm) and TiO_2 (35 and 320 nm) were coated following the procedure presented in Figure 3.6.

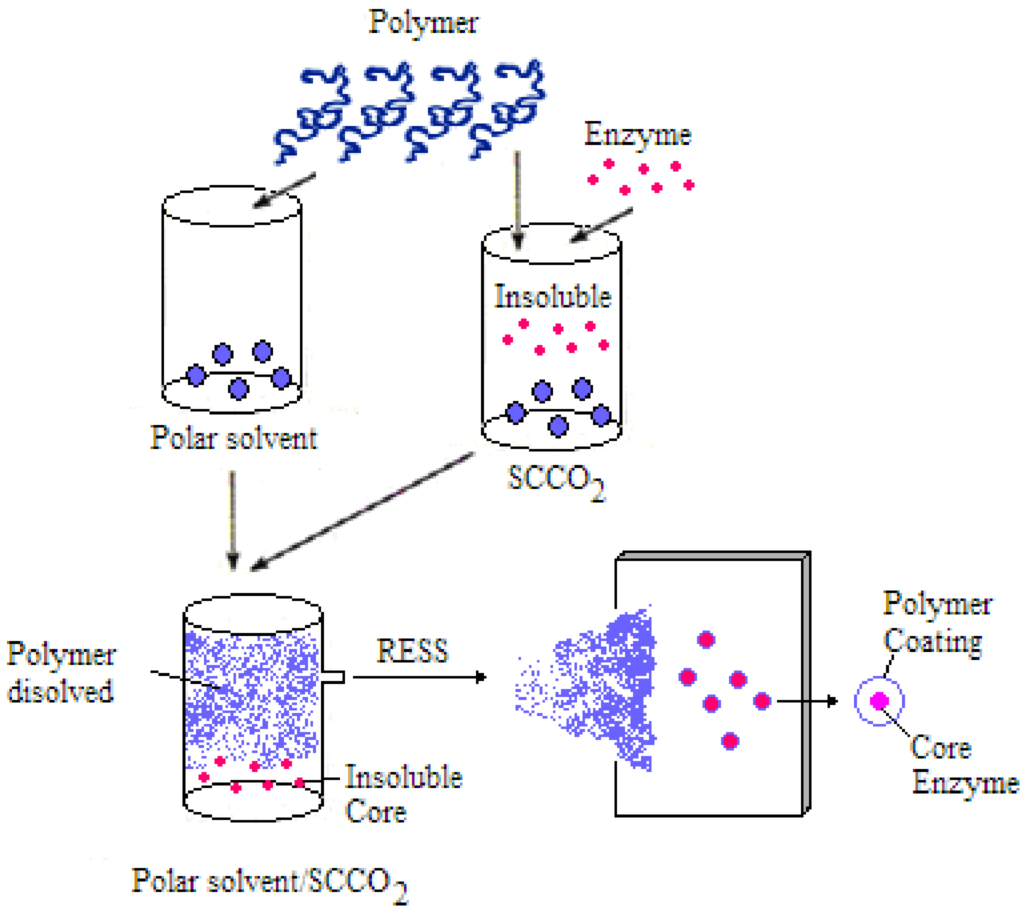

Figure 3.6. Formation of Polymeric Microcapsules by RESS-N.

With this work, the authors made a great contribution in the coating arena, since particles between 6 and 62 µm were coated with different polymers and the SEM results showed they got good coverage. The most important contribution was the development of a technique where the cosolvent could be easily removed from the final product, as evidenced by the amount of residual cosolvent in the microcapsules, which was less than 1 wt. %.

Glebov (2001) used $SCCO_2$ to apply polymeric films on fused silica plates and metal (Al, Mg) powders (20 μm). The polymers used were poly (vinylidene fluoride) and poly (4-vinylbiphenyl) (PVB).

Solutions of polymers in $SCCO_2$ were prepared in a batch stirred high-pressure temperature-controlled reactor, and samples of metal powders and/or of fused silica substrates were placed in an auxiliary vessel (sampling volume) connected to the reactor through a sampling valve. After the desirable reactor temperature was achieved, the sampling valve was opened and the auxiliary volume was connected to the reactor. After 10 min the sampling valve was closed, and the reactor was discharged to the atmosphere. The sampling volume was allowed to cool and then discharged. The thicknesses of the films reported were in the range of 1-30 nm.

In 2001, Wang Ting-Jie used a rapid expansion of supercritical fluid solution (RESS) process for the coating granulation of fine particles in a fluidized bed. He used CO_2 as a solvent, paraffin as a binder, fine particles of SiO_2 (d= 1μm) as coating material and glass beads as core particle (d=130 μm). What makes this process different is that core particles and fine particles were employed to simulate the drug-carrier and the drug in pharmaceuticals. The core particles carried the drug of fine particles to the human body and dispersed them. The releasing control of the fine particles was determined by the surface coating on the fine particles. The core particles and fine particles were mixed and fluidized before the rapid expansion of the supercritical fluid solution.

Like in other RESS processes, the paraffin was heated and extracted with $SCCO_2$. After extraction, the $SCCO_2$ solution of paraffin was expanded into the fluidized bed through the nozzle. Liquefied carbon dioxide was fed into the extraction column at a constant flow rate to keep the pressure constant in the column during the coating granulation process. The temperature at the nozzle inlet was found to be an important factor affecting the coating granulation process.

The rapid expansion of the supercritical solution caused a high supersaturating ratio of solute in the spraying flow, forming a large number of superfine nuclei. The superfine nuclei deposited on the surface of the particles formed a thin film. It was found that the fine particles were all covered with the thin film. The granules with fine particles attached were circulated through the spraying region and were covered with the binder or coating material in the region in the form of a film, resulting in the fine particles being cumulatively coated on core particles layer by layer.

Ribeiro Dos Santos (2002 and 2003) implemented a batch process to create solvent-free microparticles of bovine serum albumin (BSA) for sustained release using Gelucire 50/02 (which is a mixture of glycerides and fatty acid esters), Dynasan 114 or Trimyristin as coating materials.

The coating material and the BSA crystals were placed in an autoclave equipped with an impeller. The autoclave was sealed, heated and pressurized with CO_2 until the desired supercritical conditions were reached. Cooling the autoclave induced a pressure decrease and a phase change from supercritical to liquid state, thereby insolubilizing the coating material precipitated upon the insoluble BSA crystals dispersed in the medium. Afterwards, the autoclave was vented to ambient conditions and the coated particles were collected from the bottom of the autoclave.

The stability of BSA was evaluated by performing capillary electrophoresis and there was no apparent effect of the encapsulation conditions on the structural integrity of the protein. Gelucire 50/02 appeared to be a good coating material, since it did not crystallize such as Dynasan 114 and Trimyristin did. The coating was not found to be perfectly uniform: the outer surface of the coated particles exhibits some discontinuities and defects, with an average of two BSA crystals contained in each particle and a mean coated particle size of 500 μm.

One of the advantages of this process, compared to the homogeneous SCF process, is that the active material to be coated stays in its solid state during the whole process; consequently, biomolecules such as proteins used as drugs are less prone to denaturalization in process like this.

A modified RESS process for particle coating with a solution of polymer in supercritical CO_2 was studied by Wang Yulu (2002). This technique involved extracting the polymer (polyvinyl chloride-co-vinyl acetate (PVCVA) and hydroxypropyl cellulose (HPC)) with supercritical CO_2, with or without a co-solvent in an extraction vessel. Next, the polymer was precipitated onto the surface of host particles (glass beads, 315 and 500 μm) in a second precipitation vessel by slowly adjusting the pressure and temperature inside the precipitator to lower its solubility. The author reported an average coating thickness of 0.8 μm, with some agglomeration and uneven coating.

A rapid expansion of supercritical suspensions in impinging-stream reactors was presented by Tsutsumi (2003) for the coating of ultra fine particles with the coating layer (paraffin) in nanoscale. Silica particles with an average diameter of 1μm and titanium dioxide with the average diameter of 20 nm were used as core particles.

Measured amounts of ultra fine core particles and paraffin were loaded in the extraction column, then CO_2 was injected, and P and T were adjusted to get a SC mixture. After mixing, the supercritical suspensions were allowed to expand into the coating chamber through two capillary nozzles. The nozzles were heated to prevent clogging. During the expansion process, supercritical carbon dioxide was fed into the supercritical extraction column continuously to keep the pressure constant.

The impinging distance was observed to influence the coating rate of the ultra fine particles. The coating layer on the core particles was detected by the SEM observation. Thickness of the paraffin layer was around 50–60 nm. It was found that uniform film coating was successfully achieved in the single core silica particle and agglomeration was observed for titanium dioxide.

Another way to encapsulate particles is by dispersion polymerization in $SCCO_2$, as Yuea (2004) proposed. Dechlorane PlusR 515 (DCR) particles, with an average size of 12 μm were chosen as model host particles and were successfully encapsulated with poly(methyl methacrylate) (PMMA) and poly(1-vinyl-2-pyrrolidone) (PVP) polymers via in situ dispersion polymerization in supercritical carbon dioxide (Figure 3.7).

During polymerization, AIBN acted as free-radical initiator and PDMS-MA functioned as a surfactant. All components were premixed and charged into the reactor with CO_2 at room temperature until an appropriate pressure was reached.

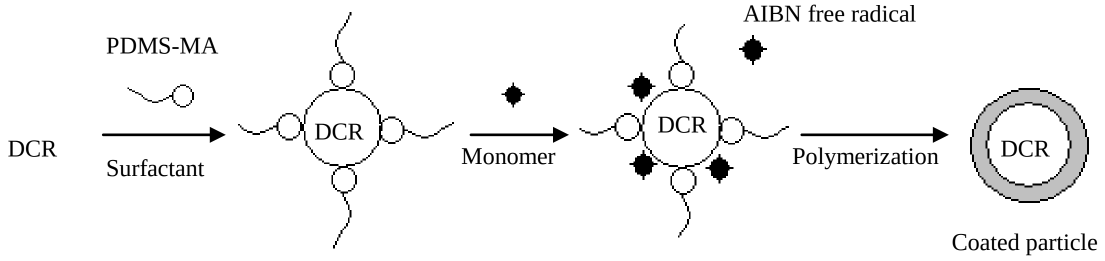

Figure 3.7. Radical Polymerization Mechanism.

Before the reaction started, the monomer, surfactant, and initiator were all dissolved in CO_2 and the heavy DCR particles stayed at the bottom of the vessel during the reaction. The vessel was then heated to initiate the free radical polymerization and the pressure reached its desired final value. Most of the experiments were run for 48 h (reaction time), after which CO_2 was released and the reactor was cooled down to room temperature followed by sample collection.

Results showed that the average particle size of 12 μm and the particle agglomeration observed was minor. As the authors stated, the polymer coagulation and the coating thickness could be controlled adjusting the Monomer/Core Material ratio and by adequate T-P operation conditions.

Kröber H. (2005) made a great contribution by using a fluidized-bed coating process with a rapid expansion of supercritical solutions (RESS) on the encapsulation of different diameters of glass beads (7.39 – 124.6 μm). He showed that it was possible to fluidize particles with a mean diameter of 7.4 μm, and he proved that the fluidization of particles under sub- or supercritical conditions was different from that under atmospheric pressure. With increasing pressure, the minimum fluid velocity necessary to start the fluidization decreased as the density of the SCF increased.

Supercritical carbon dioxide was used as solvent as well as carrier fluid for the core material creating the fluidized-bed. The coating material was stearyl alcohol (C18H38O). The apparatus consisted essentially of three subsections: the CO_2 supply, the extractor (in which the CO_2 becomes saturated with coating) and the high pressure reactor (where the coating takes place). The fluidized-bed reactor was filled with the core material and the bed was fluidized by adding pure carbon dioxide as “carrier fluid.” The reactor floor consisted of a perforated plate.

When the reactor reached thermal stability, the micro-encapsulation process was initiated. Carbon dioxide flowed through the extractor, saturated by the coating material, and then expanded through a nozzle into the fluidized-bed reactor. The expansion produced a fine aerosol of droplets that deposited onto the core particles, spreading out as a film and then hardening, yielding a solid layer of coating on the particles. Complete coatings with a layer thickness between 1 and 8 μm were achieved.

Another work in encapsulation based on an in situ polymerization for coating ceramic particles was presented by Hertz (2006). The YSZ powder (particle size 30 to 300 nm), the MMA monomer, the surfactant (PDMS-g-PA or FOMBLIN) and the initiator were introduced in the reactor containing pentane. The reactor was closed and the mixture stirred. CO_2 is non-polar whereas the oxide surface is polar; therefore, the surfactant molecules tended to assemble spontaneously at the surface of the particles with the polar or CO_2-phobe part anchored on the particles and the non-polar or CO_2-phile part dissolved in $SCCO_2$ under specific conditions (Calvo 2000, DeSimone 2001, Johnston 2000). Polymerization was carried out in $SCCO_2$ during 4 h at 30MPa and 150 °C. (Figure 3.8).

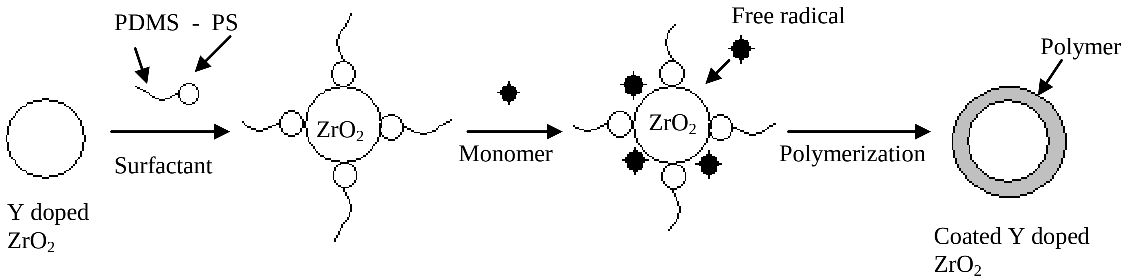

Figure 3.8. Schematic Description of the Proposed Mechanism for the Encapsulation of YSZ Powder by in Situ Polymerization in SCCO$_2$.

A number of attractive results were obtained from this preliminary study. The calculated thicknesses for the polymer shell were about 4.3 nm.

3.2.2. Carbon Dioxide as an Antisolvent

What characterizes this particular coating track is that the coating material is not soluble or has a low solubility in pure SCCO$_2$.

The aerosol solvent extraction system (ASES) used by Bleich (1996) exploited the fact that a supercritical gas was acting as non-solvent for an organic solution of the drug (hyoscine butylbromide, indomethacin, piroxican and thymopentin) and polymer (PLA) in order to form microparticles by a flocculation process. Due to the miscibility of the organic solvent used, methylene chloride, and the supercritical gas phase, microparticles with residual organic solvents below 30 ppm were formed.

The drug polymer solution (2%, w/w) was sprayed through a nozzle into the supercritical carbon dioxide phase. The spraying of the drug/polymer solution was followed by a drying process where CO$_2$ was pumped continuously. The microparticle size for all products was smaller than 50μm. Therefore, drugs with low solubility in supercritical carbon dioxide were preferable for this microparticle production technique.

Hydrophobic ion pairing (HIP) is a technique whereby ionic pharmaceutical agents and proteins can be directly solubilized in organic solvents while maintaining biological activity. It consists of pairing a charge on the molecule with oppositely charged surfactants possessing some hydrophobic character, effectively increasing the molecule's solubility in low dielectric organic solvents. Falk (1997) used this technique to coat low molecular weight pharmaceuticals like gentamycin, naloxone, and naltrexone, using supercritical carbon dioxide as the antisolvent, methylene chloride as a cosolvent and PLA as the polymer coating, in a compressed antisolvent (PCA) process.

In this process, carbon dioxide, the solvent containing the pharmaceutical compound and the polymer were pumped concurrently through an ultrasonic spray nozzle into a view cell containing carbon dioxide, at constant pressure and temperature. The cell was vented from the top so the precipitated particles could settle and be recovered directly from the chamber. The drug/polymer particles were spherical in shape and between 0.2 and 1.0μm in diameter, as determined by scanning electron microscopy. Drug incorporation efficiencies were determined and in vitro release profiles measured.

Young (1999) produced encapsulated Lysozyme (1-10 μm) by PCA method with some particular modifications that allowed him to avoid earlier limitations of massive polymer agglomeration and limited protein solubility in organic solvents.

The protein was encapsulated in biodegradable polymer, either poly-(*l*-lactide) (*l*-PLA) or poly(DL-lactide-*co*-glycolide) (PGLA) microspheres, which were precipitated from a dichloromethane solution after being sprayed into a CO_2 vapor phase through a capillary nozzle to form droplets which solidified after falling into a CO_2 liquid phase. By delaying precipitation in the vapor phase, the primary particles became sufficiently large, from 5 to 70 μm, such that they could encapsulate the lysozyme. At an optimal temperature of -20 °C, the polymer solution mixed rapidly with CO_2, and the precipitated primary particles were hard enough that agglomeration was markedly reduced compared with higher temperatures.

Upon completion of solution injection, the cell was filled with liquid CO_2. Liquid CO_2 was swept through the cell to remove the dichloromethane and further dry the particles. After drying, the cell was depressurized.

Elvassore (2001) achieved the microencapsulation of insulin with PLA using a mixture of cosolvents, dichloromethane and dimethyl sulfoxide, in order to ensure the solubility of both the polymer and the protein, to which the supercritical antisolvent was added.

In the SAS method, the liquid solution and the supercritical antisolvent were continuously added to the precipitation unit in concurrent or countercurrent mode and the particles formed were collected in the vessel. In the final step, supercritical CO_2 flowed into the vessel to wash and dry the precipitated products and after the cosolvents were extracted, the CO_2 was vented through an expansion valve.

It was found that the use of mixed solvents gave a suitable solution for the application of the SAS process. Submicron particles with no flocculation and agglomeration phenomena were obtained. The results showed that microspheres of PLA charged with insulin that were produced had average diameters ranging from 0.5 to 2 μm.

In the majority of the encapsulation procedures the common problem is agglomeration. In order to solve this problem, Wang (2004) used an ultrasonicator to break the nanoparticles agglomeration. Silica nanoparticles (hydrophobic and hydrophilic) were employed as host particles, Eudragit polymer as the coating material, acetone as cosolvent and supercritical CO_2 as the anti-solvent (SAS).

Eudragit was dissolved in acetone and the silica nanoparticles were suspended in the polymer solution, and an ultra-sonicator was used to break up the nanoparticles agglomerated in the silica–acetone suspension. When steady state conditions were reached in the high-pressure vessel, the polymer-silica–acetone suspension was delivered by a high-pressure pump and was sprayed through a stainless steel capillary nozzle into the high-pressure vessel containing $SCCO_2$. Thereafter, CO_2 was supplied to remove any residual organic solvent. When the cleaning step was completed, the high-pressure vessel was slowly depressurized and samples were collected for characterization.

The results revealed that 16–20 nm nanoparticles were successfully coated or encapsulated in polymer by the SAS coating process. The thickness of the polymer film was estimated to be around 10–40 nm, and appeared to be independent of surface hydrophilicity.

One year later Wang attempted to encapsulate fine submicron silica particles (0.5 μm) with a polymer for controlled release of drugs, poly(lactide-co-glycolide) (PLGA), using the same supercritical antisolvent (SAS) technique reported in Wang 2004.

The results showed that submicron silica particles were successfully encapsulated by PLGA in the form of loose agglomerates. It was found that the polymer weight fraction and the polymer concentration played critical roles in the agglomeration of the coated particles. A high polymer weight fraction favored the agglomeration of the coated particles and the uneven distribution of the polymer coating. A low polymer concentration appeared to prevent agglomeration among the coated particles. The operating pressure and temperature were also found to influence agglomeration. A higher pressure facilitated the agglomeration of coated particles as a result of sintering because the glass-transition temperature of the polymer, Tg, was depressed. The operating temperature appeared to have little effect on the agglomeration of the coated particles when the temperature was below the glass-transition temperature; however, when the operating temperature was above Tg, the polymer coating on the surface of particle appeared to be sintered, causing strong agglomeration. The flow rate of the polymer suspension was found to have little effect on the agglomeration.

CHAPTER 4

ENCAPSULATED PROTOTYPE SYSTEMS

Controlled release systems provide the benefits of protection from rapid degradation, targeted delivery, control of the release rate, and prolonged duration of bioactive agents. Controlled drug delivery systems have received considerable attention in recent years and they are providing in general a more controlled rate of uptake of the drug by the body. In this way, their therapeutic action is prolonged without increasing the dosage. One common way of controlling the release is by incorporating the drug in a polymeric carrier, and then the drug is released in the affected site by diffusion or surface erosion.

In conventional pharmaceutical applications, the active compound is rapidly and totally released in the body in a single burst. The concentration of the drug inside the body decreases with time (Figure 4.1a). At the beginning a peak is observed, and then as a function of time the concentration decays. One of the main problems in the traditional system is the possibility that the concentration–time curve crosses the toxicity limit for the active component. Every active substance presents two concentration limits: a lower limit, that represents the minimum concentration to obtain therapeutic effects, and the upper or toxicity limit, that represents the maximum concentration for which the undesirable effects are more important than therapeutic drug action.

The purpose of controlling the drug delivery is to achieve more effective therapies while eliminating the potential for both under and over dosing. Other advantages of using controlled delivery systems can include the maintenance of drug levels within a desired range, the need for fewer administrations, optimal use of the drug, and patient compliance (Figure 4.1b).

While these advantages can be significant, the potential disadvantages cannot be ignored. The possible toxicity or biocompatibility of the polymer coatings used, undesirable by-products of degradation, the chance of patient discomfort, and the higher cost of controlled release systems compared with traditional pharmaceutical formulations. For these reasons, research with biodegradable polymers has expanded considerably. These materials degrade within the body as a result of natural biological processes. Most biodegradable polymers degrade as a result of the hydrolysis of the polymer chains into biologically acceptable, and progressively smaller, compounds. In some cases (e.g. polylactides, polyglicolides and their copolymers) the polymers will eventually break down to lactic acid and glycolic acid, enter the Kreb’s cycle, further break down into carbon dioxide and water, and finally, are excreted through normal processes.

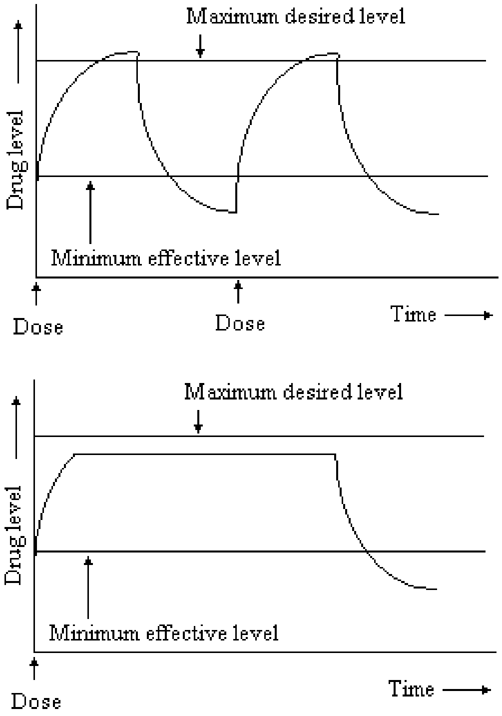

Figure 4.1. Drug Levels in the Blood.
(a) Traditional drug dosing, (b) Controlled delivery dosing.

The objective of this research was to develop a tunable and mild encapsulation technique capable of coating dried powder particles with a final size between 1 to 5 µm, since there are still a lot of room for improvement in this particle size range, as was shown in Chapter 3.

The particle should contain one core or active ingredient and a protective coating. Since the encapsulation method is in development, the simplest model was suggested (Figure 4.2).

In this chapter, the chemicals used in the encapsulation process will be described, including the rationale for their selection, their pertinent physical and chemical properties and their molecular structures.

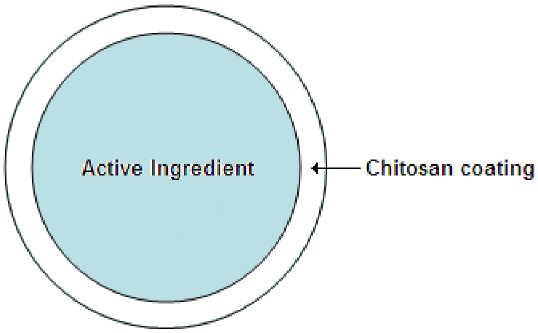

Figure 4.2. Coated Dry Powder Prototype.

4.1. Chitosan

Chitosan is a modified carbohydrate polymer derived from chitin deacetylation, as can be seen in Figure 4.3.

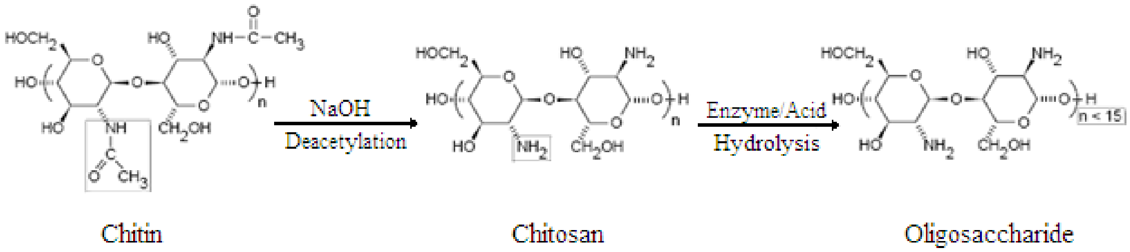

Figure 4.3. Preparation of Chitosan from Chitin.

Chitosan is used for nasal, ocular and oral drug delivery. Its use prolongs contact time and improves drug absorption. Furthermore, Chitosan is useful for gene delivery, due to its permanent cationic charge. It interacts electrostatically with negatively charged molecules like DNA to form complexes which are very stable and therefore it is able to condense DNA molecules, protecting the DNA against nuclease degradation.

In acidic mediums, the amine groups will be positively charged, conferring to the polysaccharide a high charge density which results in a strong electrostatic interaction with mucus and negatively charged mucosal surfaces, thereby increasing the permeability of an epithelium (Mansouri, 2004).

In addition to the properties mentioned in Table 4.1, Chitosan has the ability to cause tight junction disruption at the molecular level, enhancing drug delivery through tissues (Smith et al. 2004).

Table 4.1. Chitosan Properties.

Chemical properties	**Biological properties**
Cationic polyamine	Natural polymer biocompatible
High charge density at pH<6.5	Biodegradable to normal body constituents
Adheres to negatively charged surfaces	Safe and non-toxic
Amiable to chemical modifications	Hemostatic, bacteriostatic and fungistatic
High molecular weight linear polyelectrolyte.	Anticancenogenic
Viscosity, high to low (depending on Mn)	Versatile
Reactive amino/hydroxyl groups	Reasonable cost

Chitosan is a weak base and is insoluble in water at neutral and alkaline pH. Cancer or tumor cells have an acidic pH, making the amine groups in the Chitosan to be positively charged. As mentioned above, this confers to the polysaccharide a high charge density which results in a strong electrostatic interaction, which increases the permeability of the cell.

The versatility and tune-ability of this polymer is given by the combination of degree of deacetylation and molecular weight (Table 4.2), which promotes solubility in different environments (Köping-Höggård, 2003).

Table 4.2. Chitosan Classification (Sigma Aldrich)

Polymer	**Average Mn**	**% Deacetylation**	**Viscosity (cps)**
Oligosaccharide	< 5000	> 90	6
Low Mw	50,000-190,000	75-85	20-200
Medium Mw	190,000-310,000	75-85	200-800
High Mw	310,000-375,000	>75	800-2000

The specific polymer used in this research was Chitosan Oligosaccharide Lactate, (with a number average molecular weight Mn<5000, Sigma Aldrich 523682), as it is soluble at regular mucus pH 6.5, water and DMSO, which confirms a promising future application in pharmaceutical and food fields. Table 4.3 contains some physical properties of this polymer.

Table 4.3. Chitosan Oligosaccharide Lactate Physical Properties.

Property	**Value**	**Source of Information**
Physical form	Yellow powder > 90% deacetylation	Sigma Aldrich
Average MW	< 5000	Sigma Aldrich
MW (amu)	340.3	Sigma Aldrich
Density (g/cc)	1.4532 (22.6 °C) 1.4657 (28.6 °C) 1.4763 (35.3 °C)	Quantachrome Ulatrapicnometer 1000
Viscosity (cP)	6	In 1 % acetic acid, Sigma Aldrich
Soluble in	H_2O, DMSO, Acetic acid solutions (6-6.5 pH)	Determined experimentally (Chapter 5)

4.2. Carbon Dioxide (CO_2)

Carbon dioxide is a colorless, odorless gas. At standard temperature and pressure, the density of carbon dioxide is about 1.5 times that of air. The carbon dioxide molecule (O=C=O) contains two double bonds and has a linear shape. It has no electrical dipole, and as it is fully oxidized, it is moderately reactive and is non-flammable.

Supercritical carbon dioxide refers to carbon dioxide that is in a fluid state while also being at or above both its critical temperature and pressure, allowing for rather unique properties. Carbon dioxide usually behaves as a gas in air at standard conditions for temperature and pressure (STP) or as a solid called dry ice when frozen.

If the temperature and pressure are both increased from STP to be at or above the critical point for carbon dioxide, its properties are midway between a gas and a liquid. More specifically, it behaves as a supercritical fluid above its critical temperature (31.1°C) and critical pressure (72.8 atm), expanding to fill its container like a gas but with a density like that of a liquid (Figure 4.4).

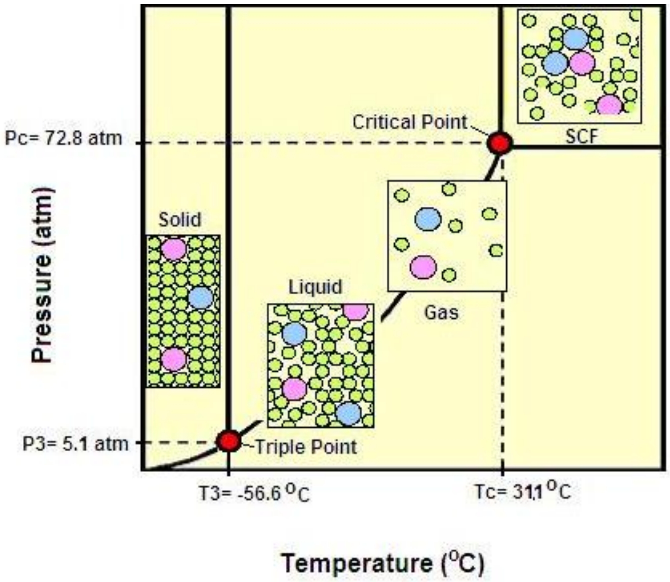

Figure 4.4. Supercritical Fluid Phase Diagram.

Supercritical CO_2 has become an important commercial and industrial solvent due to its role in chemical extraction, in addition to its low toxicity and environmental impact. It is a non-flammable solvent with low viscosity, high diffusion rate and no surface tension. The relatively low temperature of the process and the stability of CO_2 also allow most compounds to be extracted or dissolved with little damage or denaturing. The selective solvating power of carbon dioxide makes it possible to separate a particular component from a multi component mixture. Another big advantage for food and pharmaceutical applications is that CO_2 inactivates a wide variety of bacterial organisms, enabling the final product to be sterilized.

A drawback of CO_2 as a solvent, however, is that only volatile or relatively non polar compounds are soluble, as CO_2 is non-polar, and has low polarizability and a low dielectric constant. For this reason, a cosolvent is usually employed in the cases where the solute of interest is not soluble or has a very low solubility in pure supercritical carbon dioxide. Some of the properties of carbon dioxide are presented in Table 4.4.

Table 4.4. Properties of Carbon Dioxide (CO_2).

Properties	
Molecular weight	44.0095(14) g/mol
Appearance	colorless gas
Density	1,600 kg/m^3, solid; 1.98 kg/m^3, gas
Melting point	−78 °C (194.7 K) (sublimes)
Boiling point	-57 °C (216.6 K) at 5.185 bar
Critical temperature, Tc	31.03°C
Critical pressure, Pc	7.38MPa
Dynamic viscosity, μ	(1-9) x10^{-4} g/cm -s
Surface tension, σ	4.34 dyn/cm at 20°C
Solubility in water	1.45 kg/m^3
Acidity (pK_a)	6.35 and 10.33
Kinematic viscosity, ν	0.113x10^{-6} m^2/s at -10 °C
Dipole moment	zero
Heat capacity, c_p	183.1 J/mol·°K at 38°C, 8653 kPa
Enthalpy of vaporization (ΔH°vap)	15.326kJ/mol at -57.5°C
Enthropy of vaporization (ΔS°vap)	70.8 J/mol·°K at -57.5°C

4.3. Dimethyl Sulfoxide (DMSO)

Dimethyl sulfoxide, whose chemical formula is $(CH_3)_2SO$, is a by-product of wood pulping. This colorless liquid is an important polar aprotic solvent that dissolves both polar and non-polar compounds and is miscible in a wide range of organic solvents as well as water. It has a distinctive property of penetrating the skin readily, allowing the handler to taste it. Its taste has been described as oyster- or garlic-like. Some of the properties of the dimethyl sulfoxide are presented in Table 4.5.

Table 4.5. Properties of DMSO

Properties	
Molecular formula	C_2H_6OS
Molar mass	78.13 g/mol
Appearance	Clear, colorless liquid
Density, ρ	1.1004 g/cm^3, liquid
Melting point	18.5 °C (291.65 °K)
Boiling point	189 °C (462.15 °K)
Solubility in water	Miscible
Critical temperature, Tc	447°C
Critical pressure, Pc	57.1atm
Viscosity, μ	1.996 cP at 20 °C
Dipole moment	3.96
Heat capacity, c_p	153 J/mol·°K
Entropy, S	188.78 J/mol·°K
Enthalpy of formation, ΔH_f	-203.4 kJ/mol

DMSO is an important polar aprotic solvent, since it is able to dissolve a variety of organic substances, including carbohydrates, polymers, peptides, as well as many inorganic salts and gases, and is less toxic than other members of this family. Loading levels of 50-60 wt % are often observed vs 10-20 wt % with typical solvents.

Use of DMSO in medicine dates from around 1963 (Parcell 2002), when a University of Oregon Medical School team, headed by Stanley Jacob, discovered it could penetrate the skin and other membranes without damaging them and could carry other compounds into a biological system. In addition, because DMSO increases the rate of absorption of some compounds through organic tissues including skin, it can be used as a drug delivery system.

DMSO was selected for this research as an entrainer since the polymer (Chitosan) is highly soluble in it but not in pure carbon dioxide. Second, the fact that the liquid is transferred into the CO_2 under some specific P, T conditions and the non-solubility of the Chitosan in the mixture (CO_2 + DMSO) at that conditions were considered in order to design this new encapsulation method.

4.4. Calcium Oxide (CaO)

Calcium oxide is a white, caustic and alkaline crystalline solid commonly known as burnt lime, lime or quicklime; it is a widely used chemical compound, as a softener and pH regulator for water treatment, fertilizer, food industry, petroleum additives, glass, fiberglass and steel industry. On the food and pharmaceutical industry this chemical is used on the manufacture of antacid, dairy basic drinks, food complement, cheese, condensed milk, powder milk, cereals, pasta, protein products, and animal nutrition products, etc.

In this present work calcium oxide was used as it is readily available in a wide particle size range (less than one micron to 250 microns), low cost, non soluble in DMSO or SCCO2, non porous and well characterized. There is also value in micro-encapsulated calcium oxide products. Some of the properties of the calcium oxide are presented in Table 4.6.

Table 4.6. Properties of Calcium Oxide (CaO).

Properties	
Molecular formula	CaO
Molar mass	56.077g/mol
Appearance	White solid
Density	3350 kg/m^3, solid
Melting point	2572 °C (2845.15 °K)
Boiling point	2850 °C (3123.15 °K)
Thermal conductivity k, (cal/cm· s ·K)	0.019
Porosity ssa, (m^2/gr)	2-5
Solubility in water	reacts
Enthalpy of formation, $\Delta H_f°$	-635.09 kJ/mol
Entropy, S	38.19 J/mol·°K
Heat capacity, c_p	49.954 kJ/ mol·°K

4.5. Titanium Dioxide (TiO_2)

In terms of volume, Titanium Dioxide is one of the top fifty chemicals produced worldwide. It is a white, opaque and naturally-occurring mineral found in two main forms: rutile and anatase. Titanium dioxide has a variety of uses, as it is odorless and absorbent. From medicine to make-up and plastics to paper, hardly a day goes by when we do not use titanium dioxide. In powder form, titanium dioxide (TiO_2) is widely used as an intensely white pigment to brighten everyday products such as paint, paper, plastics, food, medicines, ceramics, cosmetics, and even toothpaste. Its excellent UV ray absorption qualities make it perfect for sunscreen lotions, too. It is also inert and biocompatible, making it suitable for medical devices and artificial implants. Titanium dioxide is what allows osteo-integration between an artificial medical implant and bone. Some of the properties of the titanium dioxide are presented in Table 4.7.

Table 4.7. Properties of Titanium Dioxide (TiO_2).

Properties	
Molecular formula	TiO_2
Molar mass	79.87 g/mol
Appearance	White solid
Density	4230 kg/m^3, solid
Melting point	1870 °C (2143 °K)
Boiling point	2972 °C (3245 °K)
Porosity ssa, (m^2/gr)	10-200
Solubility in water	insoluble

Like calcium oxide, titanium dioxide is widely available and well characterized. It is low cost, insoluble in DMSO or $SCCO_2$, and the particle size used is less than one micron and is porous. Experiments with TiO_2 allowed evaluating the effect of porosity on the encapsulation process.

CHAPTER 5

EXPERIMENTAL SYSTEMS AND PROCEDURES

In this chapter a description of all the experimental set-ups used during this research will be presented. This section includes set-up diagrams and the experimental procedures. Start up procedures, how to run the experiments, clean up and shut down protocols are included in the Appendices.

5.1. Solubility Systems

In determination of phase behavior of multi-component systems at high pressure, there are static and dynamic methods; these methods were reviewed in Chapter 2. Both techniques were used in this research and the experimental set-ups are presented next. Even though when using static systems just one sample mixture can be studied per loading, it requires minimum amounts of components and allows visualization of the phase transitions. Dynamic systems allow collection of large amounts of solubility and equilibrium data, but they require good handling of the operation conditions to avoid inaccurate solubility data.

5.1.1. Static Cloud Point (Phase Analyzer)

The experimental system used is shown in Figure 5.1. One of the most important components of the system was the Phase Monitor SPM20 (Thar Technologies), which consists of a high pressure variable–volume cell (5 – 15 ml) made in stainless steel where the mixture to be studied was placed. The temperature was controlled automatically between room temperature and 150±0.1 ºC. The pressure was adjusted manually using a mechanical syringe pump (Ruska 2200), and by decreasing the vessel volume the pressure was increased and vice versa. The pressure and temperature signals in the vessel were transferred to a portable PLC controller and the mixture behavior could be visualized on a video monitor.

A stirrer was used to obtain a homogeneous mix of Chitosan-DMSO-SCCO$_2$ inside the vessel. The phase behavior phenomena occurring inside the cell were visualized on a video monitor using a camera placed directly over a sapphire window.

The carbon dioxide used in this system was pumped with a syringe pump (ISCO 100DX) equipped with a cooling jacket to assure that the CO$_2$ withdrawn from cylinder tank remained in the liquid phase.

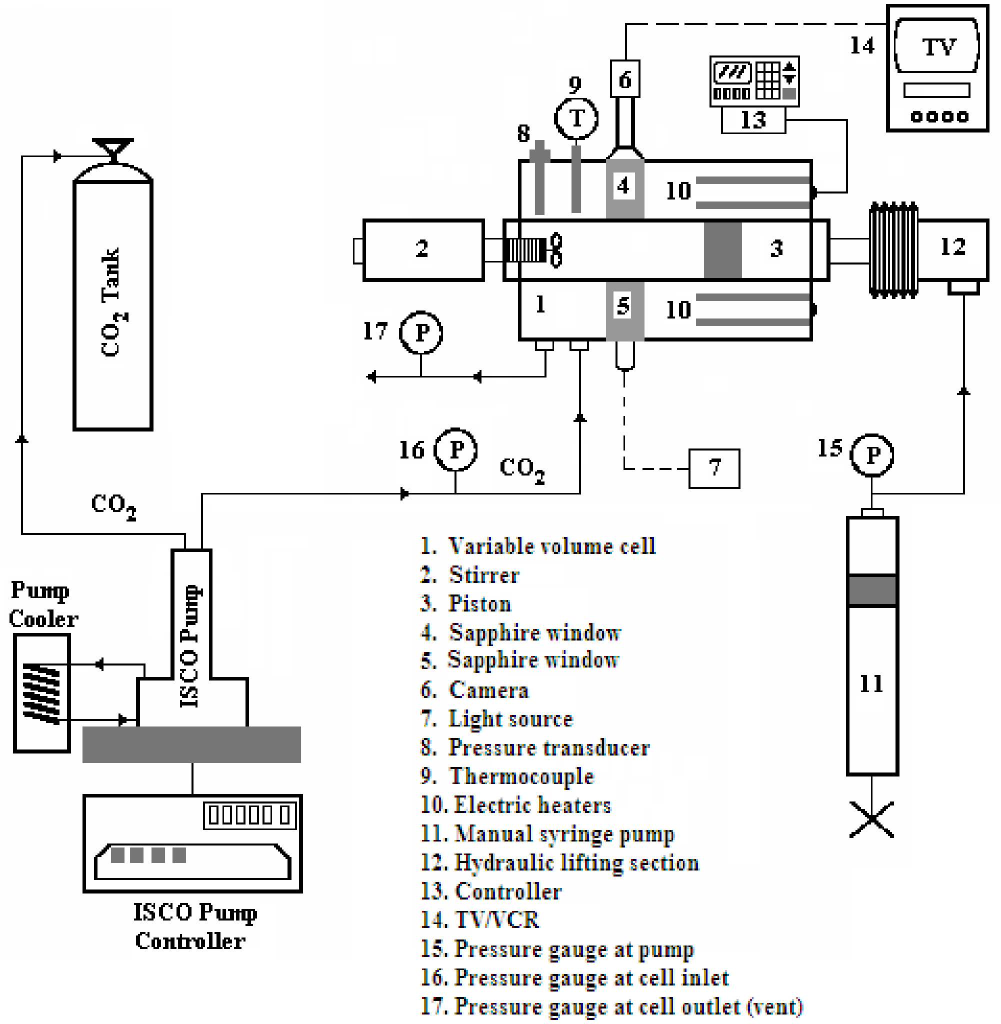

Figure 5.1. Cloud Point Experimental Set-Up Diagram.

This experimental procedure is described step by step in the flow diagram presented in Figure 5.2.

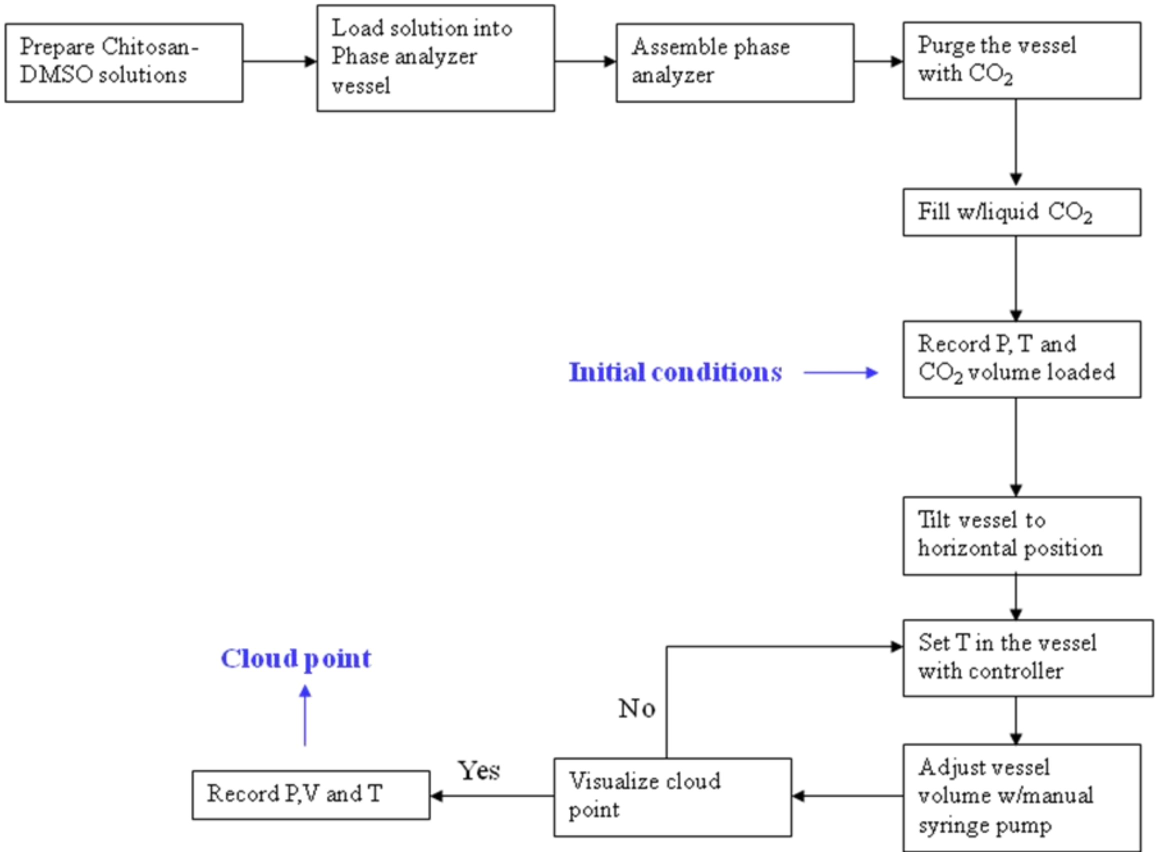

Figure 5.2. Flowchart for the Static Solubility Procedure.

Different solutions of Chitosan-DMSO (0.1, 0.5 and 1 mg/ml) were prepared by weighing 0.01g; 0.05g and 0.1g of Chitosan respectively using an analytical balance, measurable to ± 0.0001 g, and mixing this powder with 100ml of DMSO measured with a pipette, measurable to ± 0.001 ml.

After the solution was prepared, the liquid Chitosan-DMSO mixture was loaded into the cell using a pipette. Then the mixer assembly was screwed, closing the vessel. At this stage, the volume of the vessel was adjusted to 5 ml and the remaining air was purged out slowly with carbon dioxide. When the purging was completed, the outlet valve was closed, and the vessel was filled with CO_2 at a constant flow rate of 1ml/min, using the automatic syringe pump, until the desired pressure was reached. When the desired pressure was obtained, the inlet valve of the vessel was closed. At this point pressure, temperature, and CO_2 volumes that had been fed into the vessel were recorded as initial operation conditions.

Next, the vessel assembly was tilted into a horizontal position where the interface between Chitosan-DMSO and $SCCO_2$ phases in the cell could be visualized in the monitor. Then the desired temperature of the vessel was adjusted with the controller, and a period of 2 h is given for the system stabilization. The stirrer was activated and once the pressure and the temperature in the vessel were constant, the contents of the vessel were compressed by reducing its volume by moving the piston with the mechanical syringe pump, until a cloudy phase was formed. Once in the one-phase region, the pressure was lowered rapidly by moving the piston backwards until two phases were visualized. The pressure was raised slowly until a cloudy phase was formed again. This procedure was repeated five times for each sample in order to obtain repeatability. Next, the temperature of the system was changed (308, 313, 318°K) and the entire procedure was repeated to obtain more solubility data with the same load. (The step by step procedure is presented in Appendix C).

5.1.2. Dynamic Solubility

Figure 5.3 shows a diagram of the system used in this research. The set-up was built with off-the-shelf equipment and is similar to ones used by several investigators including Johnston and Ecker 1981, and Krukonis and Kurnik 1985.

The basic structure of this system consisted of two pumps (one syringe pump (ISCO 500) for the supercritical fluid and a HPLC pump (Waters 600E) for the liquid cosolvent), a preheater coil, an inline mixer and the extraction cell where the solid solute was placed. The solute extracted with the supercritical mixture was accumulated in a collection vessel and analyzed with an UV (HP 1050), while the expanded supercritical flow was measured with a Digital Wet Test Meter (Model 63135 PAC).

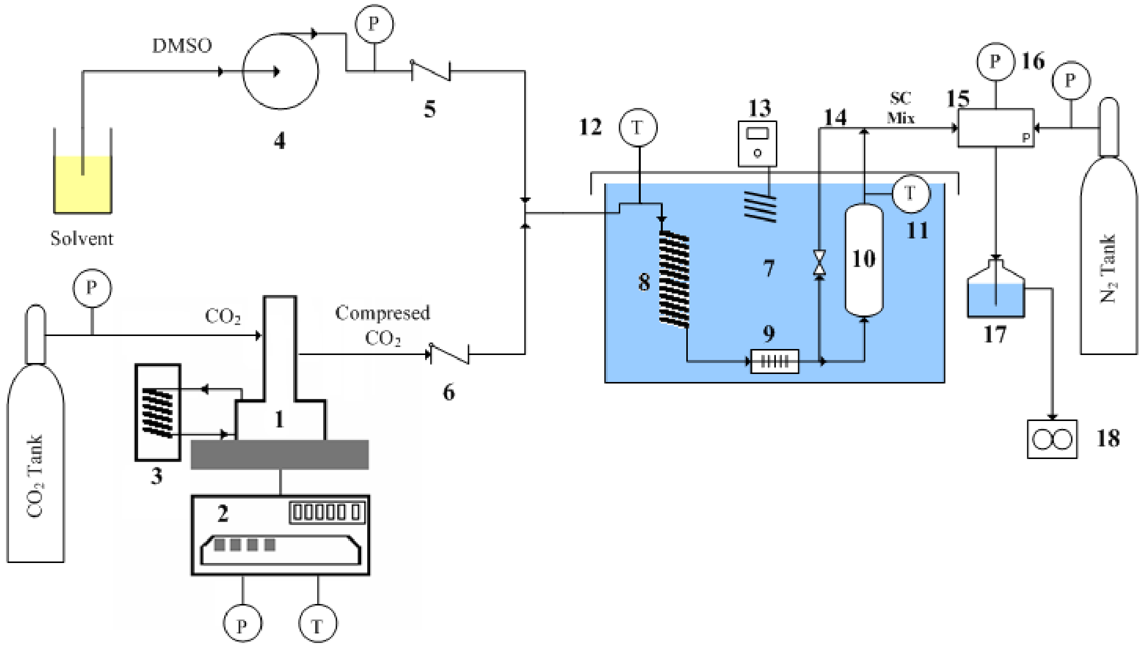

Figure 5.3. Dynamic Solubility Set-Up Diagram.
(1) ISCO pump, (2) ISCO pump controller, (3) pump chiller, (4) HPLC pump, (5, 6) check valves, (7) water tank, (8) coil heat exchanger, (9) inline mixer, (10) extraction vessel, (11, 12) thermocouples, (13) Immersion circulator, (14) bypass line, (15) back pressure regulator, (16) pressure gauge, (17) collection vessel, (18) wet test meter.

The experimental procedure to study the ternary system Chitosan-DMSO-$SCCO_2$ dynamic solubility has different steps and operation conditions that can be easily visualized in the flow chart presented in Figure 5.4. Liquid carbon dioxide (CO_2) was charged to the system using the syringe pump, which was kept at -3 °C with the help of a chiller, to ensure the CO_2 was at liquid phase while it was pumped into the system. This guaranteed a constant flow rate. The co-solvent used in this particular case was DMSO, which was pumped into the system by the HPLC pump.

After leaving the pumps, the CO_2 and the DMSO flowed through a 10 m stainless steel coil submerged into a water bath at constant temperature (the pre-heater stage). Then the DMSO-CO_2 flow passed through an inline mixer, ensuring a homogeneous mixture at the bath temperature before it contacted the heavy solute. The supercritical solution was then fed to the extraction vessel, where the heavy solid (Chitosan) was carefully packed to ensure proper contacting, to maintain the solute in the column even if it liquefied at operating conditions, and to allow sufficient room for the heavy liquid to expand as the supercritical fluid dissolved in it.

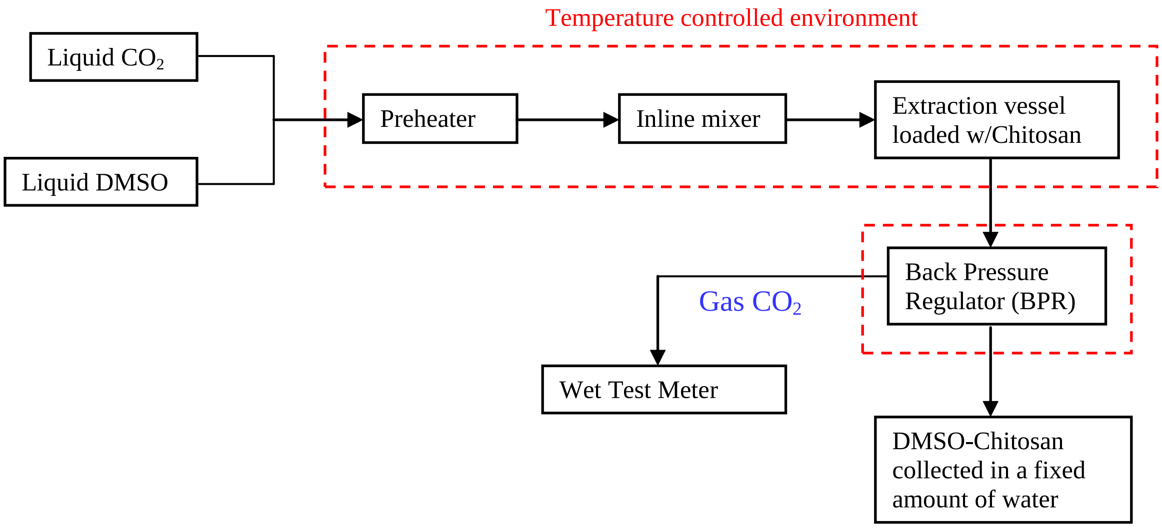

Figure 5.4. Flowchart for the Dynamic Solubility Procedure.

The column was packed with a stainless steel mesh, followed by a layer of glass wool at the bottom, then the solute was added, and finally another layer of glass wool at the top and the stainless steel mesh. For this research the glass wool and all the glassware used were pretreated with 5% hexamethyldisilazane (HMDS) solution and heated in the oven at 70°C for 12 h, creating a chemical bond with the silanol groups (Si-OH), which could capture the Chitosan producing wrong solubility data.

After the mixture left the extraction vessel, it was expanded through a mechanical back pressure regulator and collected over water into a glass collection vessel. To avoid clogging, the back pressure regulator was wrapped with a heating tape, keeping it at a temperature greater than the bath temperature, to compensate any Joule-Thomson cooling during the expansion of the CO_2. The Chitosan required for this research was soluble in water. Therefore, a measured amount of water was used to collect the extracted solute, and the concentration of Chitosan in the resulting solution was determined through UV analysis. The flow rate of the expanded CO_2 was measured with a Wet Test Meter connected to the glass collection vessel and DMSO amounts were determined from mass balance. The step by step procedure is presented in Appendix D.

5.2. Encapsulation Set-up

As is the case in the development of most new methods, the encapsulation set-up presented in Figure 5.5 was built with off-the-shelf equipment in order to minimize delivery time and maximize flexibility in design as well its retrofit.

The major pieces of equipment that were integrated within this system were a high pressure pump (P-200A THAR) used to feed the supercritical carbon dioxide, an HPLC pump for the Chitosan-DMSO mixture, a constant temperature air box where the encapsulation cell was placed, a heating bath connected to a heat exchanger placed inside the box to ensure constant temperature environment, three thermocouples (used to read the temperature inside the box and at the entrance and outlet of the cell), a lamp, a video camera/recorder system, heating tape elements over the encapsulation cell and the back pressure regulator, a back pressure regulator, a collection vessel and Wet Test Meter. The high pressure pump was connected to a chiller to ensure carbon dioxide will be at the liquid phase at the pump all the time, avoiding cavitation problems.

The insulation box was used to keep the stainless steel coil that carries the carbon dioxide and the coating solution (Chitosan-DMSO) injection system at the same temperature, ensuring supercritical conditions before reaching the encapsulation vessel.

The encapsulation vessel used was a modified Jerguson flat glass gauge, consisting of three parts. The solid central body or chamber was machined from a stainless steel bar, where one stainless steel sintered distributor plate with 0.5 μm holes was placed at the bottom of the cell and another stainless steel sintered frit plate with 0.2 μm holes was located at the top, acting as a filter to stop solid particles from leaving the vessel. The frit at the bottom has a 1/16” hole in the center for the coating solution injection tubing to pass through (Figure 5.5). The other two parts were the side bar covers that held one tempered glass each, and steel bolt ant nuts to keep all the three pieces together (Figure 5.6), even at high pressure and temperature (2220 psig, 600 °F).

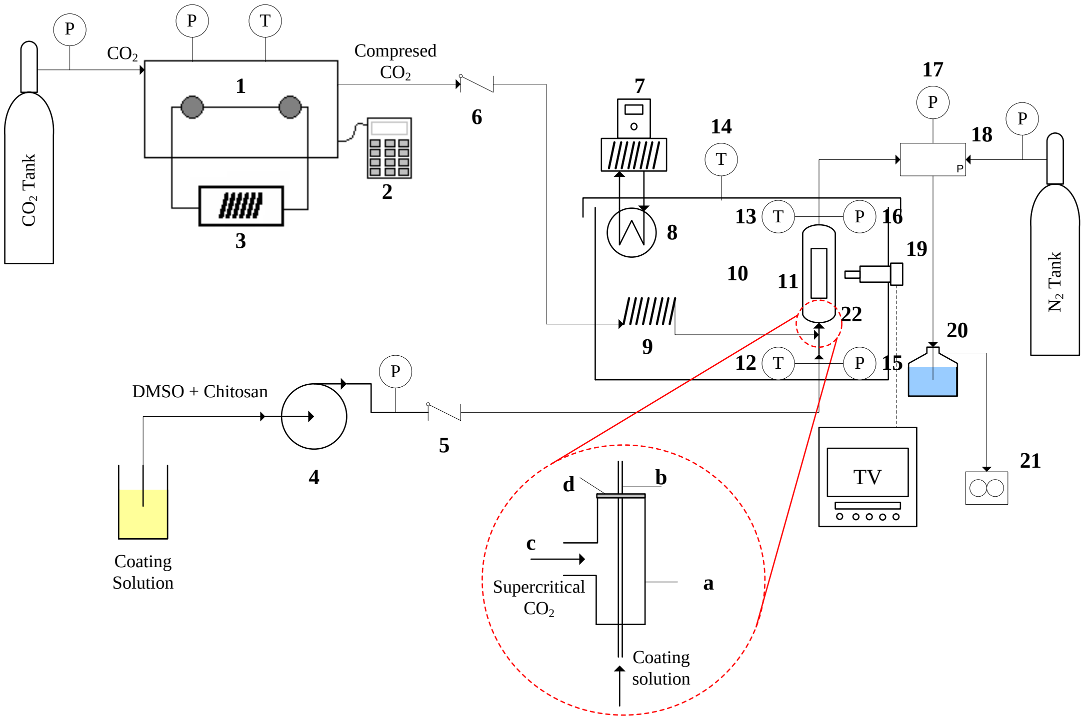

Figure 5.5. Encapsulation Set-Up Diagram.

(1) High pressure pump (P-200A THAR), (2) Pump controller, (3) Pump chiller (Refrigerator Recirculator, PolyScience), (4) HPLC pump (Waters 600E), (5, 6) Check valves, (7) Circulator bath (Haake B81), (8) Radiator, (9) Stainless steel coil, (10) Insulation box, (11) Windowed encapsulating vessel (Jerguson gauge), (12,13,14) K thermocouples, (15,16,17) Pressure gauges, (18) Back pressure regulator, (19) Camera, (20) Collection vessel, (21) Digital wet test meter (PAC), (22) Coating system detail: (a) ½ in SS Tee, (b) 1/16 in SS tubing, (c) ¼ in SS tubing, (d) SS distributor 0.5µm holes.

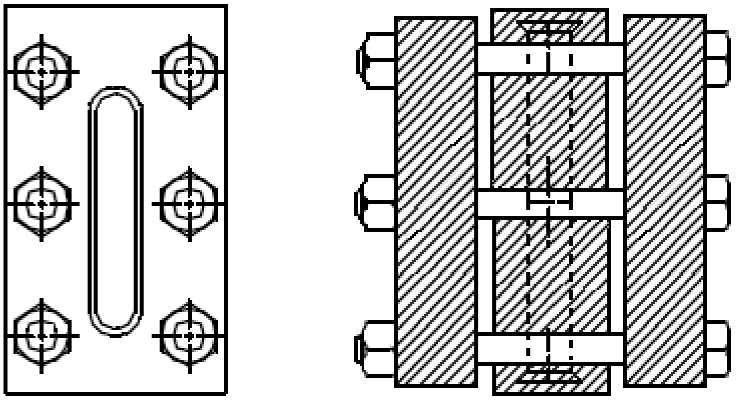

a) b)

Figure 5.6. Flat Glass Gauge. (Jerguson gauge)
(a) Front view includes window, (b) Side view.

To start the encapsulation procedure, the vessel was preloaded with the solid sample to be encapsulated and sealed following a specific procedure included in Appendix E. Then the heating bath was activated six hours before the start of the experiment, to guarantee a stable temperature inside and outside the cell. Carbon dioxide was charged to the system using a continuous pump, which was kept at 0 °C with the help of a chiller to be sure the CO_2 was at liquid phase while it was pumped into the system. The pump was operated in the continuous flow rate mode (Mode E), and the system pressure was controlled with a back pressure regulator. After leaving the pump, the CO_2 flowed through a coil located in a constant temperature air bath, where the CO_2 was pre-heated in order to reach supercritical conditions before reaching the encapsulating vessel.

In order to fluidize the particles, the supercritical CO_2 flow rate determination was required. After reviewing different equations like Wen & Yu 1966, Riba 1978 and Baeyens 1981, the first one was chosen following the recommendations of Carsten Vogt, 2005. There were two imperative numbers to estimate before starting the experiments: the minimum fluidization velocity required to fluidize the particles (u_{mf}) and terminal velocity (u_t).

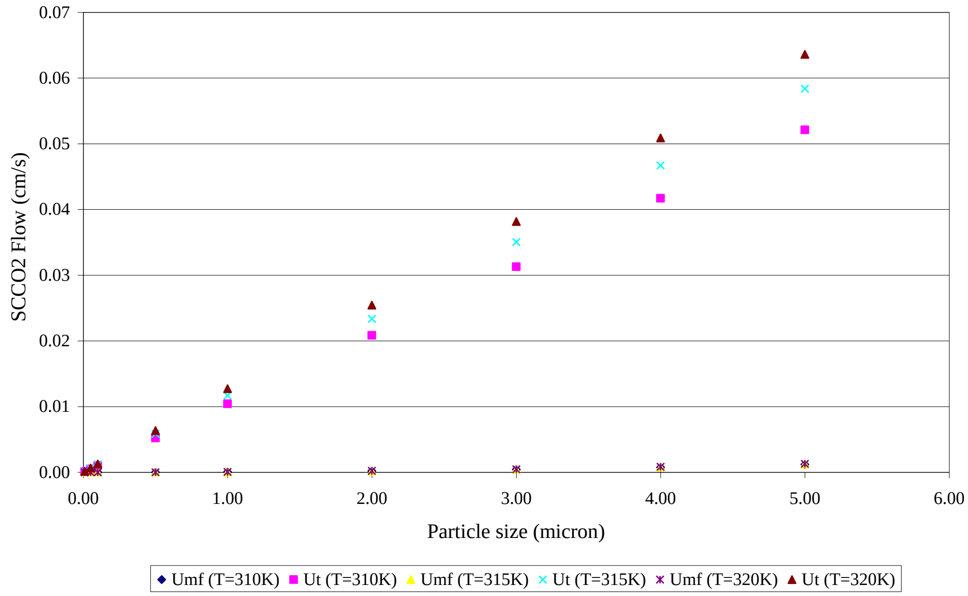

Figure 5.7. Carbon Dioxide Flow Required to Fluidize CaO Particles at 100 Bar.

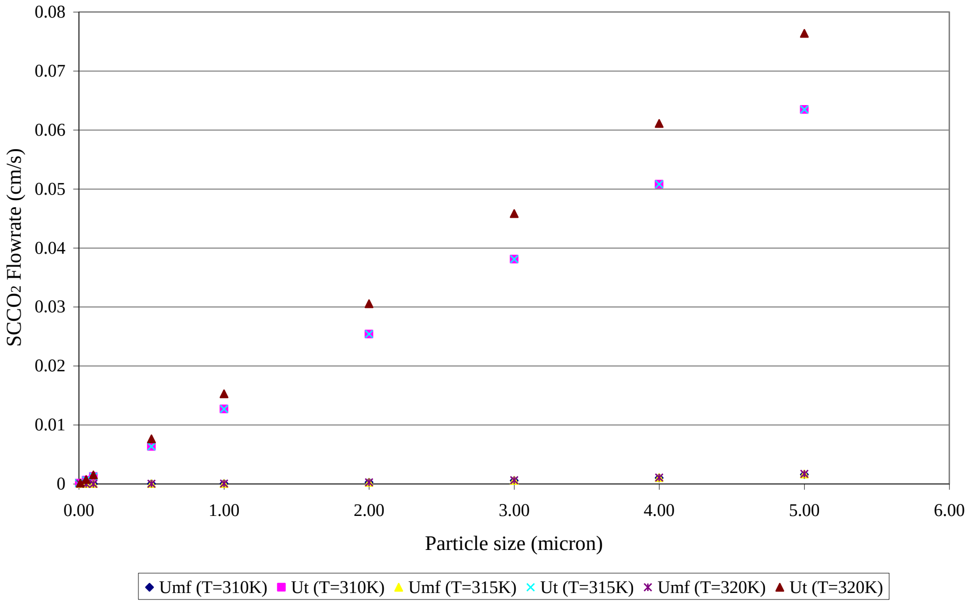

Figure 5.8. Carbon Dioxide Flow Required to Fluidize TiO_2 Particles at 100 Bar.

As can be seen in Figures 5.7 and 5.8, operating at constant pressure of 100 bar even a ΔT of 10°K did not cause major adjustments on the CO_2 flow rate required to fluidize the particles, compared to the effect of particle size. The CaO and TiO_2 samples used were made up of different particle sizes between 0.1μm to 7μm, which promoted a uniform fluidization. The best results were obtained for 2-5 g CO_2/min. Sample calculations and tabulated results are shown in Appendix F.

Once the system reaches the required operation conditions (T and P), and the particles are fluidizing properly, the coating solution, a DMSO-Chitosan mix, was pumped into the system by the HPLC pump, and the supercritical ternary system (Chitosan-DMSO-CO_2) stayed in contact with the solid particles for at least 30 minutes. The system was considered stable when the temperature difference registered at the inlet and outlet of the encapsulation cell was no more than 1 °C. The heating tape located over the cell was turned on and the temperature was controlled with an on/off controller. The coating material started to precipitate over the solid particles or core material, keeping the temperature constant to avoid re-dissolution of the polymer. The carbon dioxide flow was increased and the DMSO left the encapsulation vessel with the carbon dioxide.

After the DMSO-CO_2 mix left the coating vessel, it was expanded through a mechanical back pressure regulator and collected over a known amount of water into a glass collection vessel. To avoid clogging, the back pressure regulator was maintained at a temperature greater than the system temperature to compensate any Joule-Thomson cooling during the expansion of the CO_2. In order to establish when all the DMSO had been extracted to avoid the coating to be re-dissolved, a measured amount of water was used to collect the DMSO-$SCCO_2$ mix, and the DMSO concentration was determined through UV analysis using a quartz cuvette. The flow rate of the expanded CO_2 was measured with a Wet Test Meter connected to the glass collection vessel. The step by step procedure is presented in Appendix E.

5.3. Sample Analysis

Different characterization analysis methods were used to study the particles before and after encapsulation, as well as the encapsulant material itself.

5.3.1. Fourier Transform Spectroscopy (FTIR)

FTIR is an analysis technique that provides information about the chemical bonding or molecular structure of materials. This technique works on the fact that bonds and groups of bonds vibrate at characteristic frequencies. A molecule that is exposed to infrared rays absorbs infrared energy at frequencies that are characteristic to that molecule. During FTIR analysis, the sample is subjected to a modulated IR beam, and the sample's transmittance and reflectance of the infrared rays at different frequencies is translated into an IR absorption plot. The resulting FTIR spectra pattern is then analyzed and matched with known materials in the FTIR library of the computer processor.

FTIR spectroscopy does not require a vacuum, since neither oxygen nor nitrogen absorb infrared rays. FTIR can be used with very small quantities of sample, whether solid, liquid or gaseous.

For this research, all the samples analyzed were in the solid state: calcium oxide, titanium dioxide and Chitosan. The solid samples were milled with potassium bromide (KBr) to form a very fine powder. This powder was then compressed into a thin pellet which could be analyzed, as KBr is also transparent in the Perkin Elmer 4000 FTIR.

5.3.2. Ultraviolet Visible Absorption Spectroscopy (UV)

This analysis uses light in the ultraviolet and visible range. In this region of the electromagnetic spectrum, the molecules experience rotational and vibrational transitions, creating a complex and unique combination used to identify and differentiate chemical components.

UV spectroscopy is used for quantitative determinations. The Beer-Lambert law states that the absorbance of a solution is directly proportional to the concentration of the absorbing species in the solution and the path length. Therefore for a fixed path length, UV can be used to determine the concentration of the absorber in a solution by using a set of known concentration solutions to create a calibration curve that will show how the absorbance changes with the concentration.

The concentration of Chitosan was determined quantitatively by measuring the UV-Vis absorbance of the carbonyl and amino groups. This peak absorbance was analyzed using a V-530 UV-Vis spectrophotometer.

5.3.3. Scanning Electron Microscopy-Energy Dispersive Spectroscopy (SEM-EDS)

SEM is one of the most useful instruments in the study of solid materials. It is easy to operate, requires minimal sample preparation, is a non-destructive analysis system and enables rapid data acquisition. The SEM is used to generate high-resolution images and to show chemical composition of sampling areas from 1cm to 5 microns with magnification ranges from 20X to 30,000X. The equipment used for this research was the Hitachi 800.

The electron scanning microscope uses a focused beam of high energy electrons to generate a variety of signals at the surface of solid specimens. These signals include secondary electrons that produce SEM images, backscattered electrons, diffracted backscattered electrons used to determine crystal structures, photons that are used for elemental analysis (EDS), and visible light and heat.

Samples must be solid and they must fit into the microscope chamber. Samples must be stable in a vacuum on the order of 10^{-5} to 10^{-6} torr and dry; in this particular research all the samples were dry particles, coated and uncoated. Sample preparation was minimal. All the samples were dried under vacuum and kept in a desiccator and sprinkled over a carbon tape. In order to prevent charge buildup, the samples were coated with a thin layer of conductive material (gold), obtaining high resolution images.

Another application used extensively with the Hitachi 800 was the Automated Particle Analysis tool. This application is designed to characterize hundreds of particles by size, shape and chemical composition.

5.3.4. Transmission Electron Microscopy (TEM)

This is a microscopic technique whereby a beam of electrons is transmitted through a sample, interacting with it as it passes through. An image is formed as a result of this interaction between the electrons and the sample components; then the image is magnified and focused onto an imaging device (screen, photographic film or CCD camera).

A TEM was used in this research to visualize and measure the Chitosan coating over the CaO and TiO_2 particles, based on the structural difference (organic or inorganic) of the coated particles. The sample was prepared by placing a drop of the solution made with Ethanol and coated particles on a Formvar-coated Cu TEM grid that was dried under a lamp in ambient conditions. The grid was then placed within the TEM vacuum chamber (model FEI Morgagni 268D) and examined.

5.3.5. Atomic Force Microscopy (AFM)

This is a high resolution scanning microscopy technique that offers tridimensional particle visualization with proved resolution on the order of fractions of nanometers. The AFM consists of a cantilever with a sharp tip at the end that is used to scan the specimen surface.

This analysis technique was useful to obtain topographic imaging of the uncoated and coated particles, including surface roughness. The sample preparation for this analysis was simple and basic: double-sided sticky tape was used to attach the loose particles over a thin flat piece of glass.

There are two basic operation modes for the AFM: static and dynamic. The static mode was used in this research. In this approach, the cantilever was dragged across the surface of the sample and the contours of the surface, and uncoated and coated particles were measured directly using the deflection of the cantilever.

5.3.6. Differential Scanning Calorimeter with Thermal Gravimetric Analysis (DSC-TGA)

Thermal analyses are useful techniques to determine properties of materials as they change with temperature. To determine the inorganic-organic composition of the encapsulated particles, two methods were used in this research: differential scanning calorimetry and thermal gravimetric analysis with a TA SDT Q600 DSC-TGA system.

These two features were utilized for two different reasons. Differential scanning calorimeter measures the heat flow and the glass transition temperature of the polymer coating (Chitosan). Thermogravimetric analysis (TGA) measures the weight changes in material, determining the composition (organic coating-inorganic core) of the samples. Samples were heated in air at a rate of 5°C/min from room temperature to 700°C.

CHAPTER 6

EXPERIMENTAL RESULTS

The objective of this research had been to encapsulate small solid particles using a biopolymer, Chitosan, with supercritical CO_2 as a solvent and DMSO as a cosolvent. In order to accomplish this goal some initial steps had to be accomplished. First, a set of experiments was performed to determine the cloud point for the system DMSO-$CO_{2,}$ in order to validate the experimental set-up and the procedures with published data. The next step was determining the cloud point for the ternary system Chitosan-DMSO-CO_2 system. There is no such published polymer solubility data. In order to obtain data at the operation conditions for the encapsulation system, a dynamic solubility experimental system was developed and used to obtain solubility data. Finally, CaO and TiO_2 particles were encapsulated with Chitosan in a fluidized bed using a temperature swing to initiate dissolution. These experimental results and characterization will be presented in this chapter.

6.1. Density Experiments

Some of the models used to calculate thermodynamic properties of polymers-solvents solutions require that the concentration should be expressed in terms of volume fractions. For this reason, binary solution characterization information was required. To calculate volume fraction accurately, the partial molar volumes should be known, and as a consequence it was important to have accurate density data for different compositions of the binary mixture. In this particular case, DMSO-Chitosan, the solution was prepared by mass using an analytical balance with ± 0.0001g accuracy (OHAUS, Adventurer-Pro). The density measurements were made with a certified density meter with 0.0001g/cm^3 accuracy (DMA 4000, Anton Paar). Six different solutions were prepared by dissolving Chitosan powder in DMSO at room temperature. The concentrations expressed in weight percentage of Chitosan were: 0.15, 0.88, 1, 2.57, 4.73 and 17.36 w/w %. The density measurements were made in a temperature range of 298.15-358.15°K. The experimental data obtained was as follows.

Table 6.1. Density Data for the Mixture DMSO-Chitosan.
(Chitosan concentration w/w%)

T (°K)		**298.15**	**308.15**	**318.15**	**328.15**	**338.15**	**343.15**	**348.15**	**358.15**
Chitosan	**ρ (g/cm^3)**								
0%	**ρ**	1.0966	1.0852	1.0752	1.0652	1.0551	1.0501	1.0451	1.0350
	STD	-	-	-	-	-	-	-	-
0.15%	**ρ**	1.0967	1.0967	1.0967	1.0967	1.0967	1.0967	1.0967	1.0967
	STD	0.0003	0.0003	0.0003	0.0003	0.0003	0.0003	0.0003	0.0003
0.88%	**ρ**	1.0968	1.0876	1.0777	1.0677	1.0572	1.0522	1.0472	1.0372
	STD	0.0007	0.0006	0.0006	0.0006	0.0001	0.0001	0.0001	0.0001
1%	**ρ**	1.0974	1.0890	1.0792	1.0695	1.0594	1.0544	1.0493	1.0386
	STD	0.0016	0.0006	0.0008	0.0008	0.0005	0.0002	0.0001	0.0001
2.57%	**ρ**	1.1014	1.0940	1.0845	1.0741	1.0611	1.0591	1.0544	1.0450
	STD	0.0007	0.0007	0.0007	0.0007	0.0007	0.0007	0.0007	0.0007
4.73%	**ρ**	1.1095	1.1046	1.0897	1.0800	1.0702	1.0653	1.0604	1.0505
	STD	0.0072	0.0000	0.0000	0.0000	0.0000	0.0000	0.0000	0.0000
17.36%	**ρ**	1.1417	1.1335	1.1226	1.1129	1.1021	1.0971	1.0947	1.0826
	STD	0.0005	0.0000	0.0000	0.0000	0.0002	0.0001	0.0021	0.0009

In order to be able to appreciate the effect that temperature and concentration had over the density of the mixture, the data offered in Table 6.1 is plotted in Figure 6.1. It was seen that under isothermal conditions, the density of the mixture increased proportionally as Chitosan concentration rose, and for a fixed concentration the density of the mixture decreased as the temperature increased.

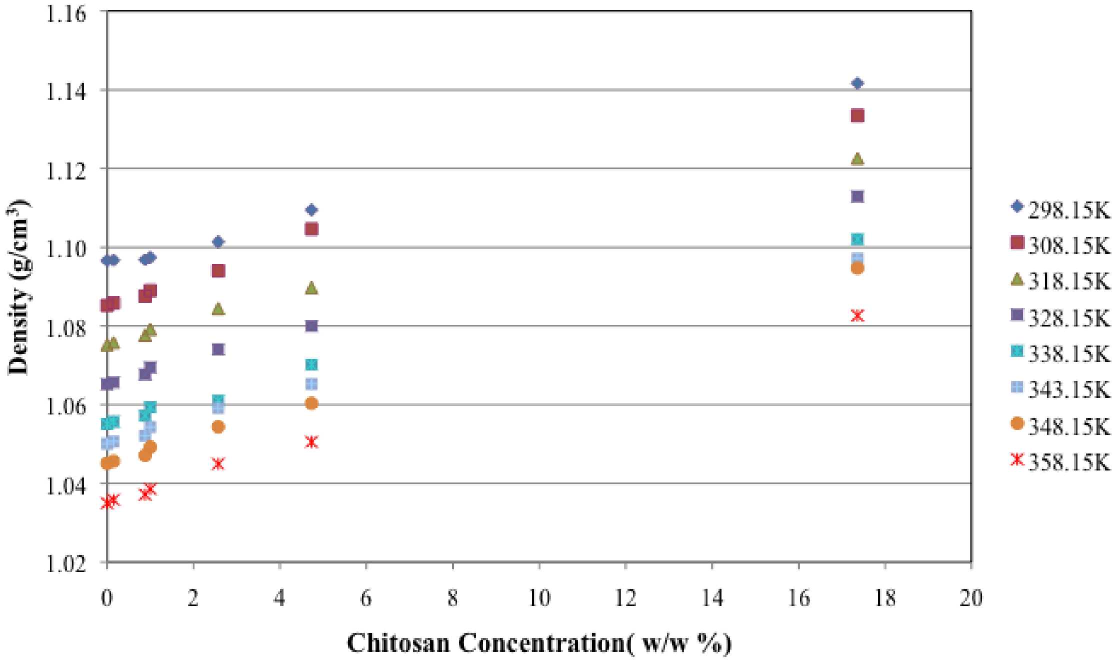

Figure 6.1. Density Isotherms as a Function of Chitosan Concentration for Different DMSO-Chitosan Solutions.

6.2. Cloud Point Experiments

The cloud point experiments were performed with the static set-up for the solvent system DMSO-$SCCO_2$ and then for the ternary system Chitosan-DMSO-$SCCO_2$.

6.2.1. DMSO-CO_2 System

Polymer solubility in CO_2 was very low, so a cosolvent was used. As has been found in this particular case, Chitosan is only soluble in water, so DMSO (dimethyl sulfoxide) was the only option, since water solubility in $SCCO_2$ is very low and other researchers like Rajasingam 2004, Gonzalez 2002 and Kordikowski 1995 studied the solubility of DMSO in supercritical dioxide for antisolvent process.

The experimental set-up used was presented in Chapter 5 section 5.1.1. One of the most important characteristics of this system was the ability to adjust pressure and temperature for a fixed concentration. This translated into data repeatability and multiple data points (P, T) for a given concentration. Pressure and temperature inside the vessel were tracked continuously in conjunction with phase behavior by having all the information projected live on the video monitor.

A stirrer was used to obtain a homogeneous mixture of DMSO-$SCCO_2$ inside the vessel. The phase behavior phenomena occurring inside the cell were visualized on a video monitor using a camera placed directly over a sapphire window.

The carbon dioxide used in this system was pumped with a syringe pump (ISCO 100DX) equipped with a cooling jacket to assure that the CO_2 withdrawn from cylinder tank remained in the liquid phase.

The first step of this experimental procedure was to load the liquid DMSO into the cell using a pipette (measurable to ± 0.01 ml), then the mixer assemble was screwed, closing the vessel. At this point, the volume of the vessel was adjusted to 5 ml and the remaining air was purged slowly with carbon dioxide. When the purging was completed, the outlet valve was closed, and the vessel filled with CO_2, at a 1ml/min constant flow rate, using the syringe pump until the desired pressure was reached. At this point, the inlet valve of the vessel was closed. The temperature in the cell was adjusted and the stirrer was activated. When the pressure and the temperature in the vessel were constant, the contents of the vessel were compressed by moving the piston with the mechanical syringe pump. Once a turbid or cloud-phase was observed, the temperature and pressure values were recorded, then the pressure was lowered by moving the piston backwards until the turbidity disappeared, and then raised slowly until the turbidity appeared. This procedure was repeated five times for each sample in order to obtain repeatability. Next, the temperature of the system was changed and the entire procedure was repeated to obtain more solubility data with the same load. The experimental data obtained is presented in the next figure with the existing published data.

The temperature selected for these experiments (314.2, 318.2 and 328.2°K) was based on the published data and the requirements for the encapsulation of natural or pharmaceutical products (thermal liable compounds). The results obtained were used to validate the method and at the same time to obtain temperature operation ranges for the coming experiments.

The DMSO molar fraction selected for this set of experiments was based on the envisioned coating method, where a small quantity of cosolvent was used, in order to avoid high concentration of DMSO on the encapsulated particle that could cause the coating to re-dissolve.

As can be seen in Table 6.2, experimental cloud point for the system DMSO-CO_2 was collected in a temperature range of 314.2°K to 328.2°K and pressures from 89 to 133.5 bars. The standard deviation based on the five readings made for each data point is less than one bar, indicating the experimental method is accurate.

Table 6.2. Experimental Cloud Point Data DMSO-CO_2

T (°K) **± 1 °K**	**X_{CO2}**	**P_{ave} (bar)**	**STD(bar)**
314.2	0.90	89.0	0.51
	0.91	90.3	0.50
	0.95	91.0	0.34
	0.96	91.2	0.52
	0.97	92.2	0.57
	0.98	92.1	0.48
318.2	0.90	103.0	0.62
	0.91	104.3	0.60
	0.94	105.0	0.75
	0.95	105.8	0.46
	0.97	106.2	0.59
328.2	0.90	129.0	0.60
	0.94	132.9	0.37
	0.95	133.5	0.45

The isotherms presented in Figure 6.2 are consistent with those reported by Rajasingam 2004, Gonzalez 2002 and Kordikowski 1995.

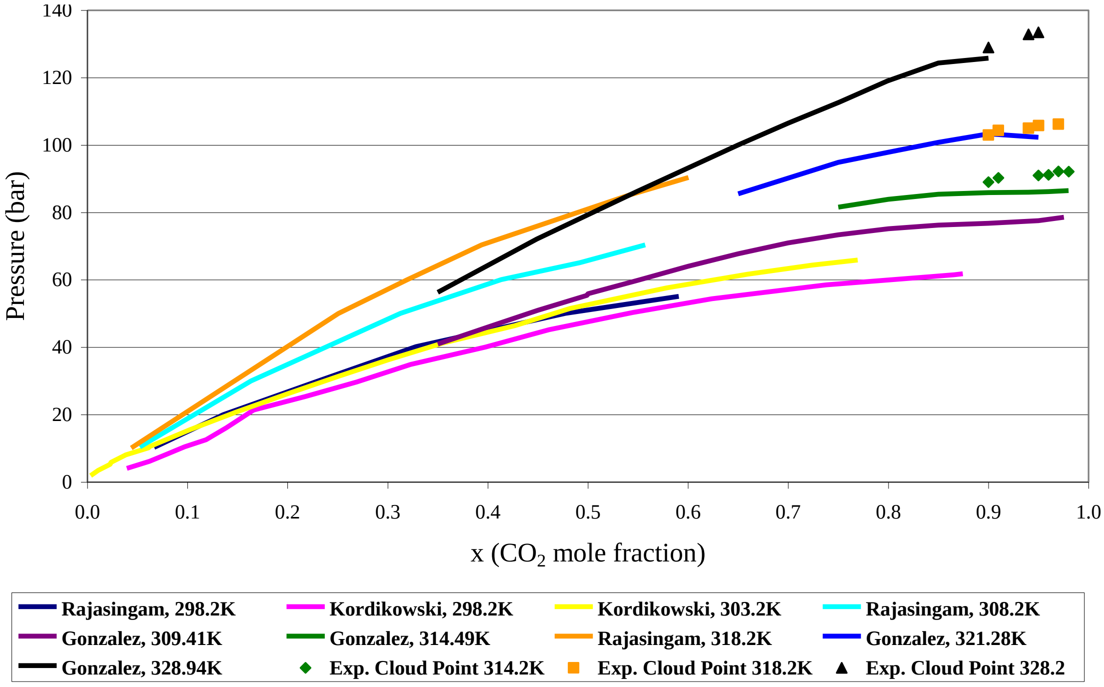

Figure 6.2. Cloud Point Experimental Data for the System DMSO- CO_2

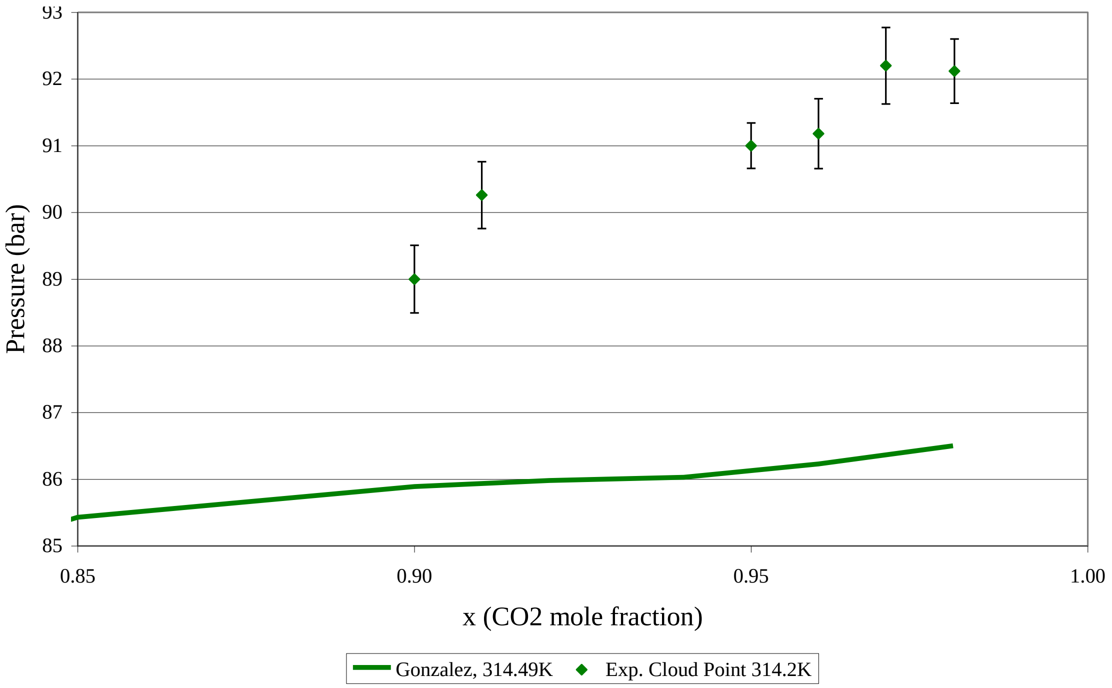

Figure 6.3. Detail Cloud Point Experimental Data for the System DMSO-CO_2 at 314°K. Shows Standard Deviation Presented in Table 6.1.

Figure 6.3 is used to show the error bars on a small section of the cloud point plot presented in Figure 6.2. Since the standard deviation is low and varies between 0.34 to 0.75 bars, it is not possible to see it on the original scale. The variation observed in Figure 6.2 can be attributed to the different experimental methods. Rajasingam and Kordikowski used a sampling method where pressure drops of 1 bar were reported as well as 10% uncertainty of their measurements. Gonzalez used a set-up similar to the one presented in this research, but the DMSO volume required was higher since this information would be applied for anti-solvent processes, and this value was measured by the number of rotations of the handle on a manual pump.

6.2.2. Chitosan-DMSO-CO_2 System

Some biopolymers frequently used in pharmaceutical applications such as poly-(D-lactide) (PDLA), poly-(L-lactide) (PLLA), poly-(DL-lactide-co-glycolide) (PGLA), Dextran, Inulin and poly vinyl alcohol (PVA), are insoluble in $SCCO_2$, for this reason different authors have been studying and processing them on a ternary system, polymer-DMSO- $SCCO_2$ (Reverchon 2000, Perez de Diego 2004). However, no data on the system Chitosan-DMSO- $SCCO_2$ has been published.

The next logical step was to obtain cloud point experimental data for this ternary system, since the binary data cosolvent-solvent (DMSO-CO_2) was already obtained.

For this purpose, the exact same set-up was used, Phase Monitor SPM20 (made by Thar Technologies), but in this case different solutions Chitosan-DMSO (0.1, 0.5 and 1 mg/ml) were prepared by measuring the amount of Chitosan using an analytical balance, measurable to ± 0.0001 g, and mixing this powder with the corresponding volume of DMSO measured with a pipette, measurable to ± 0.001 ml.

The temperature selected for these experiments (308.2, 313.2 and 318.2°F) was based on the requirements for the encapsulation of natural or pharmaceutical products (thermally labile compounds).

The DMSO molar fraction used was 10% or less in order to be consistent with the set of experiments performed for the system DMSO-CO_2.

In Table 6.3, the experimental cloud point data for the system Chitosan-DMSO-CO_2 was collected in a temperature range of 308.2 °K to 318.2 °K and pressures from 92.4 to 156.7 bars were presented, (solubility was expressed on mass basis in Table 6.3, and Figures 6.4, 6.5 and 6.6). The standard deviation value presented in this table was on average less than one bar. It was based on five readings made for each experimental condition, indicating that the experimental method is accurate. In total, for every temperature, 35 data points were collected, distributed on seven compositions and five readings for each pressure.

Table 6.3. Experimental Cloud Point Data Chitosan-DMSO-CO_2. (Mass fraction)

T (°K) ± 1 °K	w_{CO2}	w_{DMSO}	$w_{Chitosan}$	**P_{ave} (bar)**	**STD (bar)**
308.2	0.93	7.29E-02	6.65E-06	109.0	0.6
	0.92	7.84E-02	7.15E-06	92.4	0.5
	0.92	8.22E-02	7.50E-06	96.1	0.4
	0.86	1.42E-01	1.29E-05	100.8	0.4
	0.93	7.28E-02	3.32E-05	109.9	0.6
	0.94	6.45E-02	5.89E-05	119.8	0.7
	0.93	7.34E-02	6.70E-05	121.8	0.2
313.2	0.93	7.29E-02	6.65E-06	122.7	0.1
	0.92	7.84E-02	7.15E-06	95.3	0.8
	0.92	8.22E-02	7.50E-06	103.1	0.6
	0.86	1.42E-01	1.29E-05	113.9	0.6
	0.93	7.28E-02	3.32E-05	126.9	0.6
	0.94	6.45E-02	5.89E-05	138.0	0.5
	0.93	7.34E-02	6.70E-05	146.5	0.5
318.2	0.93	7.29E-02	6.65E-06	128.1	0.5
	0.92	7.84E-02	7.15E-06	103.7	0.7
	0.92	8.22E-02	7.50E-06	115.1	0.2
	0.86	1.42E-01	1.29E-05	121.8	1.1
	0.93	7.28E-02	3.32E-05	136.4	0.8
	0.90	9.50E-02	4.34E-05	145.5	0.3
	0.94	6.45E-02	5.89E-05	154.0	0.4
	0.93	7.34E-02	6.70E-05	156.7	0.3

As shown in Figure 6.4, Chitosan solubility increased proportionally with the pressure at constant temperature, and solubility decreased with temperature increments at constant pressure. This was a general effect that was suitable to the short-range attractive forces between solvent and solute. The solubility of a low-volatile solute like Chitosan, was enhanced as the density of the volatile solvent (CO_2) increased, as a consequence of temperature drop in an isobaric process or a pressure rise in an isothermal process.

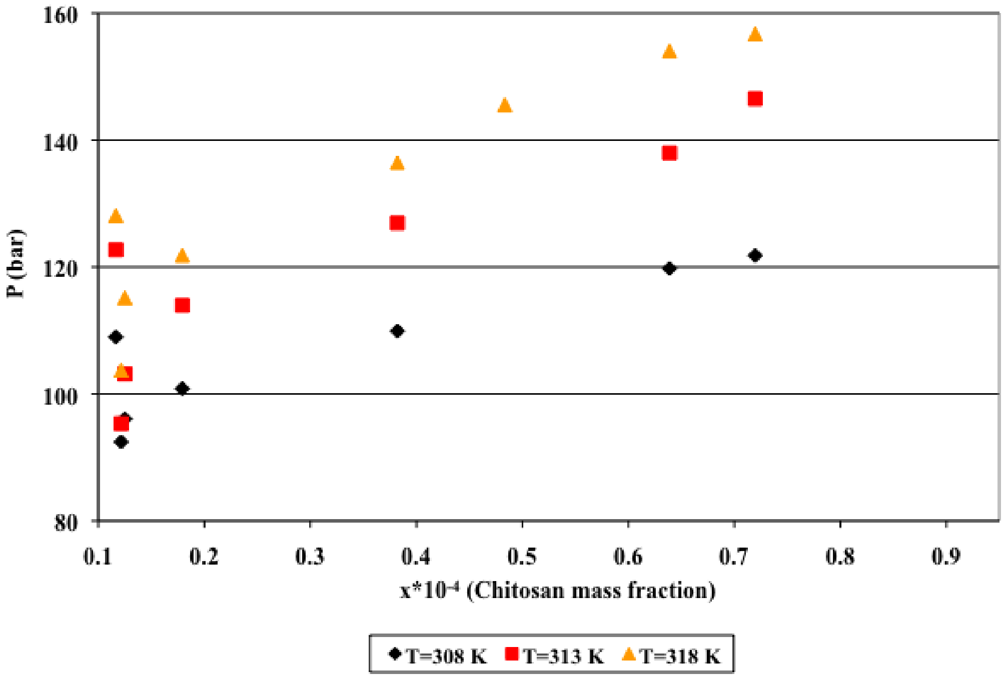

Figure 6.4. Cloud Point Experimental Data for Chitosan-DMSO- CO_2 (80-160 Bar).

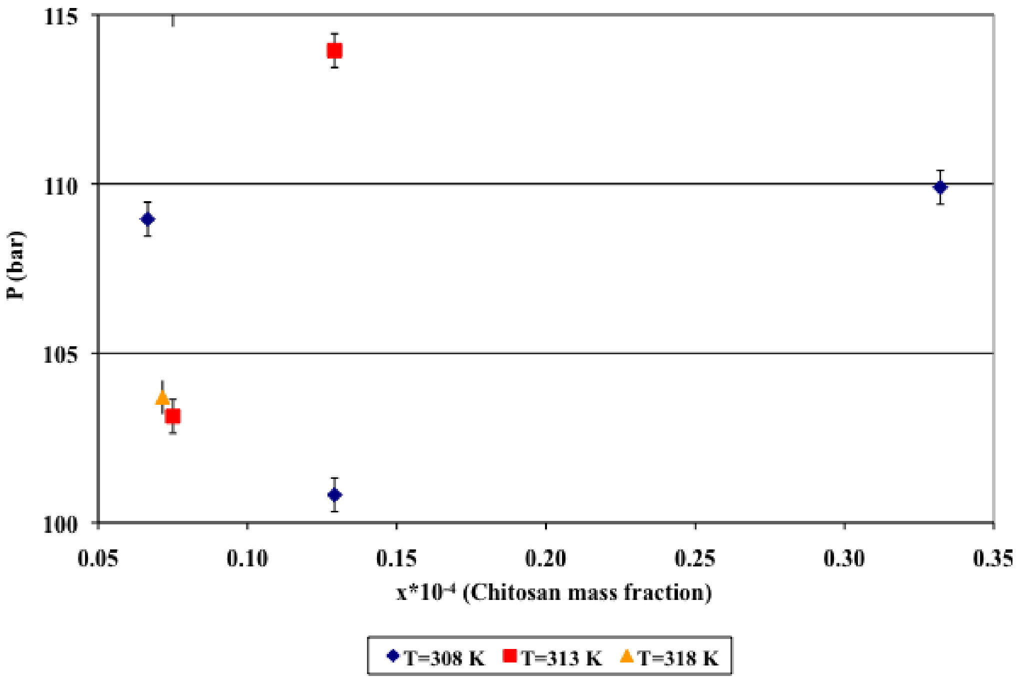

Figure 6.5. Cloud Point Experimental Data for Chitosan-DMSO- CO_2 (100-115 Bar).

In Figure 6.5, the error bars from a small section on the cloud point plot data in Figure 6.4 is presented, since the standard deviation was low and varied between 0.2 to 1.1 bars, it was not possible to show it on the original scale.

A drastic change of slope was observed when collecting the cloud point data and this is presented in Figure 6.6. This particular change of the solubility values could be attributed to the fact that as this was a low solubility system. The critical point of the solvent was close to the lower critical endpoint of the mixture. This means that the behavior of the fluid phase in the proximity of the critical endpoint was strongly influenced by the proximity of the critical point of the solvent.

At the critical endpoint, the solubility did change with infinite slope in the isobar as a function of temperature, or in the isotherm as a function of pressure, and this infinite slope was caused by the high vulnerability of the solution at the critical endpoint.

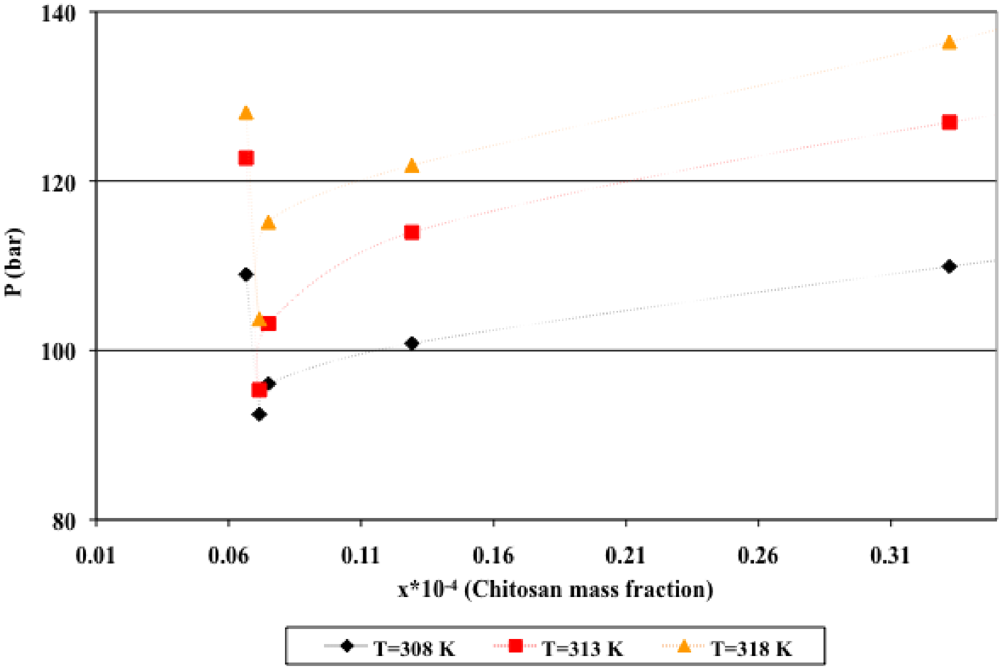

Figure 6.6. Slope Change at the Proximity of the CO_2 Critical Point for the System Chitosan-DMSO-CO_2.

In general, this cloud point experimental data confirms the hypothesis that the solubility of this polymer (Chitosan) is low, compared to the solubility of the cosolvent (DMSO). This suggests that an antisolvent or a perturbation coating method should be used when a solution of DMSO-Chitosan will be used as the coating mix and the CO_2 will be used to extract the DMSO. The Chitosan will be precipitated over the particles to be encapsulated either by saturating and expanding the DMSO with CO_2 or by temperature perturbation.

6.3. Solubility Experiments

With the cloud point information available for the binary and ternary system, next a dynamic solubility data for the system Chitosan-DMSO-CO_2 was required in order to establish the operation conditions for the encapsulation process.

The dynamic solubility system was useful to reproduce the solubility data obtained in the static set-up, this time having a continuous process under supercritical conditions. This experiment was considered as the first stage for the encapsulation process, since it was possible to establish proper sampling procedures, ascertain experimental difficulties and determine settings like temperature, pressure and flow rates.

In order to get the solubility information for the ternary system, the concentration of each component needs to be determined or calculated. The UV system was used to establish the Chitosan concentration in water-DMSO solutions, and the first step was to ensure that the DMSO presence in the water solution would not interfere with the Chitosan determination.

After the UV calibration procedure, which is presented in full detail in Appendix G, it was established that disposable PMMA cuvettes could be used to determine Chitosan concentration in Water –DMSO solutions at a wavelength of 294 nm.

The UV spectra in Figure 6.7 shows the absorbance of the Chitosan collected in 200 ml of DI water when the supercritical solution Chitosan-DMSO-CO_2 leaving the extraction cell was bubbled into an Erlenmeyer flask containing the water.

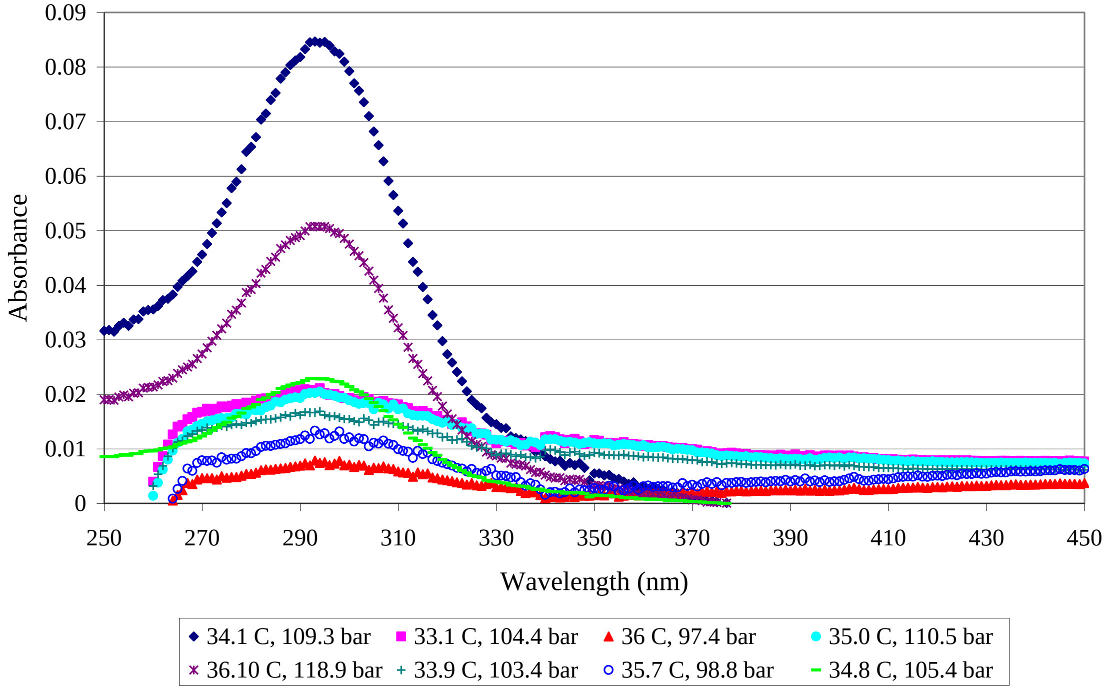

Figure 6.7. UV Spectra for Chitosan-DMSO-Water Solutions.

Using the linear relation presented in Appendix G and the UV results at absorption band of 294 nm from Figure 6.7, the Chitosan concentration was determined as presented in Table 6.4.

Table 6.4. Chitosan Molar Concentration in 200 ml of Sample Solution.

Absorbance	**C (mg/ml)**	**Mol Chitosan**
0.0078	0.01	2.78E-07
0.0138	0.02	8.00E-07
0.0169	0.03	1.07E-06
0.0211	0.04	1.43E-06
0.0225	0.04	1.56E-06
0.0847	0.11	4.20E-06
0.0205	0.03	1.38E-06
0.0529	0.06	2.32E-06

The DMSO concentration was determined as a function of the operation time and the flow rate of the HPLC pump, which was calibrated before operating the system to ensure accurate values. The UV was not an option in this case, since Chitosan-DMSO peaks overlapped in the region 195-245 nm and they could not be de-convoluted.

Table 6.5. DMSO Molar Concentration in 200 ml of Sample Solution.

Operation Time (min)	**Flow (ml/min)**	**Mol DMSO**
278.00	0.16	0.63
295.00	0.17	0.71
299.15	0.17	0.72
288.18	0.17	0.69
315.00	0.17	0.75
360.28	0.17	0.86
235.00	0.17	0.56
365.00	0.17	0.87

The amount of carbon dioxide used to extract the Chitosan was determined in two different ways: using the Improved Rackett Equation (IRE) to determine the number of moles of liquid CO_2 at -3.0 °C pumped by the ISCO syringe pump through the extraction cell, and from the volume of expanded CO_2 registered by the Wet Test Meter (WTM) located at the end of the system (Appendix H). The results obtained were similar, since the error of the IRE at this low temperature was less than 0.2% compared to the IUPAC Tables (Smeltzer, 2006).

Table 6.6. Moles of CO_2 Used to Extract DMSO-Chitosan

T WTM (°C)	**Mol CO_2 (WTM)**	**T pump (°C)**	**Mol CO_2 (IRE)**	**% Diff**
24.50	5.93	-3.00	5.93	0.14
24.00	6.43	-3.00	6.29	2.27
24.20	6.26	-3.00	6.38	-1.82
25.00	6.19	-3.00	6.14	0.81
25.40	6.94	-3.00	6.72	3.20
24.40	7.70	-3.00	7.68	0.22
26.20	5.04	-3.00	5.01	0.57
25.20	7.74	-3.00	7.78	-0.47

To conclude, the information was put together and translated as solubility data, including Chitosan, DMSO and CO_2 fractions in Table 6.7. Usually, this information is required for modeling or simply as guidance when studying the solubility of a multiple component system for extraction or encapsulation purposes. However, in this particular case, the information was not available and is a contribution of this research. It is important to mention that every operation condition was evaluated twice and T and P were registered at three different points of the system. The accuracy of these readings is confirmed with the STD values presented in Table 6.7.

Table 6.7. Solubility Data for the System Chitosan-DMSO-CO_2

T (°C)	**STD (°C)**	**P (bar)**	**STD (bar)**	$X_{Chitosan}$	X_{CO2}	X_{DMSO}
36.0	0.50	97.3	0.7	4.25E-08	0.9045	0.0955
35.7	0.15	98.8	0.5	1.14E-07	0.8990	0.1010
33.9	0.20	103.4	0.4	1.50E-07	0.8991	0.1009
33.1	0.34	104.4	0.4	2.09E-07	0.8990	0.1010
34.8	0.23	105.4	0.7	2.08E-07	0.8991	0.1009
34.1	0.17	109.3	0.8	2.72E-07	0.8990	0.1010
35.0	0.21	110.5	0.2	2.47E-07	0.8990	0.1010
36.1	0.11	118.9	0.5	4.88E-07	0.8985	0.1015

Once all the dynamic solubility data was obtained, the next step was to compare these results with the cloud point experimental data for the ternary system. This information is presented as a plot in Figure 6.4.

It is important to note that the cloud point data obtained from the static set-up or solubility cell corresponded to the unique points where the components of the chemical system co-existed in equilibrium, the mixture became opaque and it was no longer possible to see the stirrer or the polished internal surface of the high pressure cell. The dynamic set-up provided solubility data through leaching of the solid at a rate where the extract phase was saturated. These results are interrelated and they should be similar, but not necessarily exact matches, since the measurement methods were different, even though (as confirmed in Figure 6.8) for a temperature of 35 °C both results presented the same behavior: as the pressure increased for an isothermal system, the solubility increased.

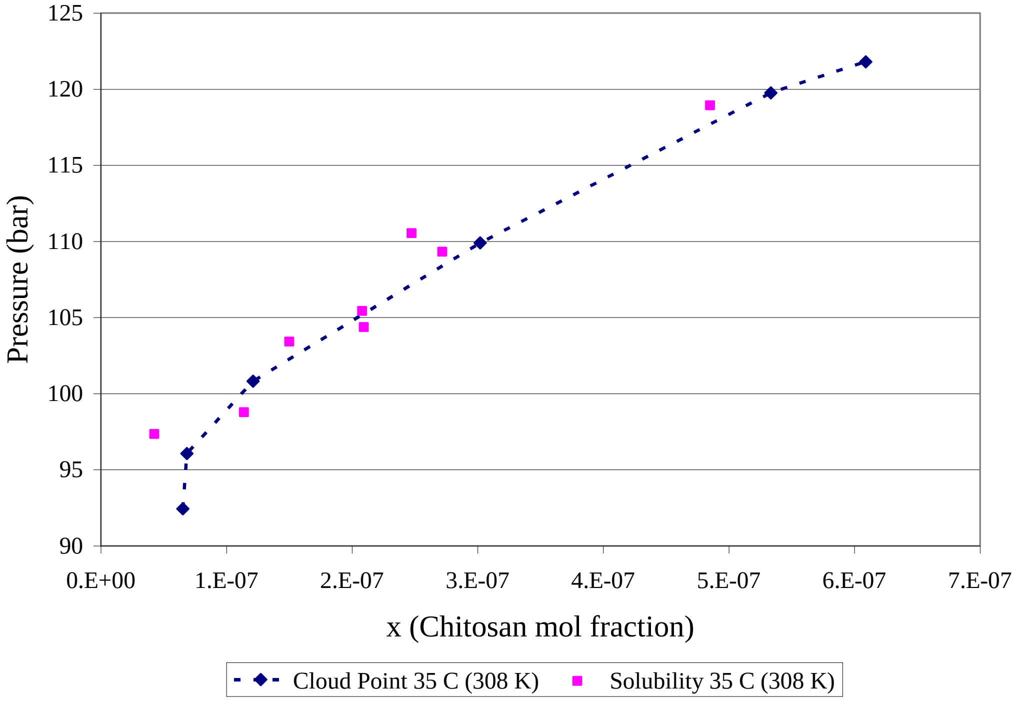

Figure 6.8. Solubility and Cloud Point Data for the Ternary System Chitosan-DMSO-CO_2 at 35 °C (308 °K).

6.4. Encapsulation Experiments

The static and dynamic solubility data obtained for the ternary system, helped establish that the pressure and temperature operation conditions for the encapsulation process were 92-156 bar and 308-318°K respectively.

The encapsulation set-up was built with off-the-shelf equipment, which makes it affordable and in this particular case we were able to build a system with a visualization window. This window made it possible to follow the encapsulation process, since the fluidization model for this ternary system was not available. In this particular experiment, the limitations were temperatures on the encapsulation cell no higher than 50 °C (323 °K) (to avoid the polymerization of the Chitosan in the lines) and pressures no higher than 130 bar (to avoid leaks on the encapsulation cell).

The materials to be encapsulated were titanium dioxide (TiO_2) and calcium oxide (CaO), and they are insoluble in DMSO. Figure 6.9 shows a diagram of the operation conditions during the encapsulation process.

Several encapsulation experiments were performed in the pressure range of 110-120 bars and a temperature range of 41-50°C (314-323 °K), using different contact periods and particles (CaO and TiO_2). Figure 6.9 describes graphically the encapsulation process step by step, considering each factor separately: pressure, temperature and carbon dioxide flow rate as a function of time. As shown in these diagrams, when the particles were getting covered by the encapsulants, all the conditions were kept constant in order to achieve a better coverage, followed by a temperature increase, which caused further Chitosan precipitation. For the given pressure range, temperature increase reduced Chitosan solubility and subsequently period allowed removal of DMSO in the system.

In an effort to show the effect of each of the operation conditions by itself, three plots are presented: Figure 6.10 (coating thickness as a function of pressure), Figure 6.11 (coating thickness as a function of temperature) and Figure 6.12 (coating thickness as a function of process time). At first glance these plots might cause some confusion, because of the complexity of the behavior shown. However, going back to the definition of solubility under supercritical conditions, it is obvious that these plots confirm the fact that solubility is a function of density and for this reason pressure and temperature effect cannot be analyzed independently.

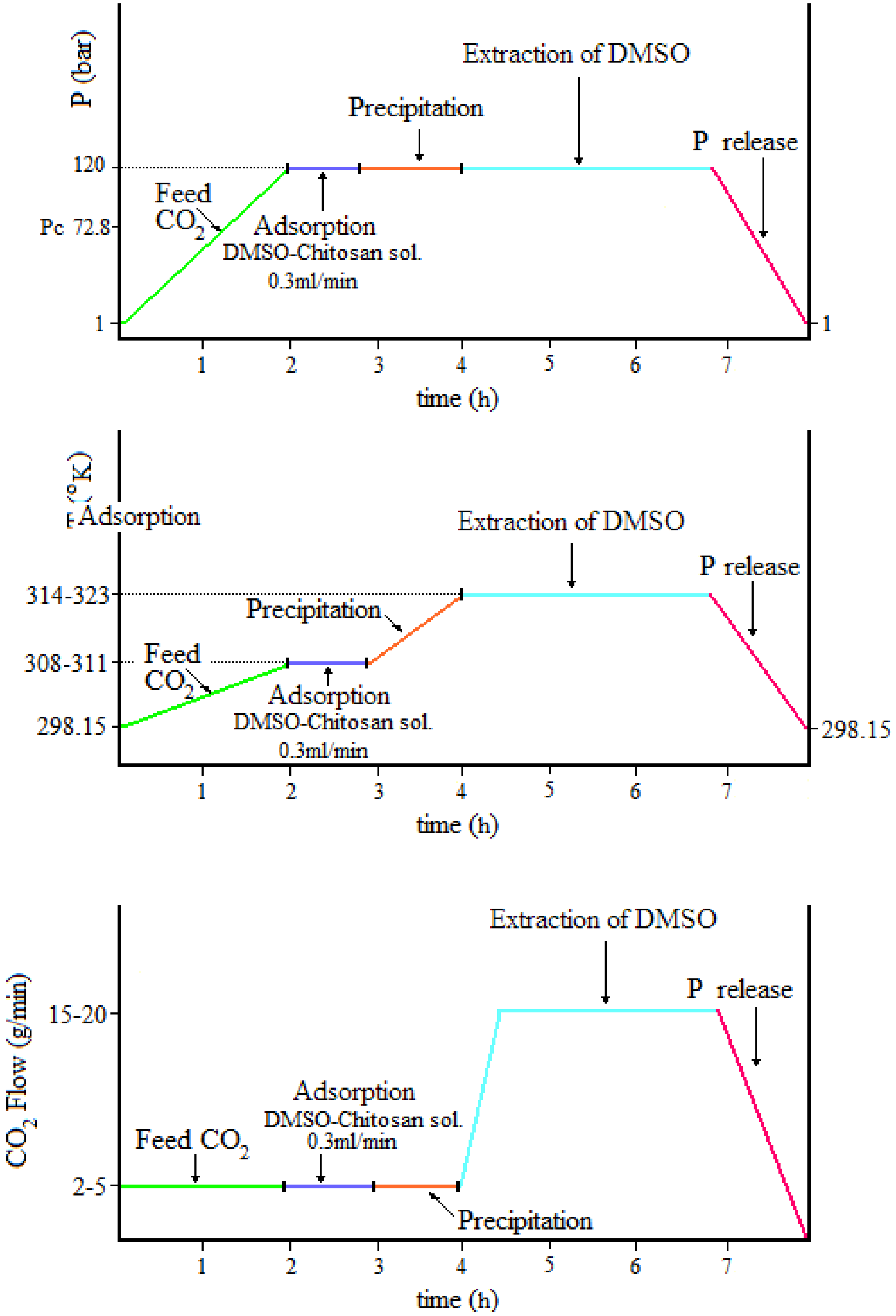

Figure 6.9. Coating Process Diagram.

The thickness of the encapsulant material deposited over the particles was given by a combination of factors: feed composition (DMSO-Chitosan), chemical composition of the mixture (Chitosan-DMSO-CO_2) in the cell, pressure, temperature and processing time. This means that even having the same feed composition, the thickness of the polymer deposited over the core material changed depending on the operation conditions (Appendix I).

Results presented in Figure 6.10 show that when pressure was raised at constant temperature, the coating thickness increased and coverage improved, which was a logical consequence of solubility enhancement.

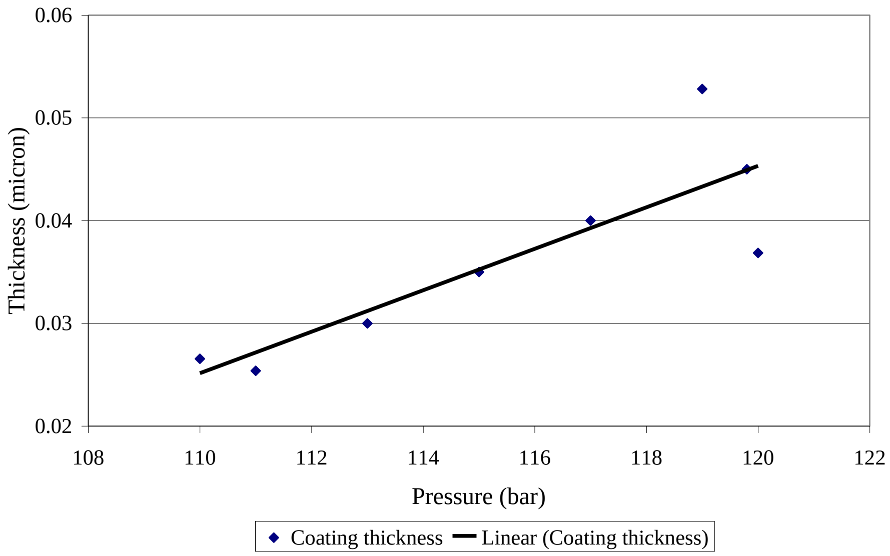

Figure 6.10. Coating Thickness as a Function of Cell Pressure

As the temperature increased at constant pressure the solubility of the polymer decreased, causing its rapid precipitation which was desirable, since this encapsulation method was based on temperature perturbation (Figure 6.11). However, if not controlled, the polymer precipitated too fast, producing agglomeration and a poor encapsulation process.

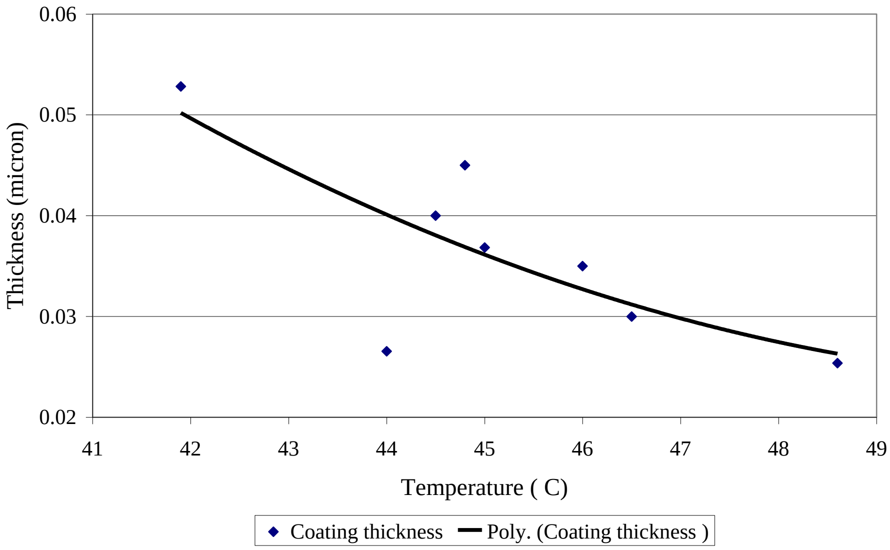

Figure 6.11. Coating Thickness as a Function of Cell Temperature.

Comparing Figures 6.10 and 6.11, it can be observed that the highest thickness was obtained for the combination high pressure-low temperature (120bar, 42ºC), which was the condition that enhanced solubility and consequently promoted better encapsulation.

The other factor considered in this encapsulation process was the process time, including precipitation and extraction of DMSO, as presented in Figure 6.12.

We would expect to get higher thickness for longer contact time, but as explained previously, solubility is a function of density, and as shown in detail in Figure 6.12, the lower thickness corresponds to a point with highest contact time at 120 bar and 42ºC, which could be an indication that the coating material was re-dissolved in the DMSO-CO_2 mixture and removed.

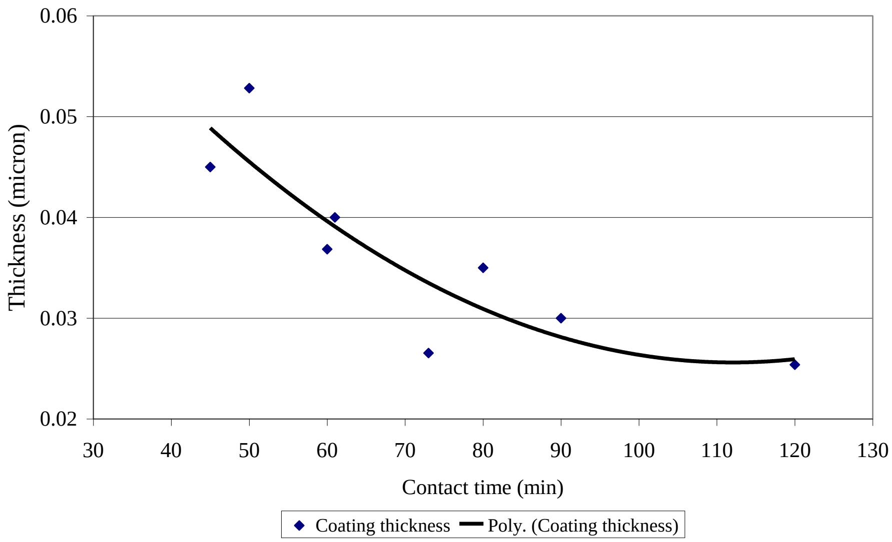

Figure 6.12. Coating Thickness as a Function of Process Time.

Table 6.8 includes all experimental conditions that resulted in encapsulated particles. When the contact period was 20 min or less, there was no conclusive information to affirm that any encapsulation was performed.

After micro-encapsulation, each sample was characterized. To establish the presence of Chitosan on the processed sample, FTIR was used. The concentration of each element in the sample was determined with the EDS. SEM was used to obtain the particle size distribution, the coating thickness was measured with TEM and finally the coating morphology was evaluated with AFM.

Table 6.8. Coating Experiments Chitosan-DMSO-Core Material

Core Material	**P (bar)**	**T(C)**	**Contact Time (min)**	**Thickness* (μm)**
CaO	111.0	48.6	Low pressure (12h)	0.0254
CaO	119.0	41.9	50	0.0528
CaO	119.8	44.8	45	0.1420
TiO_2	110.0	44.0	73	0.0265
TiO_2	120.0	45.0	60	0.0368

*These are average values, for 8-24 samples per experiment.

Figure 6.13 depicts FTIR results of transmittances of CaO samples before and after the encapsulation process. The plot in black (above) represents the CaO before coating and the only peaks observed correspond to traces of elements present on the quicklime sample: 875.99 cm^{-1} (SiO_2), 1432.41 cm^{-1} (Sulfate), 3676.53cm^{-1} (OH probably Ca-OH), which is caused by moisture exposure of the sample.

Figure 6.13. FTIR CaO Before Coating (Above),
CaO-Chitosan After Processing (Below).

The plot in red (below) represents the CaO coated with Chitosan, where the absorbance peaks obtained were compared with some published data available (Rout 2001, Cardenas 2004). The NH_2 deformations are in the range 1559-1583 cm^{-1}, C=O bond 1646-1655 cm^{-1}, C-H 2920-2945 cm^{-1} and N-H 3366-3450 cm^{-1}, similar to the ones found in literature reviewed.

These results confirm the Chitosan was precipitated during the encapsulation process, but do not necessarily prove its presence as an encapsulant. The same analysis was performed on all the TiO_2 and CaO samples, to verify the presence of Chitosan before proceeding with further analysis.

The next set of analyses performed was Energy Dispersive Spectroscopy (EDS) to determine the weight percentage of each chemical elements present in the samples after the coating process, in order to compare these values with the weight percentages of the same elements in the feed. In Tables 6.9 and 6.10 Calcium (Ca) was used for calcium oxide (CaO), Nitrogen (N) was used for Chitosan ($(C_{12}H_{24}N_2O_9)n$), sulfur (S) was used for DMSO (C_2H_6OS), titanium (Ti) was used for titanium dioxide (TiO_2), and oxygen (O) was used as a reference element to validate the accuracy of the EDS analysis. The difference (percentage basis) between the two values are presented in the last column on both tables.

Table 6.9. Feed Mass Balance vs SEM-EDS Analysis for Processed CaO Samples

Material	**Feed Mass Balance (Weight %)**			**SEM-EDS (Weight %)**				**Dif. (Oxygen)**
	Ca	**N**	**O**	**Ca**	**N**	**O**	**S**	**%**
CaO, Chitosan, DMSO*	70.72	0.09	28.68	61.03	3.46	27.78	0.60	3.14
CaO, Chitosan, DMSO	67.39	0.49	29.21	60.10	3.50	28.95	0.64	0.89
CaO, Chitosan, DMSO	42.64	3.51	33.13	31.82	2.24	34.82	0.27	-1.74
CaO, Chitosan, DMSO	48.26	2.83	32.24	40.80	3.96	33.40	0.72	-0.82
CaO, Chitosan, DMSO	35.72	4.36	34.23	28.83	4.01	31.90	1.31	1.05

* This experiment did not produce encapsulated particles

Table 6.10. Feed Mass Balance vs SEM-EDS Analysis for Processed TiO_2 Samples

Material	**Feed Mass Balance (Weight %)**			**SEM-EDS (Weight %)**				**Dif. (Oxygen)**
	Ti	**N**	**%**	**Ti**	**N**	**O**	**S**	**%**
TiO_2, Chitosan, DMSO	41.34	2.71	39.00	37.5	4.03	38.93	0.39	0.19
TiO_2, Chitosan, DMSO	29.24	4.47	38.68	20.28	7.86	38.98	0.31	-0.78

Visually it was easy to determine the presence of Chitosan in the processed samples just by observing the yellowish color of the dry powder, and SEM-EDS results confirmed the presence of Chitosan and DMSO in the processed samples (the last one (DMSO) in very small amounts), verifying that it was extracted with the supercritical CO_2 from the encapsulation cell. Another result obtained by using the SEM-EDS analysis is that even when the samples presented a yellowish color and no encapsulation was produced, having a higher percentage of N for the processed samples compared to the feed calculations was an indication of a high concentration of Chitosan. This particular sample was analyzed with TEM (Figure 6.14).

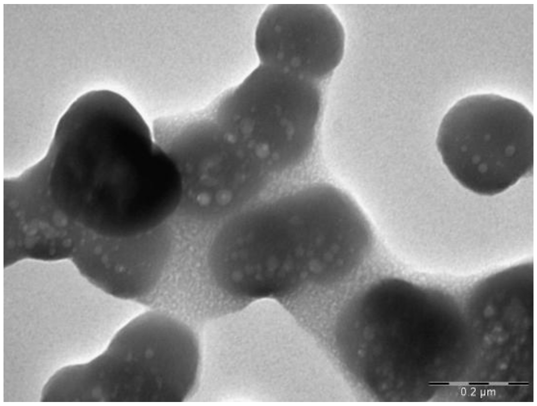

Figure 6.14. CaO-Chitosan TEM Image.

However, again these results were not conclusive, since the Chitosan could be present as coating or simply as precipitated material, and for this reason TEM and AFM analysis were required.

One of the characterization techniques employed to estimate the particle sizes (before and after the encapsulation process) and the coating thickness was a Scanning Electron Microscopy (SEM). This SEM system (Hitachi 800) has a feature that allows users to analyze a group of particles, reporting the total number of particles in the picture and the estimated diameter for each of them. Therefore, pictures of the samples were taken before and after the coating, with particle populations in the order of hundreds, establishing a particle size distribution for coated and uncoated CaO and TiO_2.

These results were essential in order to establish how the particle size was affected by the coating process and how significant the TEM results were. These results are summarized on Table 6.11, and the particle size distribution plots for the coated and uncoated CaO and TiO_2 are shown in Figures 6.15 through 6.18.

Table 6.11. Average Particle Size from SEM Analysis.

Particle	**# Measurements**	**$Do_{Average}$ (μm)**
Uncoated TiO_2	957	0.39
Coated TiO_2	543	0.40
Coated CaO	477	0.20
Uncoated CaO	806	0.25

The results obtained from the particle size distribution does not show much difference between the particle before and after processing. This indicates that the coating thickness is on the nanometer order, which is confirmed by the TEM data as well.

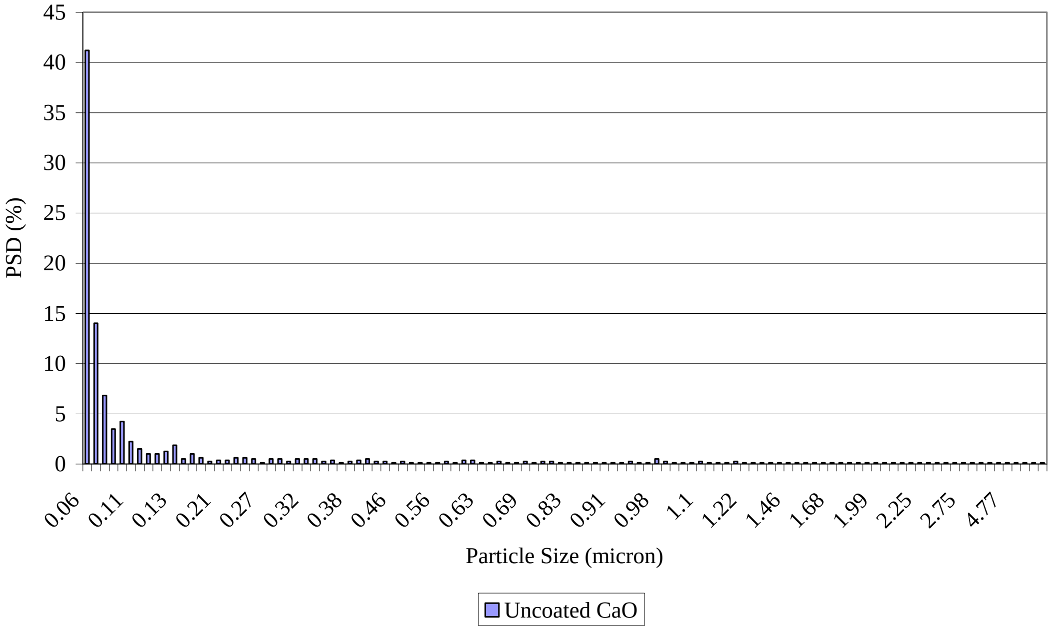

Figure 6.15. Particle Size Distribution for Uncoated CaO. (806 data points).

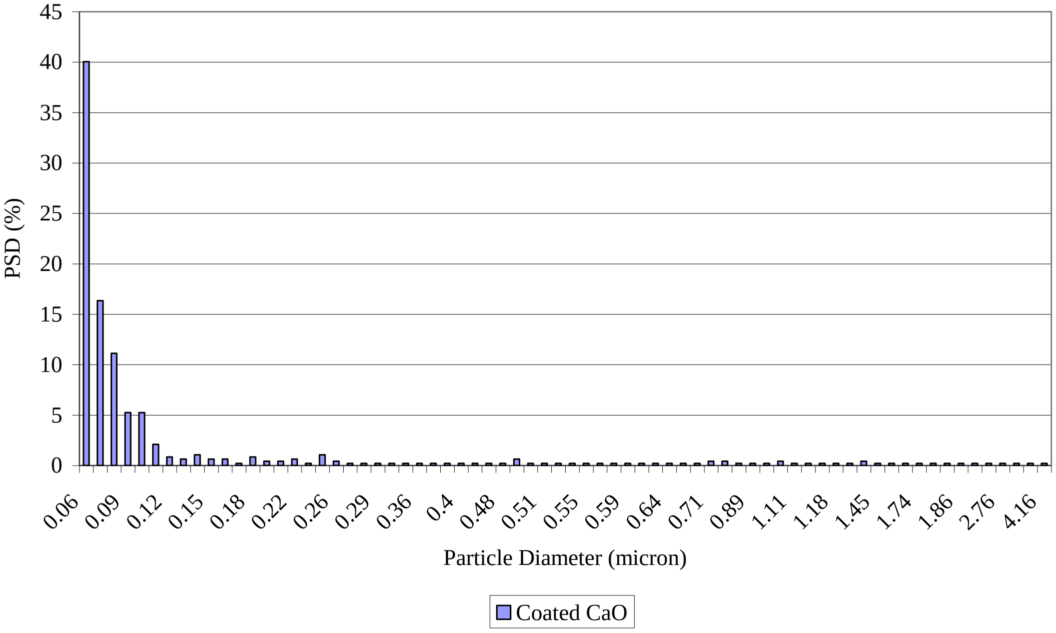

Figure 6.16. Particle Size Distribution for Encapsulated CaO. (477 data points).

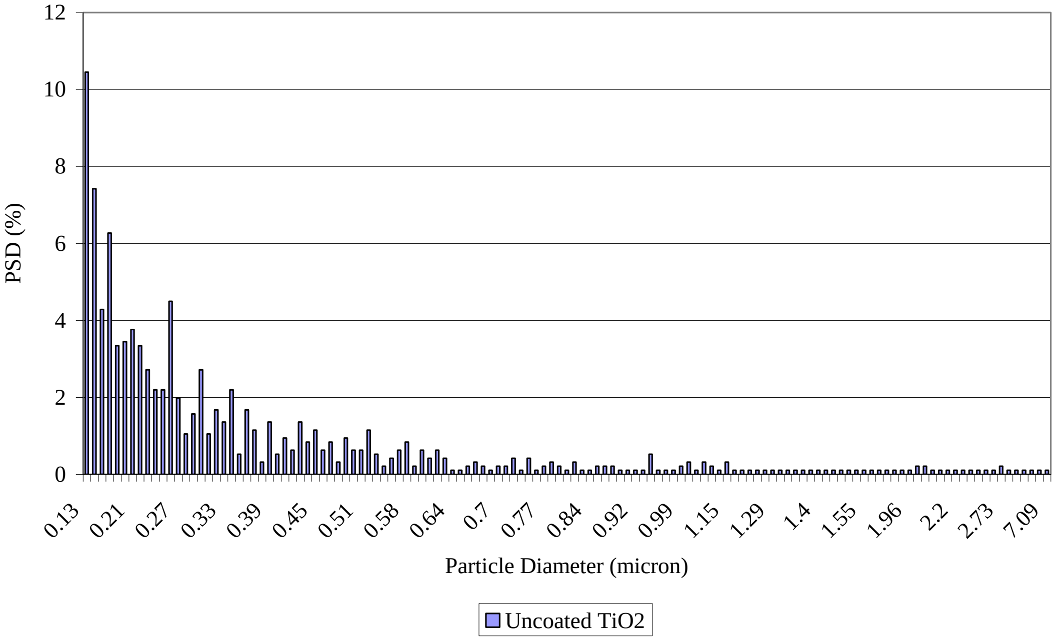

Figure 6.17. Particle Size Distribution for Uncoated $TiO_{2.}$ (957 data points).

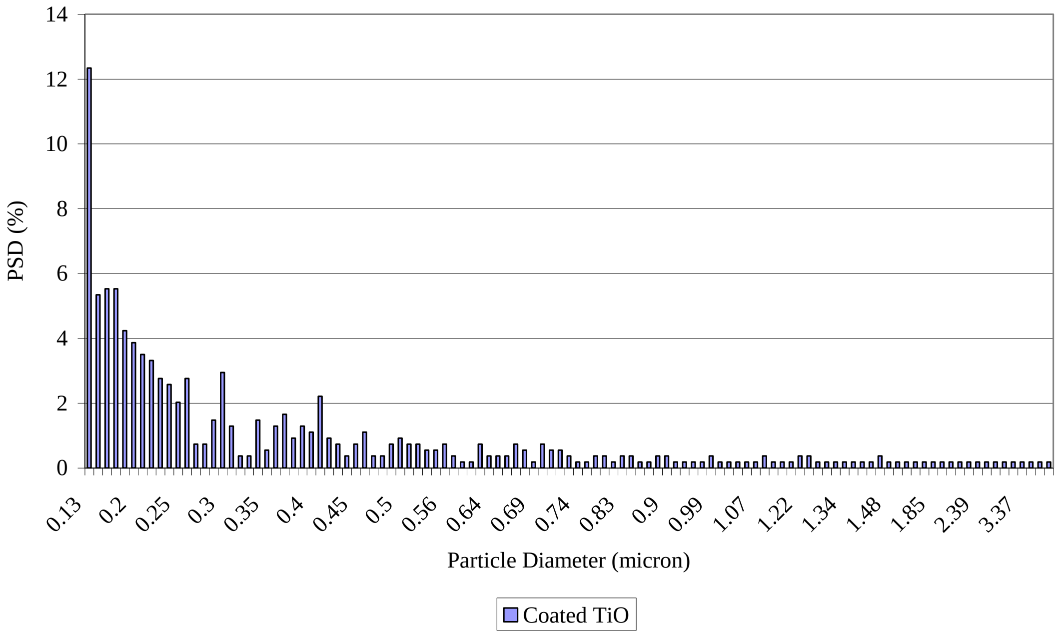

Figure 6.18. Particle Size Distribution for Encapsulated $TiO_{2.}$ (543 data points).

Another factor that had to be considered with the SEM was that samples contained encapsulated, non-encapsulated and polymer particles. Therefore, precise particle size and coating thickness required TEM analysis of the particles.

TEM analysis of the processed CaO and TiO_2 samples confirmed the fact that the particles were encapsulated, providing the shape of the encapsulated particles and the coating thickness. Transmission electron microscopy (TEM) is an imaging technique whereby a beam of electrons is transmitted through a specimen, then an image is formed, magnified and directed to appear on a CCD camera (CCDs are used in digital photography). The materials interact with the electron beam and the intensity of the transmitted beam is affected by the volume and density of the material through which it passes, for this reason in the following pictures it is possible to distinguish between the dark solid dense core made of inorganic material, CaO or TiO_2, and the organic polymer coating that is almost transparent to the electron beam.

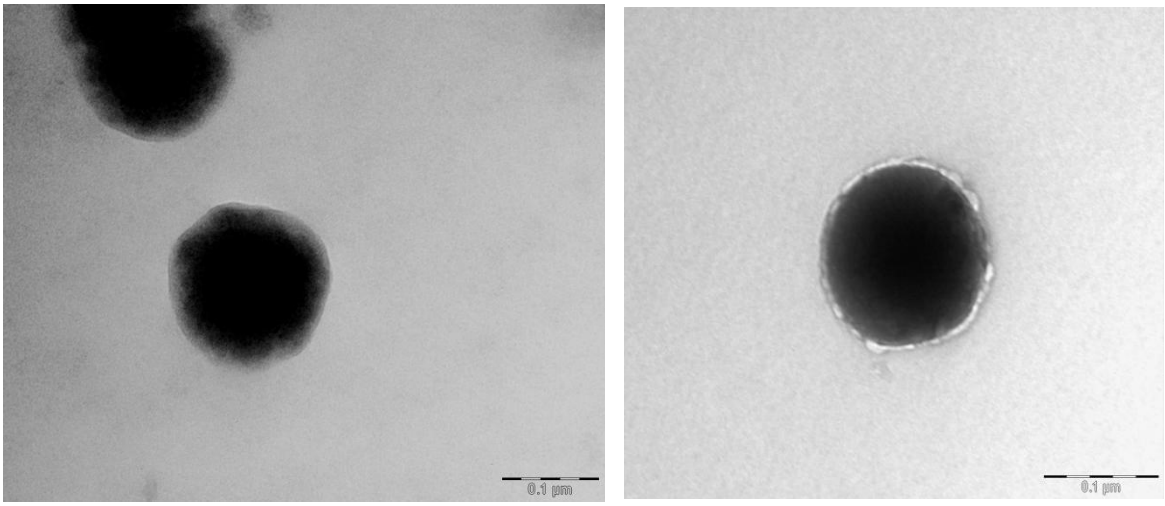

(a) (b)

Figure 6.19. TEM for Chitosan Encapsulated Particle.
(a) CaO Particles, (b) TiO_2 Particles.

Using several pictures taken for each of the processed samples, similar to the ones shown in Figure 6.19, average information about particle size and coating thickness were obtained and presented in Tables 6.12 and 6.13. The external diameter (D_o) and internal diameter (D_i) were calculated from measurements done by using Microsoft Office Visio 2003 when analyzing the digital TEM images for each particle. The bold numbers in each column represent the average values.

The experimental data showed that pressure, temperature and contact time are related: when pressure increased, the coating thickness and coverage increased as a logical consequence of solubility enhancement. As the temperature increased, the solubility of the polymer decreased, causing its rapid precipitation. This was desirable, since this encapsulation method was based on temperature perturbation, but if not controlled the polymer precipitated too fast and there was not enough time for the supercritical mixture to be absorbed over the particles' surface, producing agglomeration and a poor encapsulation process. The other factor considered in this encapsulation process was the contact time. In theory, the longer the exposure or contact time, the thicker the coating should be, but the experimental results did not back up this premise.

One encapsulation test where the CaO particles were stirred overnight at room temperature in the liquid mixture Chitosan-DMSO and then pressurized at 111 bar and 48.6ºC for 120 min was the experiment that showed the thinner coating and the inferior coverage.

Table 6.12. TEM Thickness Measurements for Encapsulated CaO Particles.

D_o (μm)	**D_i (μm)**	**Thickness (μm)**	**P (bar)**	**T (°C)**	**Contact Time (min)**
2.2208	1.3839	0.4185	120	45	45
0.5132	0.4095	0.0519	120	45	45
0.1736	0.1410	0.0163	120	45	45
1.3670	0.8970	0.2350	120	45	45
0.3430	0.2750	0.0340	120	45	45
0.9690	0.6450	0.1620	120	45	45
2.1648	1.8734	0.1457	120	45	45
0.3100	0.1650	0.0725	120	45	45
1.0077	**0.7237**	**0.1420**	**120**	**45**	**45**
0.2045	0.1372	0.0337	109	42	50
0.3577	0.1925	0.0826	109	42	50
0.2621	0.1376	0.0623	109	42	50
0.1193	0.0770	0.0212	109	42	50
0.1236	0.0817	0.0210	109	42	50
0.2464	0.1429	0.0518	109	42	50
0.2510	0.1019	0.0746	109	42	50
0.2862	0.1349	0.0757	109	42	50
0.2314	**0.1257**	**0.0528**	**109**	**42**	**50**
0.1725	0.0971	0.0377	111	49	30*
0.1081	0.0806	0.0138	111	49	30*
0.1639	0.1156	0.0242	111	49	30*
0.1400	0.0890	0.0255	111	49	30*
0.1360	0.0980	0.0190	111	49	30*
0.1480	0.0950	0.0265	111	49	30*
0.1682	0.1064	0.0309	111	49	30*
0.1480	0.0970	0.0255	111	49	30*
0.1481	**0.0973**	**0.0254**	**111**	**49**	**30***

*The system chitosan-DMSO-CaO was kept at room conditions for 12h with constant stirring before pressurization for 30 min.

Table 6.13. TEM Thickness Measurements for Encapsulated TiO_2 Particles.

D_o (μm)	**D_i (μm)**	**Thickness (μm)**	**P (bar)**	**T (°C)**	**Contact Time (min)**
0.1513	0.1371	0.0071	120	45	60
0.1531	0.1424	0.0054	120	45	60
0.3329	0.2472	0.0429	120	45	60
0.5143	0.3434	0.0855	120	45	60
0.2694	0.1220	0.0737	120	45	60
0.1153	0.1048	0.0053	120	45	60
0.1520	0.1400	0.0060	120	45	60
0.2430	0.1950	0.0240	120	45	60
0.4240	0.2950	0.0645	120	45	60
0.3920	0.2330	0.0795	120	45	60
0.1920	0.1130	0.0395	120	45	60
0.1340	0.1220	0.0060	120	45	60
0.1980	0.1680	0.0150	120	45	60
0.3340	0.2450	0.0445	120	45	60
0.4080	0.2640	0.0720	120	45	60
0.2920	0.1730	0.0595	120	45	60
0.1630	0.1180	0.0225	120	45	60
0.1660	0.1450	0.0105	120	45	60
0.2575	**0.1838**	**0.0368**	**120**	**45**	**60**
0.1343	0.1067	0.0138	110	44	73
0.1060	0.0512	0.0274	110	44	73
0.1450	0.1242	0.0104	110	44	73
0.1202	0.0546	0.0328	110	44	73
0.1500	0.1260	0.0120	110	44	73
0.1200	0.0790	0.0205	110	44	73
0.1260	0.0880	0.0190	110	44	73
0.1330	0.1220	0.0055	110	44	73
0.1430	0.1250	0.0090	110	44	73
0.1440	0.0970	0.0235	110	44	73
0.1490	0.1300	0.0095	110	44	73
0.2190	0.1860	0.0165	110	44	73
0.2390	0.1990	0.0200	110	44	73
0.3300	0.2340	0.0480	110	44	73
0.3170	0.1730	0.0720	110	44	73
0.1950	0.1730	0.0110	110	44	73
0.2690	0.1420	0.0635	110	44	73
0.1390	0.1030	0.0180	110	44	73
0.2750	0.1730	0.0510	110	44	73
0.2340	0.1390	0.0475	110	44	73
0.184	**0.131**	**0.027**	**110**	**44**	**73**

Once demonstrated by TEM results that the particles were coated and an average coating thickness was estimated, the next step was to study the morphology of the coating, and this was obtained from AFM. The atomic force microscope (AFM) is a high-resolution type of scanning probe microscope (the term 'microscope' in the name is actually a misnomer because it implies looking, while in fact the information is gathered by "feeling" the surface with a mechanical probe). The AFM is one of the foremost tools for imaging, measuring and manipulating matter at the nanoscale.

This analysis technique was chosen because AFM provides a true three-dimensional surface profile. Additionally, samples viewed by AFM do not require any special treatments (such as metal/carbon coatings on SEM) that in this case would irreversibly change the sample, making it impossible to study the true morphology of the coating material.

In Figures 6.20 and 6.21, the roughness of uncoated and coated CaO particles sample are compared, showing that once coated, the particle surface is smoother, with roughness changing from 34.548 nm for the uncoated CaO particle to 2.660 nm for the encapsulated particle.

Figures 6.22 and 6.23 (Height and Phase) for the uncoated and encapsulated CaO particles, are another evidence of the encapsulating process, since the uncoated particles present a crystal shape structure and the encapsulated ones have a rounded coated shape, confirming the results obtained by the TEM, where complete encapsulated particles were found. The Section Analysis presented in Figures 6.24 and 6.25 show particles with diameters of less than one micron, confirming the particle sizes obtained with TEM and SEM, as well as differentiating the external angular crystal shape of the uncoated particles and the rounded surface of the coated ones.

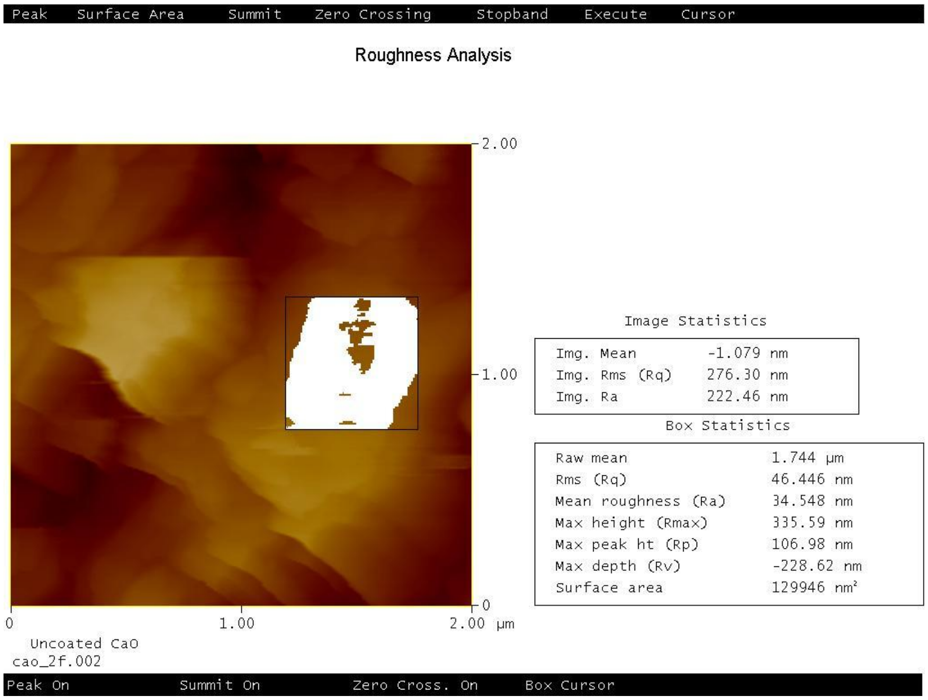

Image Statistics

```
Img. Mean        -1.079 nm
Img. Rms (Rq)    276.30 nm
Img. Ra          222.46 nm
```

Box Statistics

```
Raw mean                1.744 µm
Rms (Rq)                46.446 nm
Mean roughness (Ra)     34.548 nm
Max height (Rmax)       335.59 nm
Max peak ht (Rp)        106.98 nm
Max depth (Rv)          -228.62 nm
Surface area            129946 nm²
```

Figure 6.20. Uncoated CaO Roughness Analysis.

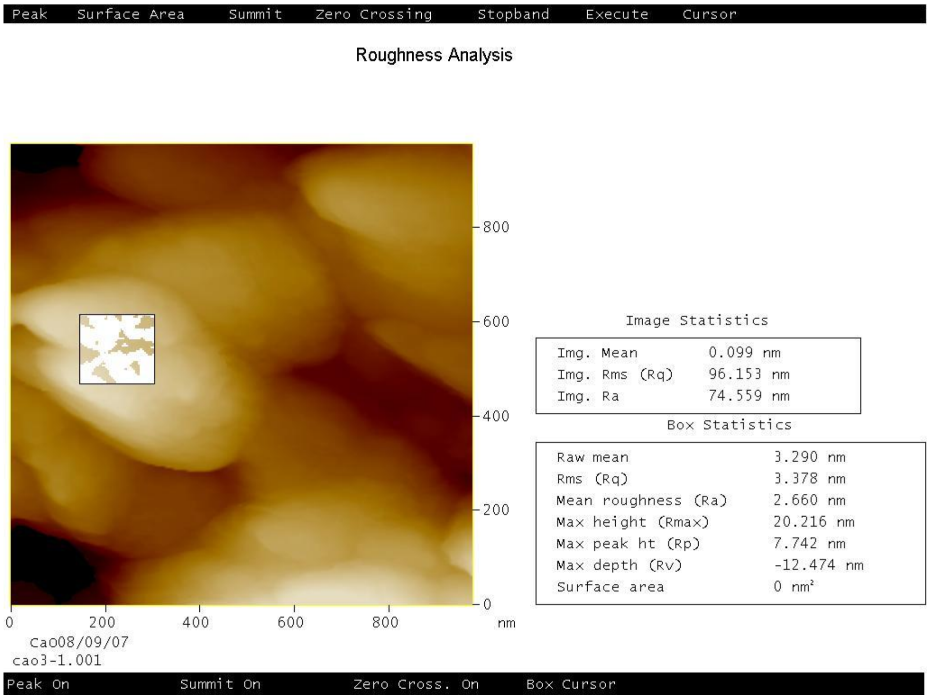

Image Statistics

```
Img. Mean        0.099 nm
Img. Rms (Rq)    96.153 nm
Img. Ra          74.559 nm
```

Box Statistics

```
Raw mean                3.290 nm
Rms (Rq)                3.378 nm
Mean roughness (Ra)     2.660 nm
Max height (Rmax)       20.216 nm
Max peak ht (Rp)        7.742 nm
Max depth (Rv)          -12.474 nm
Surface area            0 nm²
```

Figure 6.21. Coated CaO Roughness Analysis.

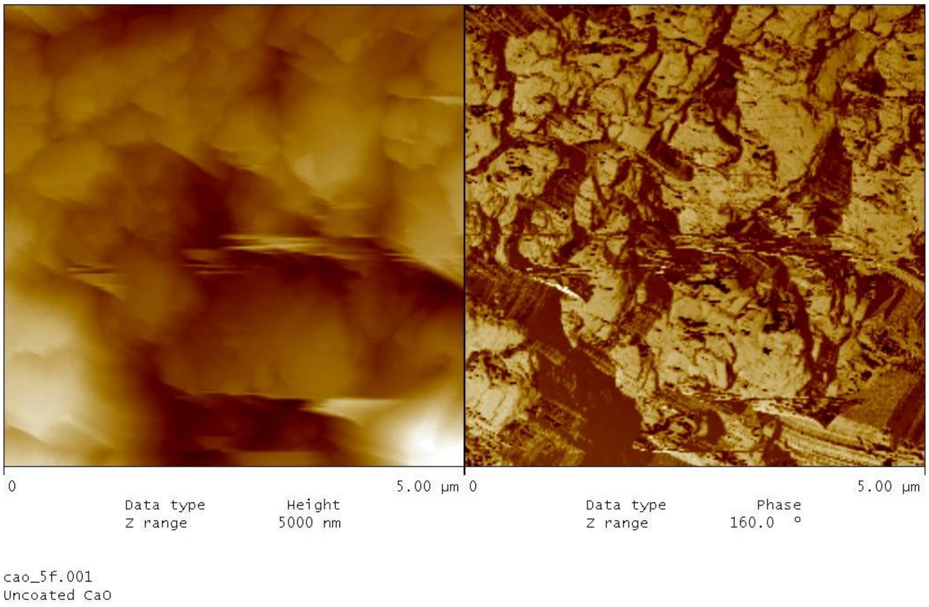

Figure 6.22. Uncoated CaO Height and Phase.

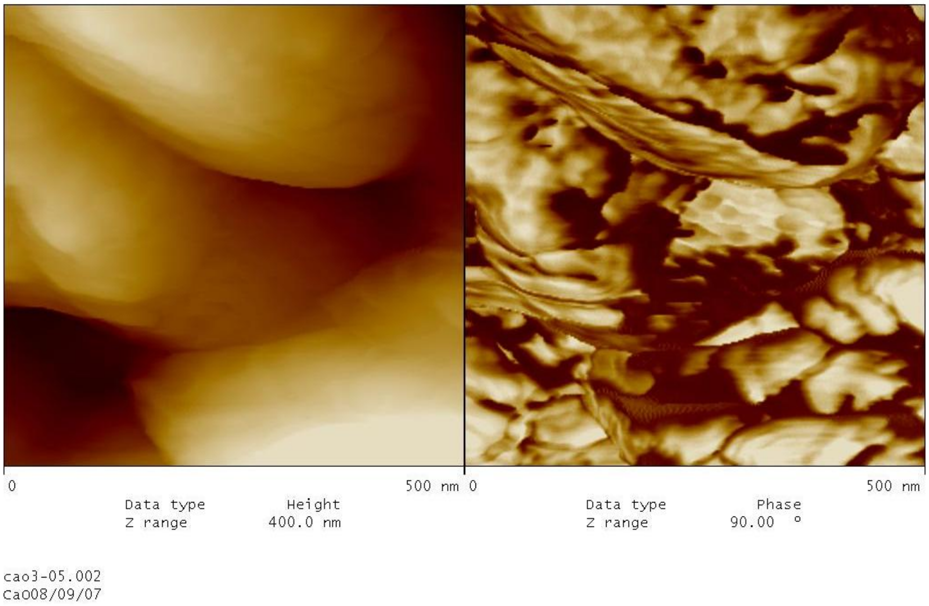

Figure 6.23. Coated CaO Height and Phase.

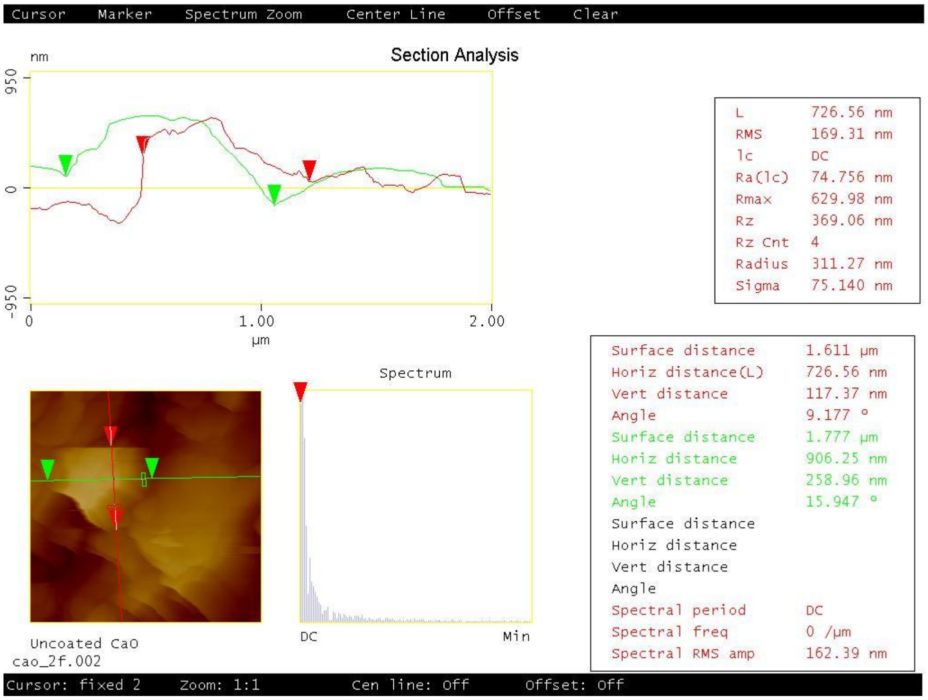

L 726.56 nm
RMS 169.31 nm
lc DC
Ra(lc) 74.756 nm
Rmax 629.98 nm
Rz 369.06 nm
Rz Cnt 4
Radius 311.27 nm
Sigma 75.140 nm

Surface distance 1.611 µm
Horiz distance(L) 726.56 nm
Vert distance 117.37 nm
Angle 9.177 °
Surface distance 1.777 µm
Horiz distance 906.25 nm
Vert distance 258.96 nm
Angle 15.947 °
Surface distance
Horiz distance
Vert distance
Angle
Spectral period DC
Spectral freq 0 /µm
Spectral RMS amp 162.39 nm

Uncoated CaO
cao_2f.002

Cursor: fixed 2 Zoom: 1:1 Cen line: Off Offset: Off

Figure 6.24. Uncoated CaO Section Analysis.

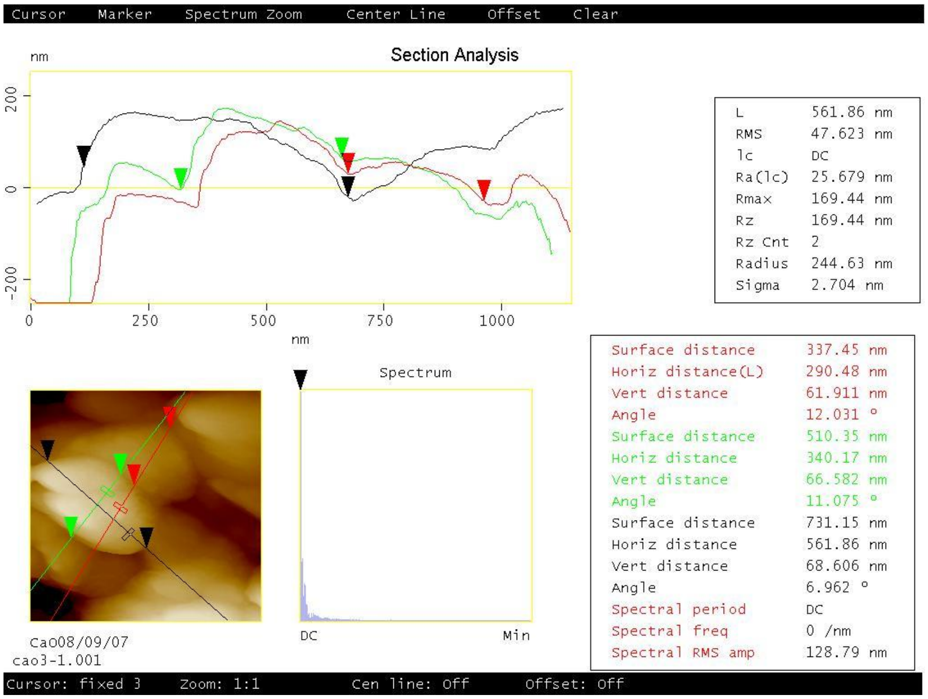

L 561.86 nm
RMS 47.623 nm
lc DC
Ra(lc) 25.679 nm
Rmax 169.44 nm
Rz 169.44 nm
Rz Cnt 2
Radius 244.63 nm
Sigma 2.704 nm

Surface distance 337.45 nm
Horiz distance(L) 290.48 nm
Vert distance 61.911 nm
Angle 12.031 °
Surface distance 510.35 nm
Horiz distance 340.17 nm
Vert distance 66.582 nm
Angle 11.075 °
Surface distance 731.15 nm
Horiz distance 561.86 nm
Vert distance 68.606 nm
Angle 6.962 °
Spectral period DC
Spectral freq 0 /nm
Spectral RMS amp 128.79 nm

Ca008/09/07
cao3-1.001

Cursor: fixed 3 Zoom: 1:1 Cen line: Off Offset: Off

Figure 6.25. Coated CaO Section Analysis.

6.5. Coating Analysis and Characterization

As mentioned previously, there is no analytical data published about this particular Chitosan Oligosaccharide Lactate; for this reason some characterization was needed. In order to determine if the encapsulating process was causing some changes to the polymer, all analytical tests were performed before and after processing.

FTIR analyses were performed to four Chitosan samples of different molecular weights and the Oligosaccharide Lactate before and after the encapsulating process, to determine if there were any changes on polymer. Figure 6.26 shows that all the plots are similar, confirming that all the Chitosan peaks were present before and after the encapsulation process.

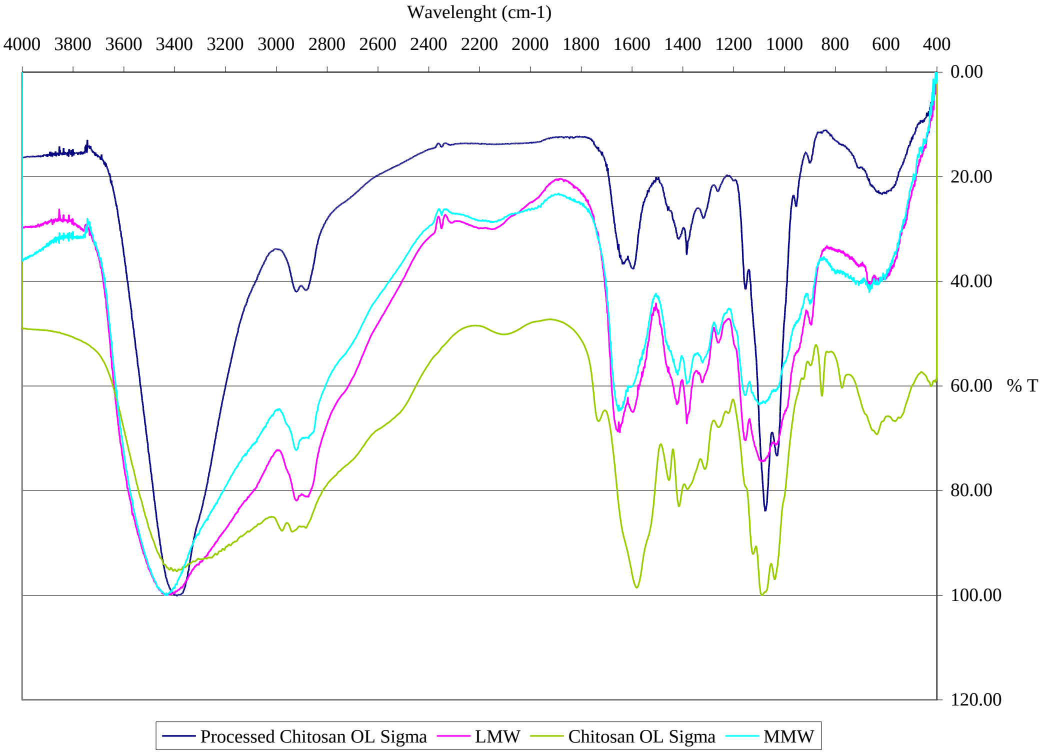

Figure 6.26. FTIR Plot for Chitosan Oligosaccharide Lactate. (OL Sigma).
Before and after processing is shown, as well as Chitosan Low Molecular Weight (LMW) and Medium Molecular Weight (MMW).

The δ-NH deformations were in the 1600 cm^{-1} (1539 cm^{-1} amine and 1635 cm^{-1} amide) range. The ν-CO band was at 1074 cm^{-1}, stretching deformation ν-CH was at 2920-2945 cm^{-1}, ν-OH was at 3435 cm^{-1}, and ν-CN was at 1153 cm^{-1}. These were all similar to the ones found in the literature reviewed (Cardenas 2004, Jang 2003 and Zhou 2002).

The only difference observed was that the processed Oligosaccharide Lactate spectrum had two peaks seeming to be stronger, one at 3435 cm^{-1}, that corresponded to ν-OH deformations, which could be an indication of some water absorbed in the Chitosan; and the other one was around 1060cm^{-1}, for the sulfoxide group, indicating that some DMSO remained absorbed in the polymer. However this peak overlapped with the ν-CO band at 1074 cm^{-1} and ν-CN at 1153 cm^{-1}.

Using another analysis method, a DSC-TGA device was used to characterize the polymers, by measuring both heat flow and weight changes in a material as a function of temperature on time in a controlled atmosphere. This is a very useful technique because the information obtained allows differentiation between endothermic and exothermic events which have no associated weight loss (e.g. melting, crystallization, glass transition) and those which involve a weight loss (e.g. degradation).

In Figure 6.27, a DSC-TGA for Chitosan Oligosaccharide Lactate before processing is shown, where a phase change or glass transition temperature was observed at 106.1°C (no weight loss) and decomposition was seen at 148.96 °C accompanied by a weight loss of 21.16%. Glass transition temperatures have been reported by Y. Dong 2004 for higher molecular weights Chitosans (450,000 Da) around 130-150 °C, but no data was found for Chitosan Oligosaccharide Lactate. Not even the provider (Sigma Aldrich) had this data available in order to compare the results.

Figure 6.28 shows a DSC-TGA for the processed Chitosan Oligosaccharide Lactate, where decomposition at 125.8 °C accompanied by a weight loss of 49.92% was observed. These results indicate that the original polymer was more stable and this is probably a consequence of the water and DMSO absorbed by the Chitosan during processing or manipulation, as indicated by the FTIR (increase of ν-OH 3435 cm^{-1} peak) and the NMR tests presented next, and confirmed by studies done by Ratajska on water soluble Chitosan.

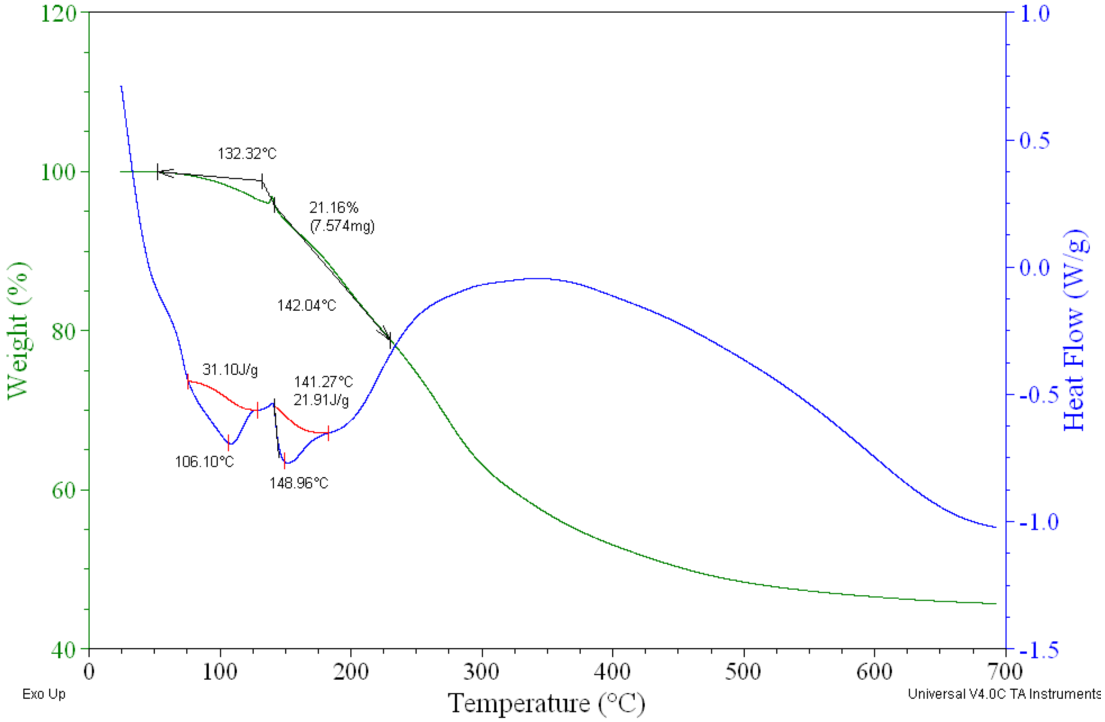

Figure 6.27. DSC-TGA for Chitosan Oligosaccharide Lactate.

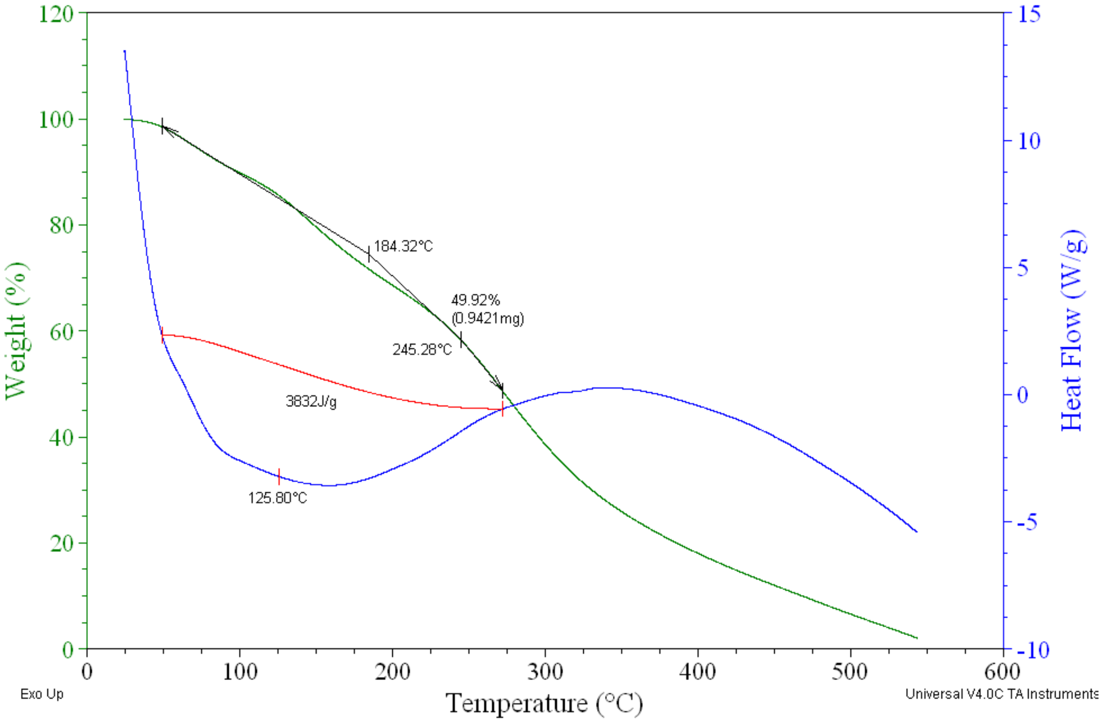

Figure 6.28. DSC-TGA for Processed Chitosan Oligosaccharide Lactate.

From a theoretical proton NMR of the monomer made in ChemDraw from CambridgeSoft, which is generally a good estimate, we can see the expected peaks in Figure 6.29.

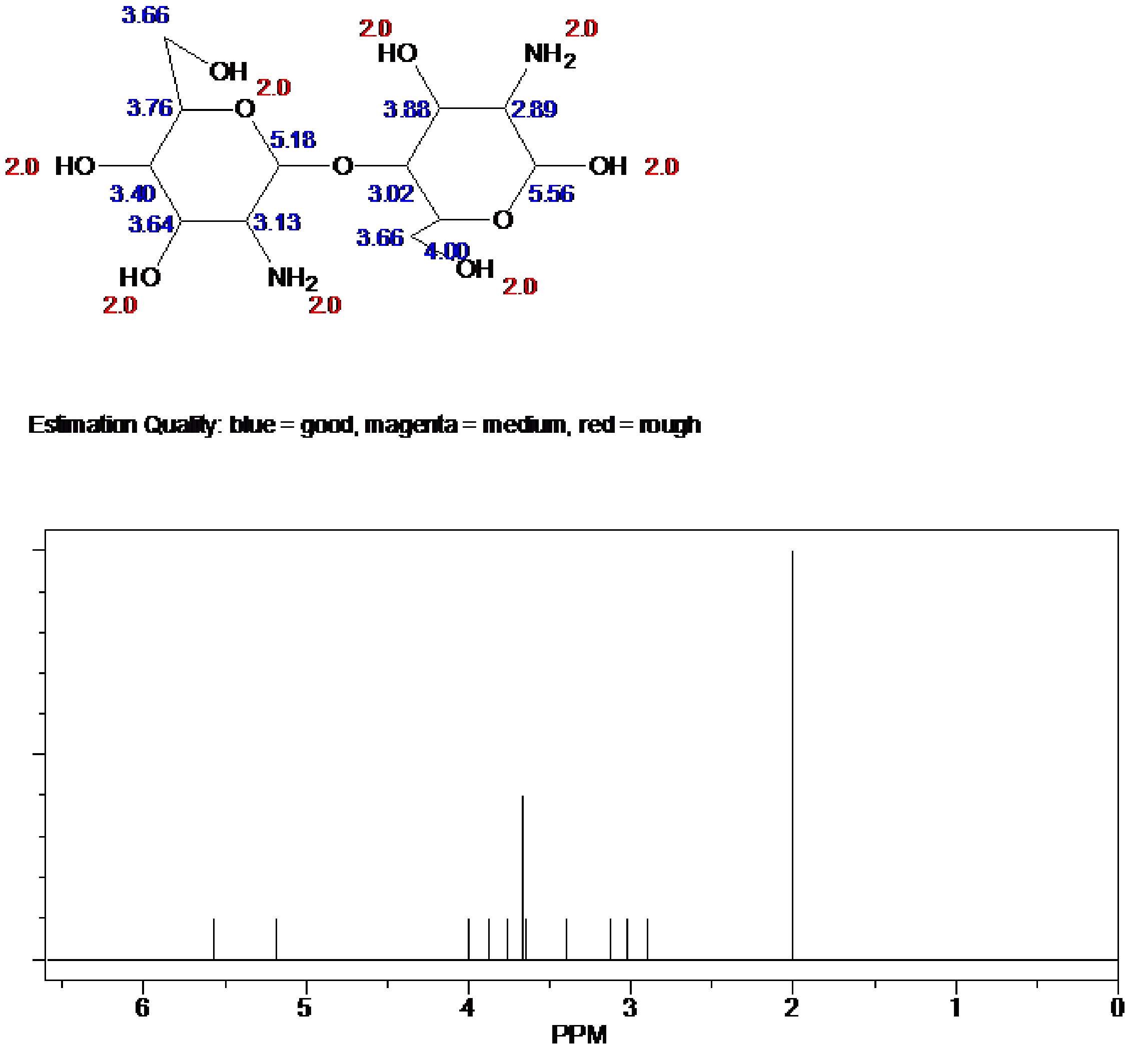

Figure 6.29. Proton NMR for Chitosan Monomer (ChemDraw).

The NMR done at Inova-400 (Figure 6.30) looks pretty well resolved for the peaks of the pure Chitosan Oligosaccharide Lactate, if compared with the NMR of the monomer made with ChemDraw. The DMSO peak came around 2.5-2.62 ppm. In addition, there was always water absorbed by the DMSO and it appeared around 3.3 ppm.

In Figure 6.31, a Proton NMR of the processed Chitosan Oligosaccharide Lactate is presented and it can be seen is that, although almost all DMSO was extracted from the sample (SEM-EDS data), there was still some DMSO present. Also, the large peak between 2-3 ppm was residual DMSO and the other large peak between 3-4 ppm was water, probably absorbed from the environment, since the sample and DMSO are highly hygroscopic. This caused some of the peaks shifting to 5-6 ppm and the rest of the peaks were buried under DMSO and water peaks, since the encapsulation process described did not change the chemical structure of the polymer.

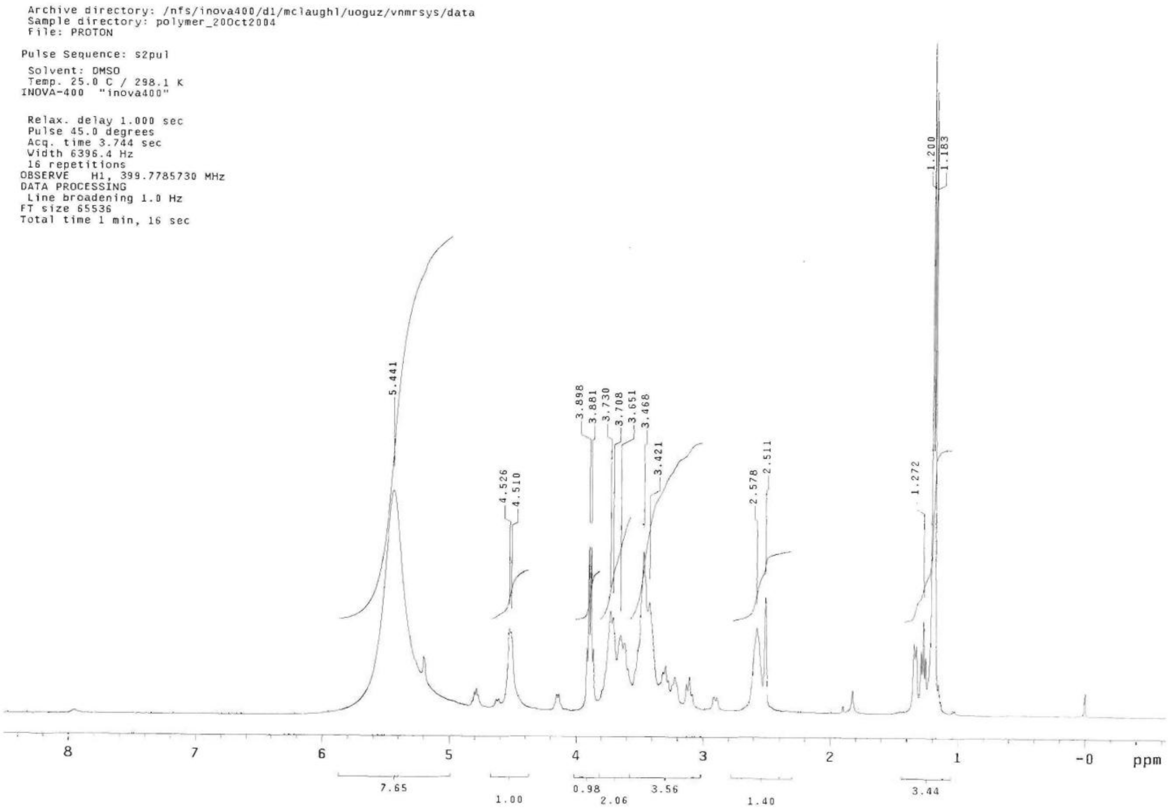

```
 Archive directory: /nfs/inova400/d1/mclaughl/uoguz/vnmrsys/data
 Sample directory: polymer_20Oct2004
 File: PROTON

Pulse Sequence: s2pul

 Solvent: DMSO
 Temp. 25.0 C / 298.1 K
INOVA-400  "inova400"

 Relax. delay 1.000 sec
 Pulse 45.0 degrees
 Acq. time 3.744 sec
 Width 6396.4 Hz
 16 repetitions
OBSERVE   H1, 399.7785730 MHz
DATA PROCESSING
 Line broadening 1.0 Hz
FT size 65536
Total time 1 min, 16 sec
```

Figure 6.30. Proton NMR Pure Chitosan Oligosaccharide Lactate.

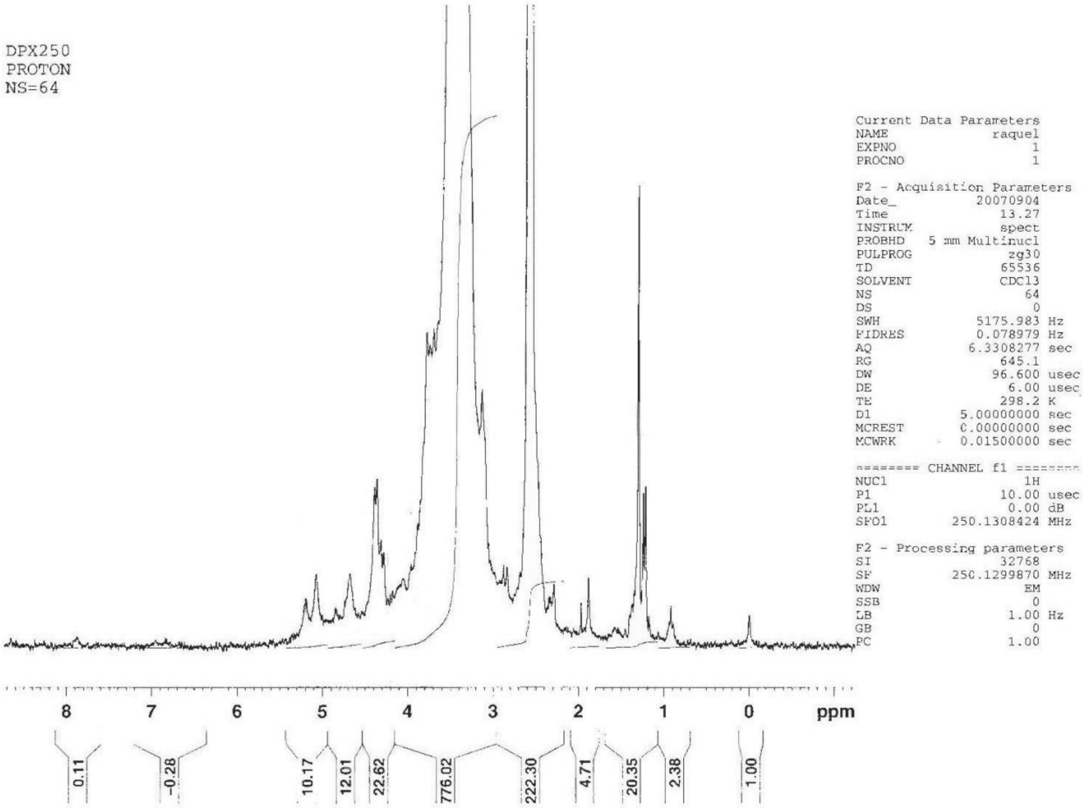

```
Current Data Parameters
NAME              raquel
EXPNO                  1
PROCNO                 1

F2 - Acquisition Parameters
Date_           20070904
Time               13.27
INSTRUM            spect
PROBHD   5 mm Multinucl
PULPROG             zg30
TD                 65536
SOLVENT            CDCl3
NS                    64
DS                     0
SWH             5175.983 Hz
FIDRES          0.078979 Hz
AQ             6.3308277 sec
RG                 645.1
DW                96.600 usec
DE                  6.00 usec
TE                 298.2 K
D1            5.00000000 sec
MCREST        0.00000000 sec
MCWRK         0.01500000 sec

======== CHANNEL f1 ========
NUC1                  1H
P1                 10.00 usec
PL1                 0.00 dB
SFO1         250.1308424 MHz

F2 - Processing parameters
SI                 32768
SF           250.1299870 MHz
WDW                   EM
SSB                    0
LB                  1.00 Hz
GB                     0
PC                  1.00
```

Figure 6.31. Proton NMR Processed Chitosan Oligosaccharide Lactate.

CHAPTER 7

CONCLUSIONS AND RECOMMENDATIONS

Chitosan Oligosaccharide Lactate is a relatively new biopolymer with a low molecular weight (5000Da), when compared with the other members of the Chitosan family where the molecular weight ranges 50,000 to 375,000 Da. This specific characteristic makes Chitosan Oligosaccharide Lactate soluble at regular mucus pH 6.5, showing potential application in the pharmaceutical and food industries. What was found during this research is that it is not soluble on DCM, chloroform, acetone, ethanol or pure supercritical $CO_{2,}$ but it is highly soluble in water and DMSO. DMSO, being readily accepted for targeted delivery, can be used as a cosolvent in supercritical procedures.

The main objective of this research was to perform the encapsulation of fine dry powders using supercritical CO_2. This necessitated basic information on phase behavior and solubility for the system DMSO-CO_2. The experimental effort to date had focused on high DMSO concentrations used for antisolvent procedures with limited use for DMSO as a cosolvent in encapsulation procedures. Cloud point data was generated for the system DMSO-CO_2 in a temperature range of 314.2 °K to 328.2 °K and pressures from 89 to 133.5 bars and DMSO molar fractions between 5 to 10%. The standard deviation based on the five readings made for each data point is less than one bar, indicating that this experimental method is accurate. The results that were obtained line up with existent literature data reported by Rajasingam 2004, Gonzalez 2002 and Kordikowski 1995, observing some variations (± 4 bar) that can be attributed to the different experimental methods designed to work with DMSO concentrations over 10% molar basis.

Chitosan-DMSO-CO_2 cloud point and solubility data was generated in a temperature range of 308.2 °K to 318.2 °K and pressures from 92.4 to 156.7 bars with a standard deviation for each data point of less than one bar. This is an important contribution from this research, since there was previously no information available for this system. Furthermore, as is well known, modeling the behavior of a supercritical mixture including a polymer is exceedingly difficult, since polymers are substances composed of many single molecules or repeating units (monomers) connected by covalent chemical bonds, interacting among themselves and the solvents used at supercritical conditions.

From the solubility experiments, it can be stated that at isothermal conditions the Chitosan solubility increases proportionally with the pressure; and at constant pressure the solubility decreases with temperature increments. This is a general effect that is suitable to the short-range attractive forces between solvent and solute. The solubility of a low-volatile solute, like Chitosan, is enhanced as the density of the volatile solvent (CO_2) increases, as a consequence of temperature drop in an isobaric process or pressure rise in an isothermal process.

The fact that DMSO solubility in supercritical CO_2 is high compared to the solubility of Chitosan Oligosaccharide Lactate in $SCCO_2$ was the reason to try a temperature change at isobaric conditions to disrupt the equilibrium of this ternary system. The experimental work performed establishes that by increasing the temperature at constant pressure, the solubility of the Chitosan decreases, causing it to precipitate over the particles that need to be encapsulated while the DMSO stays solubilized in the $SCCO_2$.

Fluidization of CaO and TiO_2 particles with diameters under one micron was achieved in a mini fluidized bed (volume = 60 ml) with $SCCO_2$. The average CO_2 mass flow used to fluidize these particles was 2 to 5g/min, calculated with Wen & Yu 1966, as recommended by Carsten Vogt, 2005.

The performance of this encapsulation method for dry powders particles was proved by encapsulating calcium oxide (CaO, non porous) and titanium dioxide (TiO_2, porous) particles with diameters under one micron using Chitosan Oligosaccharide Lactate.

This research confirms FTIR and EDS as valuable techniques to verify the presence of Chitosan in the encapsulated particle and also shows that almost all DMSO was removed during extraction. TEM analysis provided visual confirmation that CaO and TiO_2 particles of 1 micron or less were encapsulated with a thickness of 5 nm or less, and these results coincided with SEM and AFM analysis.

The experimental data obtained validates the fact that solubility is a function of pressure and temperature. Pressure increments at constant temperature cause coating thickness augmentation and coverage improvement as a logical consequence of solubility enhancement. On the other hand, temperature increments diminish the solubility of the polymer, causing its rapid precipitation, which is desirable since this encapsulation method is based on temperature perturbation. However, when not controlled the polymer precipitates too fast, and if contact time was not enough for the supercritical mix to get adsorbed over the particles, it results in surface agglomeration and a poor encapsulation.

SEM samples of 477 to more than 900 particles provided a particle size distribution, where more than 90% of the CaO and TiO_2 particles had been confirmed to have a diameter under one micron.

AFM showed particle roughness of 2-4 nm for the encapsulated sample and 36 to 46 nm or higher for uncoated ones, proving the particles were encapsulated, since the surface is smoother after the coating is applied, also the uncoated particles presented a crystal angular shape structure when compared to the encapsulated ones with a rounded shape.

FTIR analyses were performed on four Chitosan samples of different molecular weights and the Oligosaccharide Lactate before and after the encapsulating process. All the plots are similar, confirming the presence of Chitosan before and after the encapsulation process. The only difference observed is that the processed Oligosaccharide Lactate spectrum has two peaks seeming to be stronger, one at 3435cm^{-1}, that corresponds to ν-OH deformations (which can be an indication of some water absorbed in the Chitosan) and the other one at around 1060cm^{-1} for the sulfoxide group (indicating that some DMSO remains absorbed in the polymer). However, this peak overlaps with the ν-CO band at 1074 cm^{-1} and ν-CN at 1153 cm^{-1}.

DSC-TGA analysis performed on Chitosan Oligosaccharide Lactate indicates that the original polymer appears to be more thermally stable and this is probably a consequence of the water adsorbed by the Chitosan during or after processing, as confirmed by the NMR tests. DSC-TGA for Chitosan Oligosaccharide Lactate before processing shows a phase change or glass transition temperature at 106.1°C (no weight loss) and decomposition at 148.96 °C, accompanied by a weight loss of 21.16%, while processed Chitosan Oligosaccharide Lactate had decomposition at 125.8 °C, accompanied by a weight loss of 49.92%.

In conclusion, the solubility data and encapsulation results obtained from this research are valuable as new information. This new data can be the starting point for many other research works, including experimental and modeling. It was proven experimentally that Chitosan Oligosaccharide Lactate can be solubilized in supercritical carbon dioxide using DMSO as a cosolvent (5-10%) at temperatures between 308.2 °K to 318.2 °K and pressures from 92.4 to 156.7 bars. This information was used to coat CaO and TiO_2 particles (0.2-2 μm) at 92-156 bar and 308-318°K, using a temperature perturbation technique in a fluidized bed.

The mass balance presented in Appendix I indicates that the solubility decreases inside the encapsulation cell, as the temperature was raised at a constant pressure to promote the polymer precipitation. The results from Tables I.3 and I.4 indicate that the volume of $SCCO_2$ used to remove DMSO was higher than required, which could cause Chitosan removal, reducing encapsulant thickness.

The results obtained during this experimental research work are encouraging and for this reason some improvements are recommended for future work. In order to obtain more experimental data in less time from the dynamic solubility set-up, it would be useful to have the solubility cell and the mixer enclosed in an oven instead of the water bath, as well as having a densitometer connected to the extraction cell.

The encapsulation cell used was a modified Jerguson gauge, which included some Teflon baffles especially designed to avoid disruption of the flow profile. These inserts had to be readjusted after every single experiment, taking at least eight hours before the cell could be operated again. For this reason, redesigning and building the body of the cell as one solid piece should be considered, as well as an easy opening and closing system. Having a full body Safire cell on the solubility set-up would make it possible to obtain all the phase transitions for multi-component mixtures, facilitating future modeling attempts for this and other supercritical systems.

Due to the hygroscopic nature of Chitosan Oligosaccharide Lactate, some agglomeration could be attributed to moisture pick-up over time; for future experiments it is recommended to store samples in absolute dry conditions.

REFERENCES

- Akihisa N., Eiichi U., Chiaki N. (2005) Patent JP2005232053.
- Akman U. and Sunol A. K. “Modeling of supercritical desorbers with an equation-of-state-based isotherm.” *AIChE Journal*, 37, no. 2, (1991): 215-224.
- Andrady A. L., Torikai A. and Kobatake T. “Spectral sensitivity of chitosan photo-degradation.” *Journal of Applied Polymer Science*, 62, no. 9, (1996): 1465-1471.
- Benita, Simon. *Microencapsulation methods and industrial applications*. Boca Raton: CRC Press, 2006.
- Benoit J. P., Richard J., Thies C. (1996) Patent FR 2753639, WO 96/13136.
- Benoit J. P., Rolland H., Thies C., Van de Velde V. (1996) Patent EP 0706821, WO 96/11055.
- Bleich J. and Muller B. W. “Production of drug loaded microparticles by the use of supercritical gases with the Aerosol Solvent Extraction System (ASES) process.” *Journal of Microencapsulation*, 13, no. 2, (1996): 131-139.
- Bolz A., Deiters K., Peters C. J. and de Loos T. W. “Nomenclature for Phase Diagrams with Particular Reference to Vapour-Liquid and Liquid-Liquid Equilibria.” *International Union of Pure and Applied Chemistry (IUPAC), Physical Chemistry Division-Commission of Thermodynamics*, 70, no. 11, (1998): 2233-2257.
- Brannon-Peppas L., “Polymers in controlled drug delivery.” *Medical Plastic and Biomaterials Magazine*, November, (1997).
- Buerger A., Raschck T., Voigt N., Schwanke F. (2003) Patent WO03075881.
- Calvo L., Holmes J. D., Yates M. Z. and Johnston K. P. “Steric stabilization of inorganic suspensions in carbon dioxide.” *Journal of Supercritical Fluids*, 16, (2000): 247-260.
- Cardenas G. and Miranda P. “FTIR and TGA studies of chitosan composite films.” *Journal of Chilean Chemical Society*, 49, no. 4, (2004): 291-295.

- Chang C. J., Randolph A. D. “Precipitation of micronized organic particles from supercritical fluids.” *AIChE Journal*, 35, (1989): 1876-1882.

- Chaubal M. “Using Chitosan as an Excipient for Oral Drug Delivery”. Available from www.drugdeliverytech.com/cgi-bin/articles.cgi?idArticle=131.

- Chimowitz E. H. and Pennisi K. J. “Process synthesis concepts for supercritical gas extraction in the crossover region.” *AIChE Journal*, 32, no. 10, (1986):1665.

- Chiou A. H., Cheng H. C., Wang D. P. “Micronization and microencapsulation of felodipine by supercritical carbon dioxide.” *Journal of Microencapsulation*, 23, no. 3, (2006): 265-276.

- Cooper, A. I. “Polymer synthesis and processing using supercritical carbon dioxide.” *Journal of Materials Chemistry*, 10, (2000): 207-234.

- Cunningham M. F., Mahabadi H. K. Patent US5514514.

- Dalian Medicine Institute (1998). Patent CN1221607.

- Deiters U. K. and Pegg I. L. “Systematic Investigation of the Phase Behaviour in Binary Fluid Mixtures. I. Calculations Based on the Redlich-Kwong Equation of State.” *Journal of Chemical Physics*, 90, (1989): 6632-6641.

- DeSimone, J. M. and Keiper, J. S. “Surfactants and self-assembly in carbon dioxide.” *Current Opinion in Colloid Interfacial Science*, 5, (2001): 333-341.

- Duarte A. R. C., Sousa Costa M., Simplicio A. L., Cardoso M. M., Duarte C. M. M. “Preparation of controlled release microspheres using supercritical fluid technology for delivery of anti-inflammatory drugs.” *International Journal of Pharmaceutics*, 308, (2006): 168-174.

- Elgin J. C. and Weinstock J. J. “Phase Equilibrium at Elevated Pressures in Ternary Systems of Ethylene and Water with Organic Liquids: Salting out with a Supercritical Gas.” *Journal of Chemical Engineering Data*, 4, no. 1, (1959): 3-12.

- Elvassore N., Bertucco A. and Caliceti P. “Production of Protein-Loaded Polymeric Microcapsules by Compressed CO2 in a Mixed Solvent.” *Industrial and Engineering Chemistry Research*, 40, (2001): 795-800.

- Falk R., Randolph T. W., Meyer J. D., Kelly M. R., Manning M. C. "Controlled release of ionic compounds from poly (L-lactide) microspheres produced by precipitation with a compressed antisolvent." *Journal of Controlled Release*, 44, (1997): 77–85.

- Glebov E. M., Yuan L., Krishtopa L. G., Usov O. M., and Krasnoperov L. N. Coating of Metal Powders with Polymers in Supercritical Carbon Dioxide. *Industrial & Engineering Chemistry Research*, 40, no. 19, (2001): 4058-4068.

- Gonzalez V., Tufeu R. and Subra P.. "High-pressure vapor-liquid equilibrium for the binary systems carbon dioxide+dimethyl sulfoxide and carbon dioxide+dichloromethane." *Journal of Chemical Engineering Data*, 47, (2002): 492-495.

- Gouin S. "Micro-encapsulation: industrial appraisal of existing technologies and trends." *Trends in Food Science & Technology*, 15, (2004): 330-347.

- Grandison A. S., Lewis M. J., *Separation Processes in the Food and Biotechnology Industries*, England: Woodhead Publishing Ltd., 1996.

- Lu G., Wang L., Wang R., Zeng Y. and Huang X. "Determination of Chitosan by Cathodic Stripping Voltammetry." *Analytical Science*, April 22, (2006): 575-578.

- Hertz A., Sarrade S., Guizard C., and Julbe A. "Synthesis and encapsulation of yttria stabilized zirconia particles in supercritical carbon dioxide." *Journal of the European Ceramic Society*, 26, (2006): 1195-1203.

- Jang M.-K. and Nah J.-W. "Characterization and modification of low molecular water-soluble chitosan for pharmaceutical application." *Bulletin of the Korean Chemical Society*, 24, no. 9, (2004): 1303-1307.

- Johnston, K. P. "Block copolymers as stabilizers in supercritical fluids." Current *Opinion in Colloid & Interface Science*, 5, (2000): 351-356.

- Johnston, K. P. and Eckert C. A. "An analytical Carnahan-Starling van der Waals model for solubility of hydrocarbons solids in supercritical fluids." *AIChE Journal*, 27, no. 5, (1981): 773-779.

- Jung J. and Perrut M. "Particle design using supercritical fluids: Literature and patent survey." *Journal of Supercritical Fluids*, 20, (2001): 179-219.

- Kerc J., Srcic S., Knez Z., Sencar-Bozic P. "Micronization of drugs using supercritical carbon dioxide." *International Journal of Pharmaceutics*, 182, no. 1, (1999): 33-39.

- Kim J.-H., Paxton T. E. and Tomasko D. L. “Microencapsulation of Naproxen Using Rapid Expansion of Supercritical Solutions.” *Biotechnology Progress*, 12, (1996): 650-661.

- Kobe Steel Ltd. (1993). Patent J05057166.

- Köping-Höggård M., Mel’nikova Y. S., Varum K. M., Lindman B. and Arthursson P.. “Relationship between the physical shape and efficiency of oligomeric chitosan as a gene delivery system in vitro and in vivo.” *Journal of Gene Medicine*, 5, (2003): 130-141.

- Kordikowski A., Schenk A. P., Van Nielen R. M. and Peters C. J. “Volume expansions and vapor-liquid equilibria of binary mixtures of a variety of polar solvents and certain near critical solvents.” *Journal of Supercritical Fluids*, 8, (1995): 205-216.

- Krause H., Niehaus M., Teipel U. (1998) Patent DE 19711393.

- Krukonis, V. J. and Kurnik R. T. “Solubility of the solid aromatic isomers in carbon dioxide.” *Journal of Chemical Engineering Data*, 30, no. 3, (1985): 247-249.

- Lamm M. H. and Hall C. K. “Molecular Simulation of Complete Phase Diagrams for Binary Mixtures.” *AIChE Journal,* 47, (2001): 1664-1675.

- Lele A. K. and Shine A. D. “Morphology of Polymers Precipitated from a Supercritical Solvent.” *AIChE Journal*, 38, no. 5, (1992): 742-752.

- Lele A. K., and Shine A. D. “Effect of RESS Dynamics on Polymer Morphology.” *Industrial & Engineering Chemistry Research*, 33, no. 6, (1994): 1476-1485.

- Liu D., Zhang J., Chen J., Li Z., Shen D. and Yang G. “Recovery of TiO_2 nanoparticles synthesized in reverse micelles by antisolvent CO_2.” *Colloids and Surfaces A: Physicochemical and Engineering Aspects*, 227, (2003): 45-48.

- Mansouri S., Lavigne P., Corsi K., Benderdour M., Beaumont E., Fernandez J. C.. “Chitosan-DNA nanoparticles as non-viral vectors in gene therapy: strategies to improve transfection efficacy.” *European Journal of Pharmaceutics and Biopharmaceutics*, 57, (2004): 1-8.

- Matson D. W., Fulton J. L., Peterson R. C., Smith R. D. “Rapid expansion of supercritical fluid solutions: Solution formation of powders, thin films, and fibers.” *Industrial & Engineering Chemistry Research*, 26, (1987): 2298-2306.

- Matsuyama K., Mishima K., Hayashi K.-I. and Matsuyama H. “Microencapsulation of TiO2 nanoparticles with polymer by rapid expansion of supercritical solution.” *Journal of Nanoparticle Research*, 5, (2003): 87-95.

- Matsuyama K., Mishima K., Hayashi K.-I., Ishikawa H., Matsuyama H., and Harada T. “Formation of Microcapsules of Medicines by the Rapid Expansion of a Supercritical Solution with a Nonsolvent.” *Journal of Applied Polymer Science*, 89, (2003): 742-752.

- Mawson S., Johnston K. P., Combes J. R., and DeSimone J. M., “Formation of Poly (1,1,2,2-Tetrahydroperfluorodecyl Acrylate) Submicron Fibers and Particles from Supercritical Carbon Dioxide Solutions.” *Macromolecules*, 28, no. 9, (1995): 3182-3191.

- McHugh M. A. and Gucke T. L. “Separating Polymer Solutions with Supercritical Fluids.” *Macromolecules*, 18, no. 4, (1985): 674-680.

- McHugh M. A., Seckner A. J. and Yogan T. J. “High Pressure Phase Behavior of Octcosane and Carbon Dioxide.” *Industrial Engineering Chemical Fundamentals*, 23, (1984): 493-499.

- McHugh M. A. and Krukonis V. J. *Supercritical Fluid Extraction Principles and Practice;* 2nd Ed., Boston: Butterworth-Heinemann, 1994.

- Middleton J. C. and Tipton A. J., “Synthetic biodegradable polymers as medical devices.” *Medical Plastic and Biomaterials Magazine*, March (1998). Available from http://www.devicelink.com/mpb/archive/98/03/002.html.

- Mishima K., Yamaguchi S. Umemoto H., (1996) Patent JP 8104830.

- Mishima K. (1999) Patent JP11197494.

- Mishima K., Mitani H. (1999) Patent JP11047681.

- Mishima K., Matsuyama K., Tanabe D., Yamauchi S., Young T. J. and Johnston K. P. “Microencapsulation of Proteins by Rapid Expansion of Supercritical Solution with a Nonsolvent.” *AIChE Journal*, 46, no. 4, (2000): 857-865.

- Modell M., Robey R. J., Krukonis V. J., de Filippi R. P. and Oestreich D. “Supercritical fluid regeneration of activated carbon.” *87th AIChE Meeting*, Boston, August (1979).

- Muzzarelli, R. A. A., *Natural Chelating Polymers: Alignic Acid, Chitin and Chitosan*. New York: Pergamon Press, 1973.

- O'Neill M. L., Cao Q., Fang M., Johnston K. P., Wilkinson S. P., Smith C. D., Kerschner J. L., and Jureller S. H, ''Solubility of Homopolymers and Copolymers in Carbon Dioxide.'' *Industrial & Engineering Chemistry Research*, 37, no. 8, (1998): 3067-3079.

- Onwulata, Charles. *Encapsulated and powdered foods*. Boca Raton: CRC Press Taylor & Francis Group, 2005.

- Parcell S. W. "Sulfur in human nutrition and applications in medicine." *Alternative Medicine Review*, 7, no. 1, (2002): 22-44.

- Patel, K. S, "Automatic Generation of Global Phase Equilibrium Diagram from Equation of State." *Doctoral Dissertation*, USF, (2008).

- Patel K. S. and Sunol A. K. "Automatic generation of global phase equilibrium diagram for binary systems from equation of state." *Computers and Chemical Engineering*, 33, (2009): 1793-1804.

- Perez de Diego Y., Wubbolts F. E., Witkamp G. J., de Loos T. W. and Jansens P. J. "Measurements of phase behavior of the system dextran-DMSO-CO2 at high pressures." *Journal of Supercritical Fluids*, 35, no. 1, (2005): 1-9.

- Perrut M. (2001) Patent WO2001049407.

- Pessey V., Cansell F., Chevalier B., Weill F., Etourneau J. (1999) Patent FR 9904175.

- Pessey V., Garriga R., Weill F., Chevalier B., Etourneau J. and Cansell F. "Core-Shell Materials Elaboration in Supercritical Mixture CO_2/Ethanol. *Industrial & Engineering Chemistry Research*, 39, (2000): 4714-4719.

- Polishuk I., Wisniak J., Segura H., Yelash L. V. and Kraska T. "Prediction of the Critical Locus in Binary Mixtures Using Equation of State. II. Investigation of van der Waals-Type and Carnahan-Starling-Type Equation of State." *Fluid Phase Equilibria,* 172, (2000):1-26.

- Rajasingam R., Lioe L., Pham Q. T. and Lucien F. P. "Solubility of carbon dioxide in dimethyl sulfoxide and N-methy-2-pyrrolidone at elevated pressure." *Journal of Supercritical Fluids*, 31, (2004): 227-234.

- Ratajska M., et al. "Studies on the biodegradation of chitosan in aqueous medium." *Fibres & Textiles in Eastern Europe*, 11, no. 3, (2003): 75-79.

- Reverchon E., Della Porta G., De Rosa I., Subra P. and Letourneur D. "Supercritical Antisolvent Micronization of Some Biopolymers." *Journal of Supercritical Fluids*, 18, (2000): 239-245.

- Reverchon E., Della Porta G., Pace S. and Di Trolio A. “Supercritical antisolvent precipitation of submicronic particles of superconductor precursors.” *Industrial & Engineering Chemistry Research*, 37, no. 3, (1998): 221-236, 952-958.

- Rizvi, S. S. H., *Supercritical Fluid Processing of Food and Biomaterials*, New York: Ed. Blackie Academy, 1994.

- Rout S. K. and Prinyawiwatkul W. “Determining degree of deacetylation and purity of crawfish chitin and chitosan using Fourier Transform Infrared (FTIR) spectroscopy.” *IFT Annual Meeting*, New Orleans, Louisiana 2001.

- Seckner A. J.; McClellan A. K. and McHugh M. A. “High-Pressure Solution Behavior of the Polystyrene-Toluene-Ethane System.” *AIChE Journal*, 34, (1988): 9-16.

- Shiho H. and DeSimone J. M. “Dispersion polymerization of acrylonitrile in supercritical carbon dioxide.” *Macromolecules*, 33, (2000): 1565-1569.

- Shine A., Gelb J. (1997) Patent WO 98/15348.

- Siokonkowska A., Wisniewski M., Skopinska J., Kennedy C. J., and Wess T. J. “The photochemical stability of collagen-chitosan blends.” *Journal of Photochemistry and Photobiology A: Chemistry*, 162, (2004): 545-554.

- Smeltzer B., “ The solubility of Triton X-114 and Tergitol 15-S-9 in high pressure carbon dioxide solutions,” *Master Thesis*, University of South Florida, 2005.

- Smith J., Wood E. and Dornish M. “Effect of chitosan on epithelial cell tight junctions.” *Pharmaceutical Research*, 21, no. 1, (2004): 43-49.

- Spencer C. F. and Danner R. P. “Improved equation for prediction of saturated liquid density.” *Journal of Chemical and Engineering Data*, 17, (1972): 236-241.

- Subramanian B., Said S., Rajewski R. A., Stella V. (1997) Patent WO 97/31691.

- Subramanian B., Said S., Rajewski R. A., Stella V. (1998) Patent US5833891.

- Sun Y.-P. and Rollins H. W. “Preparation of polymer-protected semiconductor nanoparticles through the rapid expansion of supercritical fluid solution.” *Chemical Physics Letters*, 288, (1998): 585-588.

- Sunol A. K. (1997) Patent US 0062332.

- Sunol A. K., Sunol S. G. *Handbook of Solvents*. Toronto, Canada: ChemTec Publishing, 2001. (ISBN 1-895198-24-0):1419-1449.

- Sunol A. K., Kosky J. P., Murphy M., Hansen E., Jones J., Mierau B. and Sunol S. "Supercritical Fluid Aided Encapsulation of Particles in a Fluidized Bed Environment." *Proceedings of the 5th Meeting on Supercritical Fluids*, TOME 1, ISASF, (1998).

- Tan C. S and Liou D. C. "Desorption for ethyl acetate from activated carbon by supercritical carbon dioxide." *Industrial & Engineering Chemistry Research*, 27, no. 6, (1988): 988-991.

- Tan C. S and Liou D. C. "Regeneration of activated carbon loaded with toluene by supercritical carbon dioxide." *Separation Science and Technology*, 294, no. 1, (1989a):111-127.

- Tan C. S and Liou D. C. "Adsorption equilibrium of toluene from supercritical carbon dioxide on activated carbon." *Industrial & Engineering Chemistry Research*, 29, no. 7, (1990a): 1412-1415.

- Thies C., Dos Santos Ribeiro I., Richard J., Vandevelde V., Rolland H. and Benoit J. P. "A supercritical fluid-based coating technology 1: Process considerations." *Journal of Microencapsulation*, 20, no. 1, (2003): 87-96.

- Tom J. W., Debenedetti P. G. "Formation of bioerodible polymeric microspheres and microparticles by rapid expansion of supercritical solutions." *Biotechnology Progress*, 7, no. 5, (1991): 403-411.

- Tom J. W., Debenedetti P. G. and Jerome R. "Precipitation of Poly L-Lactic Acid and Composite Poly L-Lactic Acid.-Pyrene Particles by Rapid Expansion of Supercritical Solutions." *Journal of Supercritical Fluids*, 7, no. 1, (1994): 9-29.

- Tsutsumi A., Ikeda M., Chen W., and Iwatsuki J. "A nano-coating process by the rapid expansion of supercritical suspensions in impinging-stream reactors." *Powder Technology*, 138, (2003): 211-215.

- Tsutsumi A., Nakamoto S., Mineo T. and Yoshida K. "A novel fluidized-bed coating of fine particles by rapid expansion of supercritical fluid solutions." *Powder Technology*, 85, no. 3, (1995): 275-278.

- Van Konynenburg P. H. and Scott R. L. "Critical Lines and Phase Equilibria inVan Der Waals Mixtures." *Philosophical Transactions of the Royal Society of London. Series A, Mathematical and Physical Sciences*, 298, (1980): 495-540.

- Vitzthum O. and Hubert P., German Patent 2357590, 1975; US Patent 3879569, 1975.

- Wang T.-J., Tsutsumi A., Hasegawa H. and Mineo T. “Mechanism of particle coating granulation with RESS process in a fluidized bed.” *Powder Technology*, 118, no. 3, (2001): 229-235.

- Wang Y., Wei D., Dave R., Pfeffer R., Sauceau M., Letourneau J.-J. and Fages J. “Extraction and precipitation particle coating using supercritical CO_2.” *Powder Technology*, 127, (2002): 32-44.

- Wang Y., Dave R. N. and Pfeffer R. “Polymer coating/encapsulation of nanoparticles using a supercritical anti-solvent process.” *Journal of Supercritical Fluids*, 28, (2004): 85-99.

- Wang Y., Pfeffer R. and Dave R. (2004) Patent WO2004091571.

- Wang Y., Pfeffer R. and Dave R. “Polymer Encapsulation of Fine Particles by a Supercritical Antisolvent Process.” *AIChE Journal*, 51, no. 2, (2005): 440-455.

- Wang W., Griffiths R. M. T., Naylor A., Giles M. R., Irvine D. J. and Howdle S. M. “Preparation of cross-linked microparticles of poly(glycidyl methacrylate) by dispersion polymerization of glycidyl methacrylate using PDMS macromonomer as stabilizer in supercritical carbon dioxide.” *Polymer*, 43, (2002): 6653-6659.

- Yelash L. V. and Kraska T. “The Global Phase Behaviour of Binary Mixtures of Chain Molecules: Theory and Application.” *Physical Chemistry Chemical Physics*, 1, (1999): 4315- 4322.

- Yeo S. D., Lim G. B., Debenedetti P. G. and Bernstein H. “Formation of microparticulate protein powders using a supercritical fluid antisolvent.” *Biotechnology and Bioengineering*, 41, (1993): 341-346.

- Yeo S. D., Debenedetti P. G., Radosz M. and Schmidt H. M. “Supercritical antisolvent process for substituted para-linked aromatic polyamides: phase equilibrium and morphology study.” *Macromolecules*, 26, (1993): 6207-6210.

- Young T. J., Johnston K. P., Mishima K. and Tanaka H. “Encapsulation of Lysozyme in a Biodegradable Polymer by Precipitation with a Vapor-over-Liquid Antisolvent.” *Journal of Pharmaceutical Sciences*, 88, no. 6, (1999): 640-650.

- Zhou Y.-G., Yang Y.-D., Guo X.-M. and Chen G.-R. “Effect of molecular weight and degree of deacetylation of chitosan on urea adsorption properties of copper chitosan.” *Journal of Applied Polymer Science*, 89, (2003): 1520-1523.

APPENDICES

Appendix A. Supercritical Encapsulation Techniques Literature

Reference	**Process**	**Particle Size (µm)**	**Coating Solubility**	**Core Solubility**	**Comments**
Bleich J., 1996	ASES	<50	No	No	- $SCCO_2$ - Core particles: hyoscine butylbromide, indomethacin, piroxican and thymopentin. - Coating material: PLA. - Particle size: 10-90 µm.
Chapttopadhyay P., 2005	SFEE	0.2-1	No	No	- $SCCO_2$ - Core particles: indomethacin and ketoprofen. - Coating material: Eudagrid and PLA. - Continuous and batch process by supercritical carbon dioxide extraction of oil in water (o/w) emulsions. - Final particle size 200 and 1000 nm.
Elva1ssore Nicola, 2001	SAS	0.5-2	No	No	- $SCCO_2$ - Core particles: insulin. - Coating material: PLA - Cosolvents: DCM, DMSO. - Particle size: 0.5 to 2 µm.
Falk Rick, 1997	PCA	0.2-1	No	No	- $SCCO_2$ - Core particles: Gentamycin, naloxone, and naltrexone. - Coating material: PLA. - Hydrophobic ion pairing (HIP) technique was used. - Particle size: 0.2-1.0µm.
Glebov Evgeni M., 2001	RESS	20	Yes	No	- $SCCO_2$ - Core particles: Al, Mg powders (20 µm). - Coating material: poly(vinylidene fluoride) and poly(4-vinylbiphenyl) (PVB) were used. - Average thicknesses of the films deposited on metal powders were in the range of 1-30 nm.

Appendix A (Continued)

Reference	**Process**	**Particle Size (µm)**	**Coating Solubility**	**Core Solubility**	**Comments**
Hertz Audrey, 2006	RESS, Polymerization	0.03-0.3	Yes	No	- SCCO$_2$ - The core material: YSZ particles. - Coating material MMA and PMMA. - PDMS-g-PA was used as surfactant.
Kim Jong-Hyun, 1996	RESS	10-90	Yes	Yes	- SCCO$_2$ - Core particles: naproxen. - Coating material: poly-(L-lactic acid) (L-PLA). - Particle size: 10-90 µm. - Agglomeration was constant in almost all the experiments.
Kröber H, 2005	RESS	7.39-124.6	Yes	No	- SCCO$_2$. - Glass beads were coated with stearyl alcohol. - Smooth coating, thickness 1-8 µm. - Coated particle size range is 70-125 µm.
Matsuyama Kiyoshi, 2003	RESS-N	14.6	Yes	No	- SCCO$_2$ - Core material: *p*-acetamidophenol, acetylsalicylic acid, 1,3-dimethylxanthine, flavone, and 3-hydroxyflavone. - Coating material PEG, PMMA, PLA, PGLA and PPG-PEG.
Mishima Kenji, 2000	RESS-N	6-62	Yes	No	- SCCO$_2$ - Core material: lysozyme (24 µm) and lipase (19 µm). - Coating material PEG, PMMA, PLA, PGLA and PPG-PEG.
Pessey V., 2000	SCF- Reaction	2-3	Yes	No	- SCCO$_2$ - Core particles: Ni (3 µm) and SmCo$_5$ (10µm) - Coating: Cu - The thickness on Ni gave values from 0.2 to 1 µm.

Appendix A (Continued)

Reference	**Process**	**Particle Size (µm)**	**Coating Solubility**	**Core Solubility**	**Comments**
Ribeiro Dos Santos, 2002	Gradual P-T drop	125-500	Yes	No	- SCCO$_2$. - BSA microparticles coated with Gelucire 50/02 or Dynasan 114. - Dynasan 114 crystallizes, was not a good coating. - Coating was not perfectly uniform. - Coated particle size range is 543 µm.
Sun Ya-Ping, 1998	RESS	0.0033	Yes	No	- SCNH$_3$ - Core particles: cadmium sulfide (33 Å) - Coating material: Poly(*N*-vinyl-2-pyrrolidone).
Sunol A.K, 1998	T antisolvent	30-500	Yes	No	- SCCO$_2$ - Core particles: sodium chloride (30-500 µm) and ammonium nitrate. - Coating material: HTPB. - Film thicknesses as low as 0.2 micron.
Thies C., 2003	Gradual P-T drop	500	Yes	No	- SCCO$_2$. - BSA crystals and sugar spheres as core particles coated with Gelucire 50/02 and Trimyristin. - Trimyristin crystallizes, was not a good coating. - Insoluble biomolecules less prone to denaturizing in process like this. - Coated particle size range is 500 µm.
Tsutsumi Atsushi, 1995	RESS	55.6	Yes	No	- SCCO$_2$. - Spherical catalyst particles were coated with paraffin. - Average particle size 56 µm. - Coating thickness below 0.5µm.

Appendix A (Continued)

Reference	**Process**	**Particle Size (µm)**	**Coating Solubility**	**Core Solubility**	**Comments**
Tsutsumi Atsushi, 2003	RESS, Impinging	0.02-1	Yes	No	- $SCCO_2$ - Core particles: silica particles (1µm) and titanium dioxide (20 nm) were used. - Coating material was paraffin. - Thickness of the paraffin layer was around 50–60 nm.
Wang Ting-Jie, 2001	RESS	130	Yes	No	- $SCCO_2$, paraffin was used as a binder. - Fine particles of SiO_2 (*d*= 1µm) as coating material and glass beads as core particle (*d*=130 µm).
Wang Yulu, 2002	RESS	315-500	Yes	No	- $SCCO_2$. - PVCVA and HPC were used as coating. - The host particles were glass beads, 315 and 500 µm. - The average coating thickness was about 0.8 µm, some agglomeration and uneven coating was observed.
Wang Yulu, 2004	SAS	0.016, 0.020, 0.6	No	No	- $SCCO_2$ - Core particles: silica nanoparticles (hydrophobic and hydrophilic). - Coating material: Eudragit. - Coated particle: 600 nm. - Coating thickness: 75 nm.
Wang Yulu, 2005	SAS	0.5	No	No	- $SCCO_2$ - Core particles: silica particles (0.5 µm) - Coating material: PLGA.
Young Timothy J., 1999	PCA	5-70	No	No	- $SCCO_2$ - Core particles: Lysozyme (1-10 µm). - Coating material was *l*-PLA or PGLA. - Particle size: 5- 70 µm.

Appendix A (Continued)

Reference	**Process**	**Particle Size (µm)**	**Coating Solubility**	**Core Solubility**	**Comments**
Yuea Baohua, 2004	Dispersion polymerization	12	Yes	No	- SC CO_2. - DCR particles were encapsulated with PMMA and PVP. - Useful when a monomer can be used as a cosolvent. - Valuable to make small particles, 12 µm. - Minor particle agglomeration.

BSA: Bovine serum albumin
CdS: cadmium sulfide
CF3COCH=C(O)-CF$_3$]$_2$Cu: bis-(hexafluoroacetylacetonate)copper(II)
L-PLA: Poly-L-lactide
PEG: Poly(ethylene glycol)
PDMS-g-PA: poly(dimethylsiloxane)-grafted-polyacrylate
PMMA: Poly(methyl methacrylate)
PPG:Poly(propylene glycol)
PS: Poly(styrene)
PVB: poly(4-vinylbiphenyl)
PVDF: poly(vinylidene fluoride)
SmCo$_5$: Samarium cobalt

Appendix B. Supercritical Encapsulation Patents Literature

Author	Patent #	Method
Akihisa N., Eiichi U., Chiaki N. (2005)	JP 2005232053	Formulation of liposome-charged particles with a lipid film using $SCCO_2$ in a RESS process.
Benoit J. P., Richard J., Thies C. (1996)	FR 2753639 WO 96/13136	A suspension of the active substance and a polar polymer in an organic solvent were precipitated with $SCCO_2$ using a SAS process.
Benoit J. P. , Rolland H., Thies C., Van de Velde V. (1996)	EP 0706821 WO 96/11055	Particles were coated in a stirred vessel by precipitating the dissolved coating with T and P changes.
Benoit J. P. , Rolland H., Thies C., Van de Velde V. (2000)	US 6087003	Solid particles were coated by using $SCCO_2$ and a coated material dissolved thereon. The pressure or temperature of the system is adjusted in such a way as to cause controlled precipitation of the coating material.
Brunner G. and Werther J. (2006)	EP 1731219	Process for encapsulating organic substances in particle form by spraying an inert supercritical carrier gas together with the coating material into a high pressure fluidized bed contained in an autoclave.
Buerger A., Raschck T., Voigt N., Schwanke F. (2003)	WO 03075881	Coating method for cosmetic application using a wax coating in a SCF fluidized bed.
Cunningham M. F., Mahabadi H. K. (1996)	US 5514514	Preparation of carrier powder polymer coatings which includes the supercritical polymerization of a monomer and surfactant in a SCF to form a porous polymer, after which a second polymer is incorporated.
Dalian Medicine Institute (1998)	CN 1221607	Lipoplast particles were coated with liposoluble medicines in a $SCCO_2$ environment by the increase of T and decrease of P.
Kobe Steel Ltd. (1993)	J 05057166	RESS process where core, coating material and $SCCO_2$ form a homogeneous system.
Krause H., Niehaus M., Teipel U. (1998)	DE 19711393	Coated 100µm particle with a coating agent dissolved in $SCCO_2$ using RESS in a fluidized bed.
Mishima K. (1999)	JP 11197494	Production of organic-inorganic microcapsules using $SCCO_2$ RESS process.
Mishima K., Yamaguchi S. Umemoto H., (1996)	JP 8104830	Patented the formation of micro-spheres by spraying a suspension of flavonoids in a supercritical solution of the polymer and a cosolvent at atmospheric pressure.

Appendix B (Continued)

Author	Patent #	Method
Mishima K., Mitani H. (1999)	JP11047681	Inorganic particles were coated with PEG using $SCCO_2$ in a RESS process, where the core and coating materials were solubilized in the SCF by using a cosolvent.
Mishima K., Matsuyama K. (2006)	KR 20060125871	A method for producing fine particles using rapid expansion into poor solvent from supercritical fluid.
Perrut M. (2001)	WO2001049407	Method for collecting and particles encapsulation using a coating agent and particles dispersed in a SCF by RESS.
Pessey V., Cansell F., Chevalier B., Weill F., Etourneau J. (1999)	FR 9904175	Coating of metallic particles was obtained by thermal decomposition of the coating material in a high pressure cell.
Shine A., Gelb J. (1997)	WO 98/15348	Microencapsulation of a core material by swelling a polymer coating with a SCF, followed by a RESS process.
Subramanian B., Said S., Rajewski R. A., Stella V. (1997)	WO 97/31691	An ASES process was patented where a solution with the coating agent was sprayed over the fluidized core particles.
Subramanian B., Saim S., Rajejewski R. A., Stella V. (1998)	US5833891	Method for particle precipitation and subsequence coating using a SCF with an antisolvent technique.
Sunol A. K. (1997)	US 0062332	Using a temperature swing, the polymer coating was precipitated over the insoluble particle core.
Wang Y., Pfeffer R., Dave R. (2004)	WO2004091571	Preparation of coated nanoparticles with $SCCO_2$ antisolvent method.
Wang Y., Pfeffer R., Dave R. (2009)	US 7537803	Polymer coating/encapsulation using supercritical antisolvent process.
Yunquing K., Guangfu Y., Yandong Y.' Zhongbing H.' Xiaoming L. (2008)	EP 1731219	Preparation of praclitaxel carried medicine sustained-release microsphere by supercritical fluid technique.

Appendix C. Operating the Phase Analyzer

1. Start Up

    a) Turn on syringe pump cooler.

    b) Let the cooler temperature reach at least –3°C before beginning experiments.

    c) Turn on syringe pump controller.

    d) Turn on syringe pump.

    e) Open the valve on the CO_2 tank.

    f) Open the inlet valves into the syringe pump and check that the outlet valves (syringe pump) are closed.

    g) Press REFILL on the syringe pump controller to fill the syringe pump, select pump A or B, flow rate no higher than 5 ml/min.

    h) When the syringe pump is full, press STOP on the syringe pump controller, then press pump A or B (depending on which pump you are working with).

    i) Close the inlet valves on the syringe pump.

    j) Turn on the TV and put in a video for recording purposes.

    k) Turn on the phase analyzer controller.

    l) Turn on the magnetic stirrer on the phase analyzer.

    m) Press the Video Input Button on the phase analyzer controller to get video feed into the TV.

    n) To make a temperature set point for experiment runs, press the down arrow on the phase analyzer controller to SPM Settings.

    o) Once blinker is on SPM Settings press the Enter Button.

    p) Enter the temperature at which you want to run experiments.

q) Press the Enter Button and then press the Escape Button to return to the main menu of the phase analyzer controller.

r) To enter sample numbers, go to Sample on the phase analyzer, then enter sample numbers. Press the Enter Button, then input whatever sample number you want.

s) Press the Enter Button after designating a sample number for your experiment.

2. Running Experiments

a) Weigh solid sample and record the mass, or measure out liquid sample and record the volume.

b) Unscrew the magnetic stirrer from the phase analyzer.

c) Put liquid/solid sample into the solubility cell.

d) Put the magnetic stirrer back on the phase analyzer and tighten it.

e) Make sure the outlet valve on the phase analyzer is closed.

f) Open the outlet valves on the syringe pump.

g) On the syringe pump controller, press RUN. Make sure the flow rate is 1 ml/min.

h) Open the inlet valve of the phase analyzer slowly to let CO_2 into the solubility cell until a pressure of 5-7 bar is reached, then close the inlet valve of the phase analyzer and open the outlet valve slowly to release the air trapped in the cell. Repeat this process 10 times, and check that the cell outlet valve remains closed after every purge.

i) After the air purging is done, stop the syringe pump and take notes about the pressure and volume at the syringe pump controller.

j) Now press RUN on the syringe pump controller and open the cell inlet valve to fill up the cell with CO_2. Recommended flow rate is 1-3 ml/min. volume with the manual pump (this will take a few minutes depending on the pressure required).

k) The temperature recommended to fill up the cell is room temperature. Once the cell is full, the temperature can be adjusted.

l) Once the required pressure is reached, press STOP on the syringe pump controller. Close both outlet valves to syringe pump and close the phase analyzer inlet valve.

m) Stop the syringe pump flow rate – close both outlet valves to syringe pump.

n) Record the final pressure and temperature at the syringe pump controller (this data is needed to calculate the amount of CO_2 used in the experiment).

o) Adjust temperature (START UP procedure *n* to *q*) and press the HEAT ON button on the phase analyzer controller to bring the cell up to the experiment temperature.

p) Adjust volume by turning the manual pump.

q) Once the operation conditions for the experiment are reached, unlock the hinge on the phase analyzer and shift the phase analyzer until it is horizontal or slightly past horizontal to get some sample in the camera's view cell. If the sample is a solid you should see some solid in the window. If the sample is liquid a liquid-liquid interface should be visible in cell window.

r) Wait at least 3h for the system to stabilize.

s) Record the pressure on the phase analyzer and the manual pump as well as the temperature.

t) Watch the sample while increasing the pressure to determine if it has dissolved into the CO_2.

u) Once no solid or no liquid-liquid interface is detected (turn on the magnetic stirrer for a few seconds to make sure). Record this pressure on the phase analyzer, the manual pump gauge, and the volume of the cell.

v) If more than one phase is observed, increase the pressure by turning the manual pump to the right.

w) Watch the sample while increasing the pressure to determine if it has dissolved into the CO_2.

x) Decrease the pressure drastically by turning the manual pump to the left until a cloud point is observed.

y) Record this pressure on the phase analyzer, the manual pump gauge, and the volume of the cell.

z) Continue increasing and decreasing the pressure as described above for precision purposes to get 5 points to average out for calculations. Record pressures and volumes properly. (It might also be wise to indicate 1 phase or 2 phases for each pressure and volume as well).

aa) Change the temperature, let the system stabilize and re-run the experiment at the new operation conditions.

3. Clean Up

Once the experiment is done and data is gathered, the system needs to be cleaned before any other experiment can be run.

a) Stop recording the experiment.
b) Press the Heat-Off Button on phase analyzer controller. Let the cell cool to room temperature. It will take a while for the cell to return to room temperature, depending on the experiment temperature used.
c) Unlock pivot and put cell into upright position.
d) Open the phase analyzer outlet valve slowly to vent the pressure. Opening the outlet valve too fast will result in clogging the outlet valve.
e) Unplug the magnetic stirrer and carefully unscrew the cap (the cell may still be pressurized even if phase analyzer controller says 0 bar).
f) Collect the remaining sample inside the cell.
g) Disconnect and remove the lamp, camera, thermocouples, inlet and outlet valves, and the pressure gauge on the phase analyzer.
h) Carefully unscrew the solubility cell from the phase analyzer (do not twist the heaters' wires connected to the cell).
i) Clean the cell using an appropriate solvent and a q-tip, so as not to scratch the wall's surface.
j) Remove O-rings from the bottom of the solubility cell and wash them thoroughly with the appropriate solvent.

k) Remove frit from phase analyzer or the solubility cell carefully (depending on which frit you use – fixed frit is in the cell, the movable frit is screwed onto the piston) and rinse thoroughly with the solvent.

l) Clean out the inlet and outlet valves of the phase analyzer with the solvent.

m) Wash the magnetic stirrer with the solvent.

n) Clean each component with compressed nitrogen as well (this aids in removing very fine solid particles).

o) Reassemble the system and refill the phase analyzer with pure CO_2 or the mix solvent- CO_2.

p) Proceed to run the system at the same operation conditions (pressure and temperature) of the experiment in order to dissolve any remaining solute.

q) This cleaning procedure should be done as many times as needed, until no solute (liquid or solid) stays inside the phase analyzer.

4. Shut Down

Once the cleaning process is done, follow the instructions to shut down the system.

a) Press the Heat-Off Button on phase analyzer controller. Let the cell cool to room temperature.

b) Open the phase analyzer outlet valve slowly to vent the pressure.

c) Open the syringe pump outlet valves to vent the remaining CO_2 through the phase analyzer.

- d) Turn off the syringe pump.
- e) Turn off the syringe pump controller.
- f) Turn off the cooler.
- g) Return the manual pump displacement to zero.
- h) Turn off the TV.

5. Reassembly
   - a) Put frit back into place (into the solubility cell or onto the piston, depending on which one you use).
   - b) Put both O-rings back into place on the bottom of the solubility cell.
   - c) Carefully tighten the solubility cell back onto the phase analyzer.
   - d) Install and connect the lamp, camera, thermocouples, inlet and outlet valves, and pressure gauge on the phase analyzer.
   - e) Carefully screw magnetic stirrer cap back on top of the phase analyzer.

Appendix D. Operating the Dynamic Solubility Set-Up

1. Glassware Pre-Treatment
    a) Prepare a 5% solution of HMDS in dichloromethane (DCM).
    b) Fill the glassware and soak the glass wool with this solution.
    c) Put on the oven at 250°C for 1 hr.
    d) Wait for cool down, pass some DCM and let it dry.

2. Start Up
    a) Turn on the syringe pump cooler (Lauda Ecoline RE120), the immersion circulator (Model 7300, Fisher) at the water bath and the heating tape over the back pressure regulator.
    b) Let the cooler temperature reach at least –3°C before beginning experiments.
    c) Turn on syringe pump controller.
    d) Turn on syringe pump.
    e) Open the valve on the CO_2 tank.
    f) Open the inlet valves into the syringe pump and check that the outlet valves (syringe pump) are closed.
    g) Press REFILL on the syringe pump controller to fill the syringe pump, select pump A or B, flow rate no higher than 5 ml/min.
    h) When the syringe pump is full, press STOP on the syringe pump controller, then press pump A or B (depending on which pump you are working with).
    i) Close the inlet valves on the syringe pump.

3. Running Experiment

   a) Weigh solid sample and record the mass.
   b) Weigh the extraction cell by itself.
   c) Prepare the cell as follows: first place a piece of stainless steel mesh at the bottom of the cell, then put in a layer of the treated glass wool, followed by the weighted solute. Before closing the cell, place at the closing top of it the metallic mesh and then another glass wool layer. The cell should be tight over the wise to assure a tight fit.
   d) Weigh the loaded cell.
   e) Place the extraction cell in the system.
   f) Set the working pressure on the BPR using the nitrogen tank.
   g) Open the outlet valves on the syringe pump.
   h) Check for leaks through all the system.
   i) Set the set-up to run through the bypass line until the operation conditions are reached (T and P).
   j) On the syringe pump controller, press RUN and wait until the required pressure is reached (100-120 bar). Make sure the flow rate is 1 ml/min.
   k) Turn on the HPLC pump.
   l) Press the DIRECT button.
   m) Select the appropriate component line (A, B, C or D) and fix the flow rate at the HPLC pump. Press ENTER.

n) Run the pumps for 2 to 3 h until the conditions (T and P) are stable. The supercritical mix will be passing through the bypass section until the system reaches the equilibrium.

o) Switch the supercritical mix to the extraction cell.

p) Set the collection vessel with a measured volume of DI water.

q) Register P and T at the system.

r) Start the Wet Test Meter.

s) Register the volume, pressure and temperature in the ISCO pump.

t) Collect samples for a period of 4 h.

u) Stop both pumps after the collection period.

v) Register P, T and volume in the ISCO pump.

w) Register total CO_2 volume and T in the Wet Test Meter.

4. Clean Up

a) Change the collection vessel.

b) Switch the flow through the bypass section.

c) Run the HPLC pump for 1 h (1ml/min), and then stop it.

d) Run the ISCO pump for 2 h with a flow rate higher than the one used for the extraction process (5 ml/min).

e) After one hour switch back the CO_2 flow to the extraction cell in order to eliminate residual DMSO.

f) Open the cell and remove the glass wool and metallic mesh from both ends.

   g) Clean the cell with water, followed by alcohol.

   h) Use nitrogen to dry the cell.

5. Shut Down

   a) Stop the ISCO pump.

   b) Turn off the water heater and let the system cool down.

   c) Release the system's pressure.

   d) Turn off the pump's chiller.

   e) Turn off the pumps.

   f) Unscrew the extraction cell carefully and let it dry completely.

   g) Weigh the dry cell.

6. Reassembly

   a) Change the Teflon tape in all the cell connections.

   b) Check that the cell is clean and completely dry.

   c) Put together the extraction cell following the same procedure (a, b, c and d) explained in the Running Experiment section.

Appendix E. Operating the Encapsulation Set-Up

1. Start Up
   a) Turn on the pump chiller, the heater at the insulation box and the heating tape over the back pressure regulator (BPR).
   b) Set the pressure at the back pressure regulator.
   c) Turn on the camera and the light inside the insulation box.
   d) Let the chiller temperature reach at least 0^oC before starting the pump.
   e) Turn on the continuous pump.
   f) Check that the outlet valve of the pump is closed.
   g) Open the valve on the CO_2 tank.
   h) Press F2 on the pump controller, select E (flow) and then input the flow rate (usually start with 4g/min). Increase the flow rate by pressing F2 and then E, set desired flow rate, ENTER; use 5g/min increments until the operation condition is reached.
   i) Very slowly, open the outlet valve on the high pressure pump.
   j) Turn on the heating tape over the coating cell.
   k) Check for leaks, and wait until the operation conditions are reached and the particles to be coated are fluidizing inside the cell.

2. Running Experiment
   a) Weigh solid to be coated and record the mass.
   b) Load the coating cell with the solid sample.

c) Place the coating cell in the system.

d) Follow the START UP procedure.

e) Turn on the WTM. Using a stop watch, start the time and the WTM simultaneously.

f) Turn on the HPLC pump.

g) Press the DIRECT button.

h) Select the appropriate component line (A, B, C or D) and fix the flowrate at the HPLC pump. Press ENTER.

i) Open the outlet valve of the HPLC pump, when the pressure in the HPLC controller slightly exceeds the pressure in the coating system.

j) Run the HPLC pump for 10 to 20 min (depending on the coating required).

k) Close the outlet valve on the HPLC pump. Change the flow rate to zero, and then press ENTER to stop the coating mix flow.

l) Set the collection vessel with a measured volume of DI water.

m) Register P and T at the system.

n) Register the flow rate and pressure in the continuous pump.

o) Collect water samples every hour and take it to the UV, until all the DMSO is extracted from the coating cell.

p) Stop pumping CO_2 after the collection period.

q) Register total CO_2 volume and T in the Wet Test Meter.

r) Register T1 (cell inlet temperature), T2 (cell outlet temperature) and T4 (box temperature).

3. Clean Up

After stopping the CO_2 pump continue with the cleaning procedure.

a) Turn off the heater at the insulation box and the heating tape of the coating cell.

b) Release the pressure of the system using the BPR until atmospheric pressure is reached.

c) Separate the coating cell from the CO_2 line and the coating line.

d) Run the HPLC pump with DMSO for twenty minutes using a flow rate of 5 ml/min through the coating line, to dissolve remaining polymer and avoid clogging.

e) Open the cell and remove the coated material and put into the desiccator.

f) Clean the cell with a dry cloth, and then use nitrogen to blow away the remaining powder.

4. Shut Down

a) Turn off the pump chiller, the heating tape over the BPR, the camera and the TV monitor.

b) Close the valves of the CO_2 and N_2 tanks.

c) Check that all the manometers or pressure indicators show atmospheric pressure, and then turn off both pumps.

5. Reassembly

   a) Prepare the coating vessel as follows: put the central chamber over one of the side windows-cover set, load the cell with the weighted core material, place the other window and cover over the central chamber. Using a torque wrench, tighten nuts in 5 ft.lb increments following the tightening sequence in Figure E.1, until the torque value of 30ft.lb is reached.

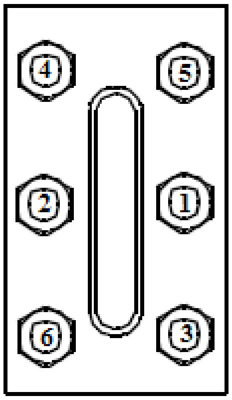

Figure E.1. Nut Tightening Sequence.

   b) Set the loaded coating cell inside the insulation box.
   c) Tighten the ¼ inlet and outlet CO_2 connections of the cell to the CO_2 line.
   d) Tighten the 1/16 inlet coating connection of the cell to the HPLC line.

Appendix F. Fluidization Calculations

Using the correlation established for Wen and Yu in 1966 for $0.001 < Re < 4000$, the minimum fluidization velocity was calculated:

$$Re = \frac{u_{mf} \cdot d_p \cdot \rho_{CO_2}}{\mu_{CO_2}} = \left[(33.7)^2 + 0.0408 \frac{d_p^3 \cdot \rho_{CO_2} \cdot (\rho_{CaO} - \rho_{CO_2}) g}{\mu_{CO_2}^2} \right]^{0.5} - 33.7 \qquad (1)$$

As an example for the calculations, the operation conditions considered were P=100 bar and T = 320 °K. At these conditions from the IUPAC table, the molar volume for carbon dioxide is 97.919 cm^3/mol, and the viscosity is 3.26 K/m·s. As the molecular weight of the carbon dioxide was 44, the density at the base operation conditions was 449.35 Kg/m^3.

As was presented in Chapter 4 in Table 4.6, the density of the calcium oxide was 3300Kg/m^3, for the calculations presented next, the size particle considered was 5 micron or 5×10^{-6} m.

Using equation 1, the Reynolds number obtained was 0.001, then solving for the minimum fluidization velocity, u_{mf}:

$$u_{mf} = \frac{Re \cdot \mu_{CO_2}}{d_p \cdot \rho_{CO_2}} \qquad (2)$$

The minimum fluidization velocity obtained was 1.3×10^{-5} m/s. The CO_2 pump input data units were grams/minute (g/min), then using the inlet transversal area on the encapsulation cell and the density of the CO_2 at the conditions inside the pump the required flow was calculated.

$$A = 2.65x10^{-4}\ m^2$$

$$\dot{V}_{mf} = A \cdot u_{mf} = 2.65x10^{-4}\ m^2 \cdot 1.3x10^{-5}\ m/s = 3.44x10^{-9}\ m^3/s$$

$$\rho_{CO_2} = 989.1 Kg/m^3 \quad (100bar, 270^{\circ}K)$$

$$\dot{M}_{mf} = 3.44x10^{-9}\ \frac{m^3}{s} \cdot 989.1 \frac{Kg}{m^3} \cdot \frac{1000g}{1Kg} \cdot \frac{60s}{1min} = 0.2 \frac{g}{min}$$

Next, the minimum mass fluidization mass flow ($\dot{M}_{mf}$) was obtained from u_{mf}, which is known as the minimum fluidization velocity. This is also sometimes referred to as the velocity at incipient fluidization ("incipient" means "about to begin"). After this, the flow rate was limited on one side by u_{mf} (minimum flow) and on the other side by the terminal (u_t) or free fall velocity of the particles (maximum flow).

$$u_t = \left[\frac{4 \cdot g \cdot d_p \left(\rho_{CaO} - \rho_{CO_2} \right)}{3 \rho_{CO_2} \cdot C_d} \right] \tag{3}$$

$$C_{d,spherical} = \frac{24}{Re_p} \quad \text{for} \quad Re_p < 0.4 \tag{4}$$

$$C_{d,spherical} = \frac{10}{Re_p^{1/2}} \quad \text{for} \quad 0.4 < Re_p < 500 \tag{5}$$

Replacing these values of the drag coefficient C_d in equation 3 the following expressions were obtained:

$$u_{t,spherical} = \frac{g \left(\rho_{CaO} - \rho_{CO_2} \right) d_p^2}{18 \cdot \mu_{CO_2}} \quad \text{for} \quad Re_p < 0.4 \tag{6}$$

$$u_{t,spherical} = \left[\frac{4}{225} \frac{\left(\rho_{CaO} - \rho_{CO_2} \right) \cdot g^2}{\rho_{CO_2} \cdot \mu_{CO_2}} \right]^{1/3} \cdot d_p \quad \text{for} \quad 0.4 < Re_p < 500 \tag{7}$$

For the Reynolds number of 0.001, the terminal velocity was calculated with equation 6, and the value obtained was 6.36x10^{-4} m/s. Following the same procedure explained previously to calculate the volumetric flow and mass flow, the results obtained were:

$$\dot{V}_t = 1.69 x 10^{-7}\ m^3/s$$
$$\dot{M}_t = 10\, g/min$$

The same calculations were done for the TiO_2, but in this case the value of density of the calcium oxide of 3300Kg/m^3 was substituted by the density of titanium dioxide of 4200 Kg/m^3.

Assuming spherical particles for an average pressure of 100 bar, the values obtained are shown in Tables F.1 and F.2.

Table F.1. Flow Required to Fluidize CaO 2µm and 5µm Particles.

T (°C)	$\dot{M}_{mf}$ **(g/min) 0.5µm**	$\dot{M}_{t}$ **(g/min) 0.5µm**	$\dot{M}_{mf}$ **(g/min) 2µm**	$\dot{M}_{t}$ **(g/min) 2µm**	$\dot{M}_{mf}$ **(g/min) 5µm**	$\dot{M}_{t}$ **(g/min) 5µm**
37	1.87E-03	0.82	0.03	3.28	0.19	8.20
38	1.90E-03	0.84	0.03	3.37	0.19	8.41
39	1.92E-03	0.86	0.03	3.45	0.19	8.62
40	1.94E-03	0.88	0.03	3.53	0.19	8.81
41	1.96E-03	0.90	0.03	3.60	0.20	9.00
42	1.97E-03	0.92	0.03	3.67	0.20	9.19
43	1.99E-03	0.94	0.03	3.74	0.20	9.36
44	2.00E-03	0.95	0.03	3.81	0.20	9.53
45	2.02E-03	0.97	0.03	3.88	0.20	9.69
46	2.03E-03	0.99	0.03	3.94	0.20	9.85
47	2.04E-03	1.00	0.03	4.00	0.20	10.00

Table F.2. Flow Required to Fluidize TiO_2 1μm and 2μm Particles.

T (°C)	$\dot{M}_{mf}$ **(g/min) 0.5μm**	$\dot{M}_{t}$ **(g/min) 0.5μm**	$\dot{M}_{mf}$ **(g/min) 1μm**	$\dot{M}_{t}$ **(g/min) 1μm**	$\dot{M}_{mf}$ **(g/min) 2μm**	$\dot{M}_{t}$ **(g/min) 2μm**
37	2.52E-03	1.00	0.01	2.00	0.04	3.99
38	2.54E-03	1.02	0.01	2.05	0.04	4.09
39	2.56E-03	1.05	0.01	2.09	0.04	4.18
40	2.58E-03	1.07	0.01	2.13	0.04	4.27
41	2.60E-03	1.09	0.01	2.18	0.04	4.35
42	2.62E-03	1.11	0.01	2.22	0.04	4.44
43	2.63E-03	1.13	0.01	2.26	0.04	4.51
44	2.65E-03	1.15	0.01	2.30	0.04	4.59
45	2.66E-03	1.17	0.01	2.33	0.04	4.66
46	2.67E-03	1.18	0.01	2.37	0.04	4.74
47	2.69E-03	1.20	0.01	2.40	0.04	4.81

As can be seen from the tables, operating at constant pressure even a ΔT of 10°C did not cause major adjustments on the CO_2 flow rate required to fluidize the particles, compared to the effect of particle size. As the samples presented a variable particle size which facilitates the fluidization, the best results were obtained for 2-5 g CO_2/min.

Appendix G. UV Calibration

The first set of UV analysis consisted of running the UV with an empty disposable cuvette and two different solutions (Chitosan-DMSO-water solution in a quartz cuvette and water-Chitosan in a quartz cuvette (Figure G.1)). The idea of these measurements was to determine first if a disposable (PMMA) or quartz cuvette should be used for Chitosan determination, and the answer for this was any of them, since the Chitosan peak shows at 294 nm where there is no interference of the cuvette materials at this wavelength. Then as the disposable cuvettes were more accessible and were proven not to interfere with the samples, these were chosen.

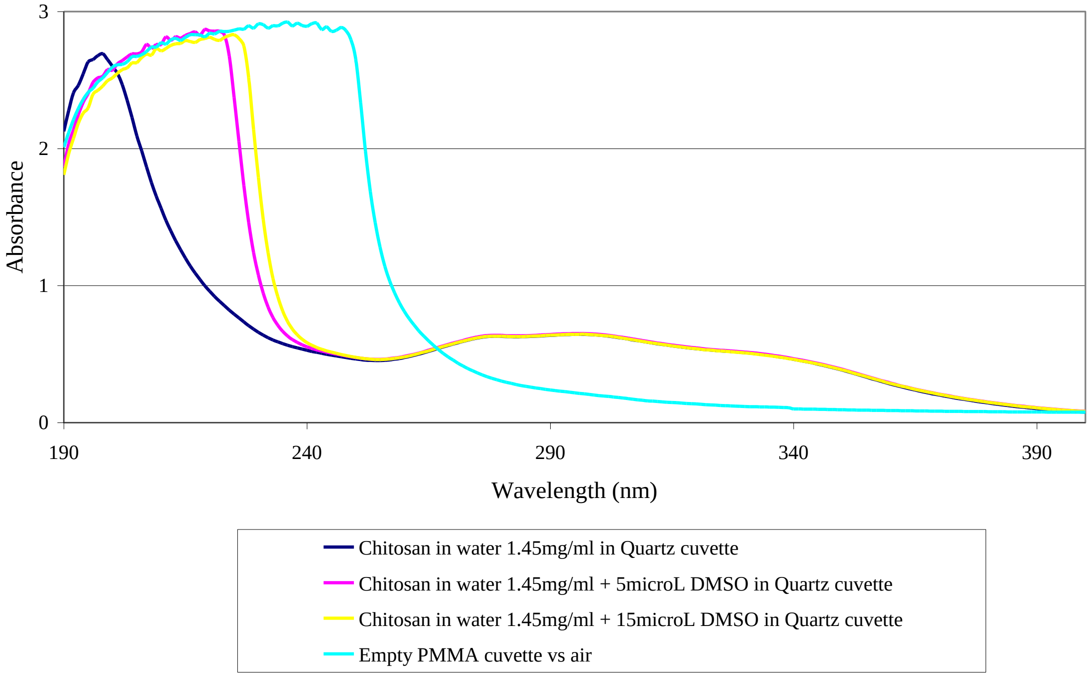

Figure G.1. Cuvette Evaluation for Water-DMSO-Chitosan System.

The next set of experiments consisted in running two solutions of Chitosan-DMSO-water and changing the DMSO concentration in order to observe any interference on the Chitosan determination. Chitosan has two peaks, one at 195 nm and another at 294 nm. The first one cannot be used because it saturates the instrument and overlaps with the DMSO peak. Due to these results, Chitosan concentration will be obtained from the peak at 294 nm, since DMSO and Chitosan peaks in the region 195-245 nm cannot be de-convoluted, and UV cannot be used to determine DMSO concentration.

Finally, a set of Chitosan-water solutions were prepared in order to construct a calibration curve using disposable cuvettes, as was proven that neither the DMSO nor the cuvette material represent an interference for this analysis.

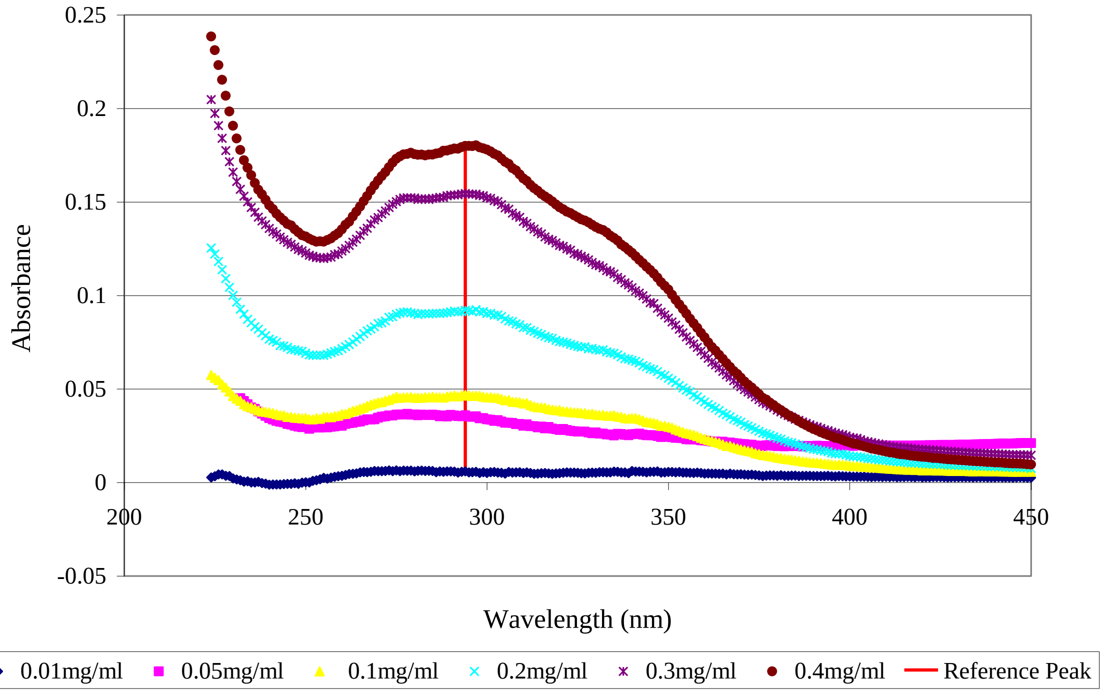

Figure G.2. UV Spectra for Chitosan-Water Solutions. Reference peak 294 nm.

Figure G.2 shows the UV plots and an absorption band at 294 nm for all Chitosan-Water solutions prepared to build a calibration curve based on Chitosan absorption. This curve is required in order to determine the Chitosan concentration on the solution collected at the end of the dynamic solubility set-up.

The UV spectrum for Chitosan reported in the bibliography (Muzzarelli 1973, Siokonkowska 2004, Guanghan 2006) mention absorption bands of 250nm, 278nm, 280nm, 295nm depending on the molecular weight and the UV exposure of the sample, given that the chromophores responsible for the UV absorption are related to the carbonyl and amino groups in the Chitosan (Andrady 1996).

With the readings obtained at the absorption band of 294 nm for six different solutions of Chitosan-Water, a calibration curve was built; this data is presented as a linear relation in Figure G.3.

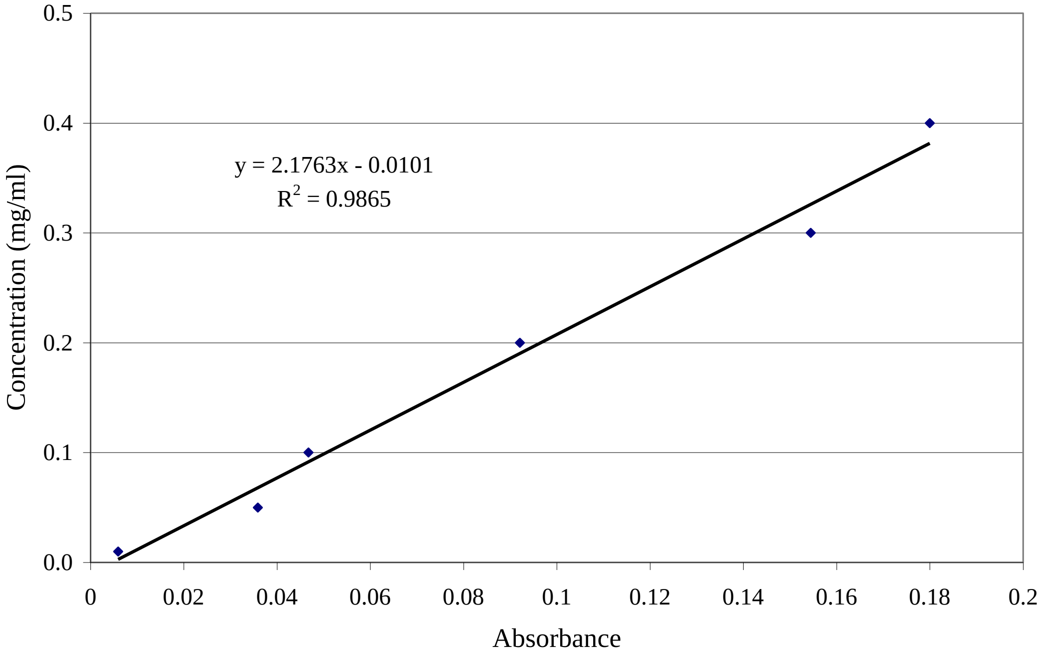

Figure G.3. Calibration Curve for Chitosan-Water Solutions Wavelength 294nm.

Appendix H. Quantification of Carbon Dioxide During Solubility Experiments

The amount of carbon dioxide used during the solubility experiments was determined in two different ways: by using the Improved Rackett Equation (IRE) and by direct measurement with a Wet Test Meter (WTM).

When running solubility experiments, the carbon dioxide was fed into the system with a syringe pump. The body or tank of the pump was kept at a constant temperature of -3°C (270.15°K) and the controller of the pump had a screen reporting temperature, pressure and volume readings in the syringe tank at all the times, providing a way to measure the amount of carbon dioxide in the feed.

The Improved Rackett Equation (IRE) can be written as:

$$\frac{1}{\rho} = \left(\frac{R\,T_c}{P_c}\right) Z_c^{\left[1+\left(1-T_r\right)^{2/7}\right]} \qquad (1)$$

This is a simple equation. No arbitrary constants are required and the only information needed is the critical properties of the substance to be evaluated. In addition, this equation has been reported to be able to predict reasonable results between the triple point and the critical point for most substances (Spencer, 1972).

By using the subsequent data and IRE the moles of CO_2 fed to the system were calculated as follows.

Table H.1. Data for IRE Calculations.

Experimental Data	**Constants and CO_2 Critical Properties**
T_{pump} = -3°C= 270.15°K	R= 83.1447 $\text{bar cm}^3 / \text{mol}\ ^\circ\text{K}$
V_{CO2} (l) = 360.28cm^3 (vol. of liquid carb dioxide in the syringe pump at -3C)	Pc= 73.7 bar
	Tc= 304.18K
	Zc= 0.2736

$$\frac{1}{\rho} = \left(\frac{83.1447 \cdot 304.18}{73.7}\right) \cdot 0.2736^{\left[1+\left(1-\frac{270.15}{304.18}\right)^{2/7}\right]} = \frac{1}{46.91\,\text{cm}^3/\text{mol}}$$

$$\rho = \frac{N}{V} \Rightarrow N = \frac{360.28\text{cm}^3}{46.91\,\text{cm}^3/\text{mol}} = 7.68\text{mol of } CO_2 \qquad (2)$$

The experimental data obtained from the dynamic set-up calculated using the IRE is presented in table H2.

Table H.2. CO_2 Feed from IRE Calculations.

T_{pump} (°C)	**T_{pump} (°K)**	**$V_{CO2,l}$ (cm^3)**	**1/ρ (cm^3/mol)**	**N_{CO2}**
-3.00	270.15	360.28	46.91	7.68
-3.00	270.15	315.00	46.91	6.72
-3.00	270.15	288.18	46.91	6.14
-3.00	270.15	299.15	46.91	6.38
-3.00	270.15	295.00	46.91	6.29
-3.00	270.15	278.00	46.91	5.93
-3.00	270.15	235.00	46.91	5.01
-3.00	270.15	365.00	46.91	7.78

After passing through the solubility set-up, the carbon dioxide was released in its gas phase and the volume of the gas released was measured with a Wet Test Meter located at the end of the experimental system. While the experiment was run, the total operation time as well as the room temperature was registered, so by considering it as an ideal gas, the moles of CO_2 released could be easily calculated.

$$P\cdot V = N\cdot R\cdot T \Rightarrow \quad N = \frac{P\cdot V}{R\cdot T}$$

$$N = \frac{1\,\text{bar}\cdot 190323.6\,\text{cm}^3}{83.1447\,{}^{\text{bar}\cdot\text{cm}^3}\!\big/_{\text{mol}\cdot{}^\circ\text{K}}\cdot 297.55^\circ\,\text{K}} = 7.70\,\text{mol} \tag{3}$$

The experimental data obtained from the dynamic set-up calculated using the WTM is presented in table H3.

Table H.3. CO_2 Feed from WTM Measurements.

T_{WTM} (°C)	**T_{WTM} (°K)**	**V_{WTM} (cm^3)**	**N_{CO2}**
24.40	297.55	190323.60	7.70
25.40	298. 55	172111.80	6.94
25.00	298.15	153456.00	6.19
24.20	297.35	154769.60	6.26
24.00	297.15	158895.30	6.43
24.50	297.65	146790.00	5.93
26.20	299.35	125334.50	5.04
25.20	298.35	192015.40	7.74

Appendix I. Quantification of Chitosan and DMSO During Encapsulation Experiments

The polymer used in this research, Chitosan Oligosaccharide Lactate, is soluble in DMSO at room temperature for concentrations not higher than 17% w/w, as presented in Chapter 6. Accordingly, it was more practical to prepare the liquid solutions of DMSO-Chitosan previous to starting the encapsulation experiments, and the feed composition for these components was determined from the feed rate set on the HPLC pump, the concentration of the solution and the operation time. The other component for the encapsulation mixture was the carbon dioxide, and the feed information was obtained from the continuous pump.

Table I.1. Feed Composition for Encapsulation Experiments

System	**Encapsulation Operation Conditions**			**Feed Composition**			
Component	**P (bar)**	**T (ºC)**	**t (min**	**Core**	**Chitosan**	**DMSO (g)**	**CO2 (g)**
CaO	111.0	48.9	30	0.10	0.10	5.50	60
CaO	119.0	41.9	50	0.30	0.14	15.85	96
CaO	119.8	44.8	45	0.20	0.14	14.86	90
TiO2	110.0	45.0	73	0.20	0.21	12.00	146
TiO2	120.0	44.0	60	0.20	0.09	22.00	80

In order to be able to explain the encapsulation mechanism evaluating the effect of the feed composition and the operation conditions, the predicted amount of Chitosan and DMSO that could precipitate in the encapsulation cell was estimated by using the following expression:

Appendix I (Continued)

$$P_m = \left(S_f - S_{c(T,P)}\right) \times \frac{F}{t} \qquad (1)$$

where:

P_m: precipitated material (g)

S_f: Solubility in the feed

S_c: Solubility in the bed (from solubility experimental data)

F: Feed rate (g/min)

t: contact time (min)

Based on the solubility data obtained experimentally for the system Chitosan-DMSO-SCCO$_2$, the feed composition and the operation conditions evaluated in the encapsulation the estimated amount of material precipitated inside the cell is presented in the following tables.

Table I.2. Chitosan Mass Balance from Solubility Data

Encapsulation Operation Conditions			**Composition**			
P (bar)	**T (ºC)**	**t (min)**	**Chitosan (g)**	**Feed S_f**	**Cell S_c**	**Precipitate P_m (g)**
111.0	48.9	30	0.10	1.5243E-3	9.7800E-6	1.5146E-4
119.0	41.9	50	0.14	1.2858E-3	2.3100E-5	1.8183E-4
119.8	44.8	45	0.14	1.2858E-3	1.2900E-5	1.7185E-4
110.0	45.0	73	0.21	2.2480E-3	1.0000E-5	4.6999E-4
120.0	44.0	60	0.10	5.2848E-4	1.2917E-5	4.6401E-5

Appendix I (Continued)

Table I.3. DMSO Mass Balance from Solubility Data at the Cell

Encapsulation Operation Conditions			**Composition**			
P (bar)	**T (ºC)**	**t (min)**	**DMSO (g)**	**Feed S_f**	**Cell S_c**	**Precipitate P_m (g)**
111.0	48.9	30	5.50	1.0701E-1	8.3869E-2	1.2726E-1
119.0	41.9	50	15.85	1.4149E-1	1.0700E-1	5.4657E-1
119.8	44.8	45	14.86	1.4200E-1	1.4149E-1	7.5326E-3
110.0	45.0	73	12.00	1.4136E-1	1.1000E-1	3.7628E-1
120.0	44.0	60	22.00	1.4215E-1	1.4157E-1	1.2926E-1

Table I.4. Mass Balance from Solubility Data DMSO Removal

Encapsulation Operation Conditions			**Composition**			
P (bar)	**T (ºC)**	**t (min)**	**CO_2 (g/min)**	**Feed S_f**	**Cell S_c**	**Removed P_m (g)**
111.0	48.9	120	20	1.1000E-1	1.0700E-1	7.20
119.0	41.9	40	40	1.6210E-1	1.0700E-1	8.82
119.8	44.8	240	25	1.6000E-1	1.4200E-1	10.80
110.0	45.0	180	15	1.4000E-1	1.1000E-1	8.10
120.0	44.0	180	20	1.6000E-1	1.4157E-1	6.64

The results obtained from the mass balances presented in these tables indicates that the solubility decreased inside the encapsulation cell, which is completely reasonable, and the temperature was raised at a constant pressure (Encapsulation Operation Conditions) to promote the polymer precipitation. The results from Table I.4 indicate that the volume of $SCCO_2$ used to remove DMSO was higher than required, which could cause Chitosan removal, reducing encapsulant thickness. For example, the

$SCCO_2$ injected in the cell at 111 bar and 48.9ºC was enough to remove 7.2g of this chemical under these operation conditions, and the amount of DMSO inside the cell before its removal was 0.11g.